Progress Towards High Precision Measurements on Ultracold Metastable Hydrogen and Trapping Deuterium

by

Julia K. Steinberger

Submitted to the Department of Physics
in partial fulfillment of the requirements for the degree of

Doctor of Philosophy

at the

MASSACHUSETTS INSTITUTE OF TECHNOLOGY

[September 2004]
August 2004

Author ....
Department of Physics
August 26, 2004

Certified by ....
Thomas J. Greytak
Professor of Physics
Thesis Supervisor

Certified by ....
Daniel Kleppner
Lester Wolfe Professor of Physics
Thesis Supervisor

Accepted by ....
Thomas J. Greytak
Chairman, Associate Department Head for Education

Progress Towards High Precision Measurements on Ultracold Metastable Hydrogen and Trapping Deuterium

by

Julia K. Steinberger

Submitted to the Department of Physics
on August 26, 2004, in partial fulfillment of the
requirements for the degree of
Doctor of Philosophy

Abstract

Ultracold metastable trapped hydrogen can be used for precision measurements for comparison with QED calculations. In particular, Karshenboim and Ivanov [Eur. Phys. Jour. D **19**, 13 (2002)] have proposed comparing the ground and first excited state hyperfine splittings of hydrogen as a high precision test of QED. An experiment to measure the $2S$ hyperfine splitting using a field-independent transition frequency in the $2S$ manifold of hydrogen is described. The relation between the transition frequency and the hyperfine splitting requires incorporating relativistic and bound state QED corrections to the electron and proton g-factors in the Breit-Rabi formula. Experimental methods for measuring the magnetic field of an ultracold hydrogen sample are developed for trap fields from 0 to 900 G. The temperature of the trapped sample at the field-independent point is a critical parameter, and is inferred from the $1S - 2S$ lineshape. The detailed dependence of this lineshape on the trap geometry is examined. A search for the transition was undertaken, but no signal was observed. The systematics of the experiment are analyzed, and modifications for carrying out the experiment are proposed.

In a separate study, the possibilities for trapping (never previously trapped) deuterium in the same cryogenic cell and magnetic trap used to trap hydrogen were investigated. Deuterium's behavior on a helium surface differs markedly from that of hydrogen due to its larger surface binding energy. We carried out a variety of studies of both hydrogen and deuterium during the trap-loading stage, working with both ^{4}He and ^{3}He surfaces. Introducing ^{3}He in the cell decreases the surface binding energy of deuterium, and thus the rate of recombination on the cell walls; however, we could not achieve deuterium trapping through helium-surface cooling. It is proposed that buffer gas loading can be used to cryogenically cool and trap deuterium.

Thesis Supervisor: Thomas J. Greytak
Title: Professor of Physics

Thesis Supervisor: Daniel Kleppner
Title: Lester Wolfe Professor of Physics

Acknowledgments

The first people to thank are obviously the Utracold Hydrogen group. Tom Greytak and Dan Kleppner are very good people to work with, providing a long term vision and focus necessary in such an intense experimental environment. My colleagues here, Dale Fried, Tom Killian, and Adam Polcyn who were on their way out when I started, Stephen Moss and David Landhuis who showed me the ropes, Kendra Vant and Lia Matos who started with me, Bonna Newman and Cort Johnson who are welcome recent additions to the group, and of course Lorenz Willmann, without whom nothing would ever get done, have been wonderful people to work with and I have learned enormously from them. The friendships we have formed will last beyond our days at MIT. I also want to mention several wonderful undergraduate students whose work and company were most welcome: Philip Larochelle, Sourav Mandal, and Mukund Vengalatorre. Our recent arrivals from Harvard, Rob deCarvalho and Nathan Brahms, have also been fun and helpful around the lab.

I don't think anyone can survive seven years as an MIT physics graduate student without lots of help from family, friends, and colleagues. My parents Jack and Cynthia Steinberger have always supported me with their steadfast belief I could do anything. They helped me be inquisitive and confrontational, essential skills in physics.

My brothers John, Joseph and Ned have provided both encouragement and inspiration along the way. John lived with me for part of graduate school, and found a second home at MIT. Joe and Ned were always ready to open their doors to me and my friends in Maine, and always found ways to distract me from my work troubles. I hope to follow their example of pursuing their own projects despite the odds.

Ned's wife, Denise, has been a big help to my whole family, and all us of owe part of our lives and sanity to her medical knowledge and listening skills. Abe and Lucas, Ned and Denise's sons, have been the lights of my life during these past years. Abe was born during my first year of graduate school, and it has been a great joy to be close enough to see him grow up. Joe's wife Keiko is a welcome addition to the family.

I have been fortunate in finding many good friends in graduate school. Molly Hicks, Kristin Burgess, Mario Serna and Ananth Chikkatur were the best quantum mechanics homework buddies anyone could hope to have. Derek Fox, Jeff Kommers, Patrick Wojdowski were wonderful officemates for my first two years in astrophysics. My first advisor at MIT, Vicki Kaspi, was unmatchable in energy and enthusiasm. Deepto Chakrabarty, Bryan Gaensler, and Walter Lewin were wonderful collaborators. Chandra Raman, whom I met through the wonderful spectroscopy seminars, encouraged me to switch from astrophysics to atomic physics. Though it all didn't work out as expected, his confidence and optimism were always helpful.

The Women in Physics group provided nourishment and companionship throughout my time at MIT.

Brice Smith, Michelle Povinelli, Mehdi Yahyanejad, Yoav Bergner and Mike Ohliger helped me survive solid state physics. Brice became a companion in many adventures in alternative politics, which Michelle documented in photography. I hope to follow Brice's example of anti-nuclear activism and use my physics knowledge to make the world a less dangerous place. Mehdi and I spent many an hour pressuring MIT to

take a stand for Iranian student visas outlawed in the Patriot Act. We were unsuccessful, but I learned much from Mehdi and his calm, smiling style of activism. Yoav is pursuing his dreams of being the most over-qualified carpenter in the world (how often is string theory really relevant?), and I admire his dedication to becoming an artist.

While we're on the topic of friends and politics, many people have helped me make sense of living in America in these times. Nick Giannone inspired me through his bravery and principles. Mike Borucke, Felix AuYeung, Brice and Saurabh Asthana were political companions in the MIT Social Justice Cooperative and the murky world of MIT's underground journalism. Saurabh's friend Thomas Barker helped through his patience, sense of humor, and beautiful paintings. Man around town Terry O'Brien generally brings the party and the excitement with him. I met my housemate Dan Keshet and friends Gil Obler and Devon McCullough during the Nader 2000 campaign. Mark Weaver, Linda Pinkow and and Chuck Rosina of WMBR encouraged me to go into radio journalism, which I fell in love with. Stephanie Wei Wang, Payal Parekh and Sanjay Basu were inspirational in their dedication to effective political action. Scott Cooper and George Collins can't be beat, either as a comedic team or for cogent analysis. More recently, Aram Harrow, Suzanne Nguyen and Adam Holt were the source of many fruitful (and sometimes heated) discussions. Samuel Arey shared many of my environmental and political interests. His sense of fun and kindness that taught me that life should be lived on one's own terms, not those of graduate school. Although we both failed miserably in this during the past year, I trust we will be more successful in the future. All these people managed to be friends and comrades despite personal differences and external pressures, and they have made my time at MIT immeasurably richer than it would have been in their absence.

Saurabh Asthana and Dan Keshet made the past four years on Cherry St. one of the best times of my life. Their friendship, inquisitiveness, squabbling over details, enthusiasm and eclectic music tastes ensured that home was never a boring place. Saurabh and Brice brought Isak-the-cat to Cherry St., and she brought us companionship, entertainment, and much needed neighborhood rodent extermination.

MIT provides an environment where many individuals and groups can flourish. It is an open campus, with excellent facilities available to student groups. Although I have had my share of differences with the MIT administration, I hope that it remains an open campus welcoming of student activity and initiative.

MIT's staff helps make it a very special place. The Center for Ultracold Atoms lost our dear administrator Carol Costa earlier this year. Her warm presence and encouragement helped everyone who came to see her, and she is missed.

The staff of the Physics Education Office are always kind and helpful, even under pressure, and they take their role of student advocates very seriously.

The staff from the Central Machine Shop, especially head machinist Peter Morley, were always helpful and often finished emergency jobs within 24 hours. They also provided crucial guidance and encouragement in repairing the leaking cryostat, making special trips to the lab to understand what I was talking about, and were always tolerant of my often incomplete drawings.

Libby Shaw of the Center for Material Science and Engineering shared facility did the surface spectroscopy that allowed us to understand our BBO crystal damage. She offered help and advice, and even did surface spectroscopy of bits and pieces of plastic tubing for us.

Dan Giblin in Building 13 has taught me about the soviet history of World War II, as well as how to navigate some paperwork mazes at MIT.

Markos Hankin of the Physics Department lecture demonstration group always helped me pick out good demonstrations for my Saturday morning physics sessions with neighborhood kids.

Some facilities MIT does not have, however, and then we have to go to Harvard. Jim MacArthur of the Harvard Physics Department electronics shop is an invaluable resource, and had helped us many times.

I took many physics classes, but some professors stand above the others. It is a privilege to be in a classroom with Mehran Kardar and John Joannopoulos. They are excellent physicists who care about communicating some of their understanding to students.

To my family

Time comes into it.
Say it. Say it.
The universe is made of stories,
not of atoms.

Muriel Rukeyser

Contents

1 Introduction 14

2 Experimental Methods for Ultracold Hydrogen 16
- 2.1 Introduction 16
- 2.2 Overview of the Apparatus 16
- 2.3 Generating and Cryogenically Cooling Atomic Hydrogen 18
  - 2.3.1 The cryogenic discharge 18
  - 2.3.2 The superfluid-helium-coated cell 19
  - 2.3.3 Cooling and losses on the cell walls 21
- 2.4 Trapping Spin-Polarized Hydrogen 23
  - 2.4.1 Hydrogen in a magnetic field 23
  - 2.4.2 Loading the magnetic trap 24
- 2.5 Cooling Magnetically Trapped Hydrogen 27
  - 2.5.1 Magnetic saddlepoint evaporation 27
  - 2.5.2 Hyperfine resonance rf evaporation 27
- 2.6 Use and Characterization of the Bolometer 28
  - 2.6.1 Operation of the bolometer 28
  - 2.6.2 Bolometric density measurement 29
  - 2.6.3 Recombination sensitivity to cell temperature 30
  - 2.6.4 Recombination sites in the cell 31
  - 2.6.5 Measuring the helium film thickness 31
  - 2.6.6 Detecting ^{3}He in the cell 32
- 2.7 $1S - 2S$ Detection of Hydrogen 34
  - 2.7.1 The 243 nm laser system 34
  - 2.7.2 Exciting the sample 34
  - 2.7.3 The $1S - 2S$ spectrum 35
  - 2.7.4 $1S - 2S$ Excitation rate and sample decay 35

3 2S Hyperfine Spectroscopy of Hydrogen 36
- 3.1 Introduction and Motivation 36
  - 3.1.1 Comparing the 1S and 2S hyperfine splittings to test QED . . 36
  - 3.1.2 Summary of the experimental procedure 39
- 3.2 Theory of the 2S Hyperfine Spectrum 43
  - 3.2.1 The Breit-Rabi formula 43
  - 3.2.2 Eigenstates 44

3.2.3 Field-independent points 45
3.2.4 Corrections to the Landé electron and proton g factors 46
3.2.5 Calculating the Field-Independent Point Transition Frequency 49
3.3 Magnetic Field Measurement 51
3.3.1 Trap bottom magnetic field: 1S hyperfine resonance 51
3.3.2 Average magnetic field: $2S_{1/2} \rightarrow 3P_{3/2}$ transition 54
3.3.3 Magnetic field dependence of 1S-2S transition 60
3.4 Temperature Measurement 60
3.4.1 The doppler-free double-exponential lineshape 61
3.4.2 Systematics of the double-exponential linewidth 62
3.4.3 High-magnetic-field temperature measurement 63
3.4.4 Adiabatically changing a harmonic trap 64
3.4.5 Harmonic frequencies in a Ioffe-Pritchard trap 65
3.4.6 Methods to lower the trap temperature at high magnetic fields 67
3.5 Calculating the 2S $|d\rangle$ to $|c\rangle$ Transition Strength 68
3.5.1 Introduction 68
3.5.2 Linewidths 68
3.5.3 Matrix element 69
3.5.4 The transverse rf coil at 82 MHz 69
3.5.5 Estimate of the 2S $|d\rangle \rightarrow |c\rangle$ decay rate from the 1S results . . 71
3.5.6 Complete model of the time dependence of the 2S $|d\rangle \rightarrow |c\rangle$ signal 72
3.5.7 Estimating the 2S $|c\rangle$ state signal strength 74
3.6 Expected Sources of Broadening and Shifts 74
3.6.1 Accuracy of rf source 74
3.6.2 Magnetic and thermal broadening 74
3.6.3 Magnetic field fluctuations 75
3.6.4 Lineshape modelling 75
3.7 Future Possibilities for 2S $|d\rangle$ to $|c\rangle$ Precision Measurements 77

4 The Quest to Trap Deuterium **79**
4.1 Introducing Deuterium 79
4.1.1 Overview of past deuterium experiments 79
4.1.2 Comparison of deuterium and hydrogen 81
4.1.3 Deuterium and hydrogen recombination on helium surfaces . . 83
4.1.4 Difficulties in trapping deuterium and experimental goals . . . 86
4.2 $1S - 2S$ Detection of Warm Hydrogen 87
4.2.1 Description of the $1S - 2S$ detection of warm hydrogen 87
4.2.2 Comparison of warm and cold sample data, I_{warm} and N_{cold} . . 88
4.2.3 Discharge power 88
4.2.4 Discharge duration 90
4.2.5 Initial cell temperature 90
4.2.6 Radial (quadrupole) magnetic field 91
4.2.7 What can be learned from warm sample $1S - 2S$ detection? . 93
4.3 Time-Resolved Studies of Discharge Pulses 93
4.3.1 Interest in time-resolved study of individual discharge pulses . 93

4.3.2 Method and geometry of bolometer discharge pulse detection . 94
4.3.3 Discharge pulse profiles dependence on magnetic fields 95
4.4 Hydrogen Discharge Pulse Profile Time-Resolved Studies 96
4.4.1 Loading magnet low: detecting (mostly) low-field-seekers . . . 96
4.4.2 Loading magnet high: detecting (mostly) high-field-seekers . . 98
4.4.3 Possible sources of the slow discharge pulse arrival time signal 100
4.4.4 Time-of-flight analysis of discharge pulse profiles 101
4.4.5 Interpretations of the time-resolved discharge pulse profile data 103
4.4.6 Effect of introducing ^{3}He in the cell 104
4.5 Deuterium Discharge Pulse Profile Time-Resolved Studies 105
4.5.1 Starting the deuterium discharge 105
4.5.2 Magnetic field and cell temperature dependence of discharge pulse signals 105
4.5.3 Time-of-flight analysis of deuterium discharge pulses 107
4.5.4 Effect of introducing ^{3}He in the cell 107
4.6 Buffer Gas Trap Loading 111
4.7 Conclusions of Deuterium Study 112

A BBO Doubling Crystal Surface Contamination 113
A.1 The BBO Doubling Crystal and its Maintenance 113
A.2 Crystal Surface Damage and Color Centers 113
A.3 A New Type of Crystal Surface Damage 114
A.4 Crystal Contamination Diagnosis 114
A.5 Finding the Contamination Source 115
A.6 Building Air Flow and Lab Overpressure 115
A.7 Damage Mechanism: Fluorine vs. Chlorine 116
A.8 Crystal Surface Repair Techniques 116

B Superfluid Helium Jacket Fill Line Design 117
B.1 Filling and Emptying the Jacket 117
B.2 Contributions to the Heat Load on the Mixing Chamber 118
B.2.1 Liquid-helium filled jacket line (no flow) 118
B.2.2 Blackbody heating from 4K IVC tailpiece 118
B.2.3 Thermal contact from kevlar threads to tailpiece 119
B.3 Superfluid Flow Heating 119
B.4 Current Fill Line Design Summary 119

C Magnet Power Supply Control 121
C.1 Original Design, Floating Voltage Requirement 121
C.2 Control Voltage Circuit Design 121

D Repairing Leaking Dilution Fridge Heat Exchangers 125
D.1 What Are Dilution Fridge Heat Exchangers? 125
D.2 Discovery of a 4K Fridge to IVC Leak 125
D.3 Locating a Leak on the Cryostat 125

D.4 Possible Leak Repair Mishaps 126
D.5 Solder Tip Designing and Testing 127

List of Figures

2-1 Cell diagram 17
2-2 Helium film tears due to discharge pulses seen as dropouts on the bolometer 21
2-3 Surface residence and recombination times of hydrogen on ^{4}He 23
2-4 Hydrogen $1S$ hyperfine manifold 24
2-5 Magnet drawing and trap profile 25
2-6 Bolometer sensitivity as a function of the cell temperature (pure ^{4}He film) 30
2-7 Bolometer signal from lower pinch and quadrupole magnet dumps . . 32
2-8 Change in the bolometer bias voltage vs set resistance curve in the presence of ^{3}He in the cell 33

3-1 Hyperfine Zeeman structure of the hydrogen 2S state 38
3-2 Schematic of high and low field traps 40
3-3 Axial magnetic field profiles of low and high field traps. 42
3-4 The 2S field-independent point between $|d\rangle$ and $|c\rangle$. 46
3-5 The 2S $|d\rangle$ to $|c\rangle$ transition around field-independent point 47
3-6 $F = 1$ low-field hyperfine structure of the hydrogen 1S state. 52
3-7 1S Hyperfine magnetic trap bottom measurement. 53
3-8 Zeeman structure of the hydrogen $3P_{3/2}$ state 55
3-9 $2S_{1/2} - 3P_{3/2}$ Absolute magnetic field measurement 58
3-10 $2S_{1/2} - 3P_{3/2}$ High magnetic field (relative) measurement 59
3-11 Double-exponential linewidth as a function of temperature and axial trap frequency 63
3-12 Double-exponential linewidth as a function of trap center and laser focus offset 64
3-13 Transverse rf coil resonance with the cell at 83 MHz and resulting atom loss 70

4-1 Hyperfine-Zeeman spectrum of the deuterium 1S state 81
4-2 Density of ^{3}He and ^{4}He above a saturated film 84
4-3 Surface residence and recombination times of hydrogen and deuterium on ^{4}He and ^{3}He 85
4-4 I_{warm} and N_{cold} as a function of the discharge power 89
4-5 I_{warm} and N_{cold} as a function of the discharge duration 90
4-6 I_{warm} and N_{cold} as a function of the initial cell temperature 91

4-7 I_{warm} as a function of radial magnetic field 92
4-8 Hydrogen discharge pulses with a low magnetic field at the cell bottom 97
4-9 Hydrogen discharge pulses with a high magnetic field at the cell bottom 99
4-10 Hydrogen discharge pulses and time-of flight profiles 102
4-11 Deuterium discharge pulses in a ^{4}He cell: magnetic field and temperature dependence 106
4-12 Deuterium discharge pulses and time-of-flight profiles 108
4-13 Comparison between deuterium and hydrogen discharge pulses as a function of magnetic field 110

C-1 Floating voltage circuit for current supply control. 122
C-2 Feedback circuit for current supply control. 123

List of Tables

2.1 Geometrical factor δ for different trap geometries 30

3.1 Measured and calculated values of the 2S hyperfine splitting frequency 37
3.2 Electron and proton Landé g factors in hydrogen, and related quantities 50
3.3 Comparison of different g factors in calculating $\frac{g_e}{g_p}\frac{m_p}{m_e}$ 50
3.4 1S $|d\rangle \rightarrow |c\rangle$ decay rates at 82 MHz 71

4.1 Physical properties of molecular hydrogen and deuterium 82
4.2 Physical and spectroscopic properties of atomic hydrogen and deuterium 82

Chapter 1

Introduction

The MIT Ultracold Hydrogen group has a long history of investigating hydrogen in a cryo-magnetic trap: exploring the interaction of hydrogen on helium surfaces [5, 23, 118], trapping and cooling hydrogen into the quantum degeneracy regime [31], to exploring the physics of the $1S - 2S$ transition [11, 55], and preparing trapped metastable hydrogen [64].

New directions for the Ultracold Hydrogen group include high precision $2S - nS$ spectroscopy of metastable hydrogen, and buffer gas trapping of hydrogen with other species (for instance lithium) and subsequent cooling into the quantum regime. This thesis describes two separate projects, one in the direction of metastable precision spectroscopy (measuring the 2S hyperfine splitting), the other in the direction of trapping new species (deuterium).

Precision spectroscopy on metastable hydrogen is attractive in our apparatus, because we can create large, long-lived samples of magnetically trapped ultracold 2S atoms using a high power narrow linewidth UV laser system. The number of 2S atoms can be as high as 10^7 at densities of 10^{10} cm^{-3}. The 2S lifetime in our cell is close to 100 ms, limited by small stray electric fields. The temperature of the 2S sample is the same as that of the 1S sample, and the 2S atoms are magnetically confined in the same trap. The trapped 2S sample is thus an ideal system for high precision spectroscopy, and complements the traditional beam spectroscopy methods [38, 62].

The 2S hyperfine splitting experiment described in Chapter 3 of this thesis was a first endeavor to perform high precision measurements on the 2S sample. The goal was to measure the 2S hyperfine splitting by measuring the transition frequency between the two highest energy Zeeman states at a field-independent point of the hyperfine-Zeeman manifold. The 2S hyperfine splitting has been proposed as a part of a high precision test of QED by Karshenboim and Ivanov [52].

The hyperfine splitting measurement required new detection techniques by which we could selectively detect only one or the other 2S hyperfine state. It also demanded better understanding of our trap's magnetic field and sample temperature and geometry with respect to the UV laser beam. These experimental advances will be useful in future high precision experiments on ultracold metastable hydrogen.

After searching for the field-independent point transition, but not observing it, we analyzed the experiment systematics further. In particular, we characterized the rf interaction with the cell and the atoms, measuring the decay rates at the appropriate frequency for the 1S state. We also discovered a drastically reduced 2S lifetime in our cell due to an electric contact failure. A full analysis of the possible count rate of the 2S field-independent point transition showed that the measurement was not feasible under the circumstances, but could be done with modifications in the future.

A number of past studies aimed towards magnetically confining and ultimately trapping deuterium have given disappointing results [21]. The new interest in trapping fermionic quantum gases encouraged us to try again. We investigated the possibilities for trapping deuterium using the same apparatus we normally use for hydrogen, as described in Chapter 4. We developed new detection techniques to study pre-trapped atoms in our cell, and the impact of the magnetic fields and cell temperature on their behavior.

Deuterium recombines much more readily than hydrogen on helium surfaces. We can see this effect in all of our deuterium studies with both ^{3}He and ^{4}He surfaces in the cell. We also detect a decrease in the loss to the cell walls with ^{3}He compared to ^{4}He. However, we could not achieve deuterium trapping through helium-surface cooling.

The Ultracold Hydrogen group is developing a new buffer gas trap loading experiment for hydrogen. This gives promise for providing the technique that will at last allow us to successfully trap deuterium.

Chapter 2 of this thesis describes the experiment as a whole, with emphasis on parts that are necessary in the subsequent chapters. The appendices include solutions to puzzling technical problems that arose in the MIT Ultracold Hydrogen group.

Chapter 2

Experimental Methods for Ultracold Hydrogen

2.1 Introduction

Ultracold atoms now constitute a large subfield of atomic physics. Atomic hydrogen occupies a special place in that subfield because the experimental techniques are fundamentally different from the laser cooling methods that are commonly used (see Metcalf and van der Straten [72] for a review of these).

To provide a framework for the problems that are addressed in this thesis, and to summarize technical details that may be of use to others, I start by providing a summary of the essential experimental method. Many of the experimental components and methods described here have been developed over the years by members of the hydrogen group, and I will frequently refer to their theses for further detail.

This chapter describes in some detail the major components of the apparatus, as well as the methods used to study the trapped atoms. Although hydrogen is the main trapped species, deuterium can be substituted throughout with a few key differences that will be expounded in Chapter 4.

2.2 Overview of the Apparatus

A schematic design of the major components of the apparatus is shown Fig. 2-1. This figure is not to scale. The different subsystems are outlined briefly below.

Cryogenic cell and discharge

The first subsystem of the experiment is the cryogenic cell that encloses the trapped atoms. It is coated with superfluid helium and connected to a cryogenic hydrogen discharge. The cell-discharge assembly is thermally anchored to, and continuously cooled by, an Oxford 2000 [83] dilution refrigerator (see Chapter 7 of Pobell [85]).

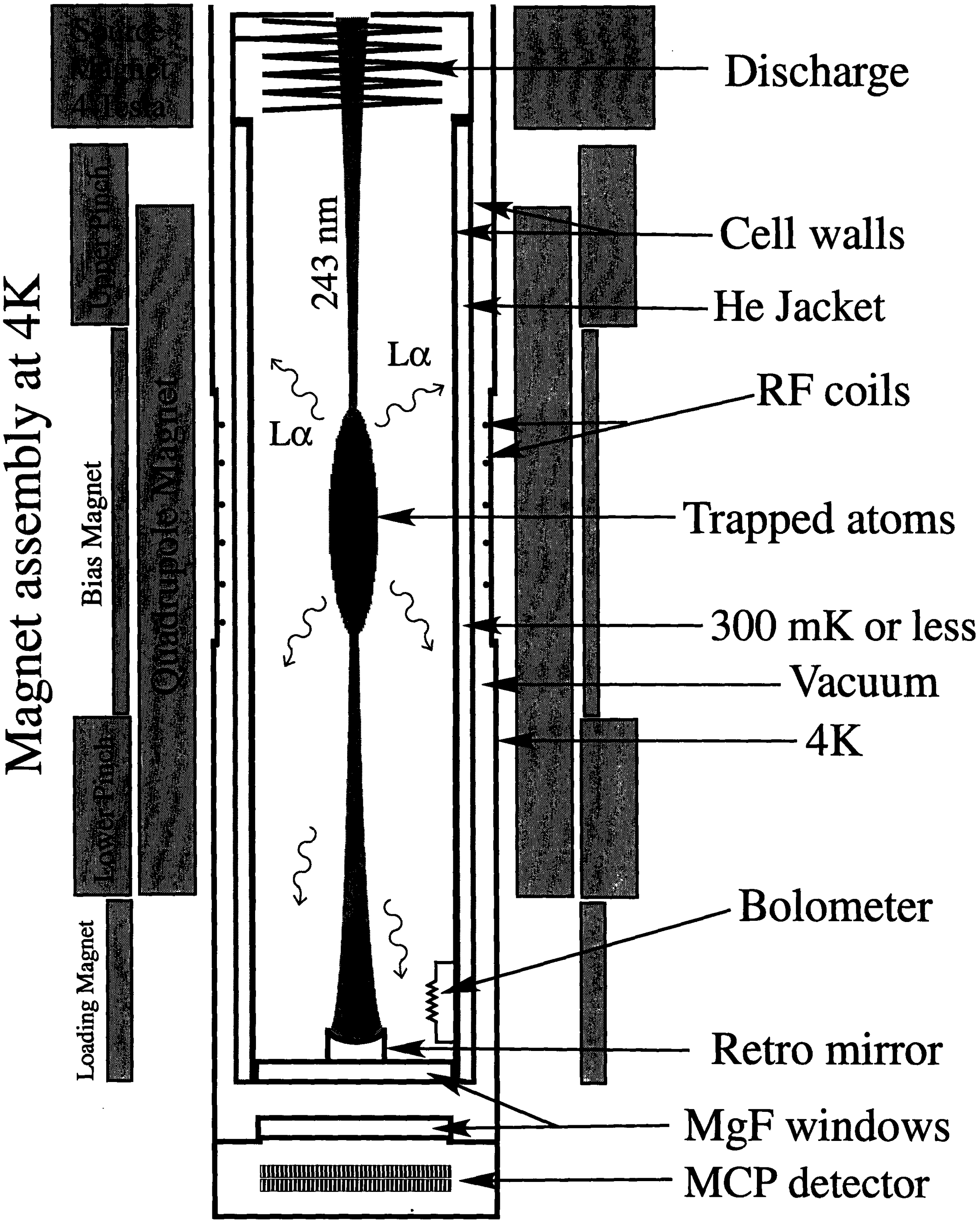

Figure 2-1: Schematic of the cell, showing the discharge, cell, main magnets, and detection chamber. This figure is not to scale.

Trapping Magnets

The magnetic trap is in the Ioffe-Pritchard configuration [86, 66]. The trapping fields are created by 11 superconducting magnets, that surround the cell and are cooled to 4 K by a liquid helium bath.

Bolometer

Our major diagnostic tool for hydrogen trapping is a bolometer (heat-sensitive resistance). The bolometer detects any kind of energy deposited on its surface, but mainly the hydrogen atom-to-molecule recombination energy. The trapped hydrogen sample must be destroyed (dumped out of the magnetic trap) to be detected on the bolometer.

$1S-2S$ Detection

A more sophisticated and powerful detection method is two-photon $1S-2S$ spectroscopy of the trapped hydrogen [11]. This is done using 10-20 milliwatts of UV laser light at 243 nm (half the frequency of the $1S-2S$ transition). The beam is sent down into the cell and retroreflected by a mirror at the bottom. This excites a small fraction of the trapped, cold $1S$ hydrogen atoms to the $2S$ metastable state. The $2S$ atoms are magnetically trapped.

These $2S$ atoms are then quenched using electric field plates on either side of the cell. The resulting emitted Lyman-α photons are detected by the Micro Channel Plate (MCP) detector. The MCP is located below the cell, in a vacuum detection chamber connected to the 4 K helium bath.

This detection method is used on trapped atoms, and is non-destructive.

$2S-3P$ Spectroscopy

Another detection tool that has been developed recently by Kendra Vant in our group [108] is one-photon $2S-3P$ 656 nm spectroscopy of the magnetically trapped $2S$ atoms. This transition can be detected as a depletion in the normal $2S$ signal level, or as an absorption of the red (656 nm) laser beam. This detection technique is useful as a potential alternate measurement technique for the $2S$ signal, for measuring the magnetic field in the trap, and as a temperature measurement technique (through Zeeman broadening). $2S-3P$ spectroscopy is described more fully in Chapter 3.

2.3 Generating and Cryogenically Cooling Atomic Hydrogen

2.3.1 The cryogenic discharge

The discharge is a helical copper coil resonator, with a resonance frequency of 300 MHz. It is directly above the cell, and is thermally anchored to the mixing chamber of the dilution refrigerator.

The inner discharge surfaces (coil and inside of the resonator) are primed with frozen molecular hydrogen during the cooldown of the cryostat. To prime the discharge with molecular hydrogen, the discharge is kept cold while the cell is heated above the hydrogen boiling temperature. This is to avoid hydrogen freezing on the cell window, which would fog it and prevent the Lyman-α from being detected by the MCP. One load of 50 torr·liters of hydrogen lasts for an entire cooldown of several months.

The discharge is located in a persistent current magnet at 4 tesla (the source magnet). The persistent current magnet maintains the discharge operation by trapping electrons and other charged particles in its field. The discharge must be re-activated after the source magnet magnet has been turned off. For the discharge to be activated, the source magnet must be ramped up to 4 tesla, and the discharge pulsed at higher powers and for longer times than usual. Sometimes the cell is heated to 1 K or higher to increase the helium vapor pressure in the discharge volume. If necessary, the 243 nm laser can also be shone onto the discharge to help activate it. The discharge, once activated, can be detected using two methods: looking down the dilution refrigerator laser beam tube, and seeing the Balmer-α glow, or detecting the Lyman-α and other light from excited hydrogen and helium atoms on the MCP.

To dissociate hydrogen for trapping, the discharge is pulsed at its resonant frequency of 300 MHz, at a temperature of roughly 300 mK. The frequency generator power is 3 dBm, and its signal is then amplified through an ENI 50 watt 50 dB rf amplifier [27]. The peak power of the pulses is between 10 and 30 watts. The discharge is pulsed on for 1 millisecond at 50 Hz (a 5% duty cycle) for a duration of 8 seconds total. The pulse frequency and duty cycle are flexible, the main quantity to preserve is the total discharge pulse time. During the discharge pulses, electrons trapped in the 4 tesla field collide with the molecular-hydrogen-coated surfaces. These collisions create a helium and molecular hydrogen gas. Collisions within this gas and with the ions dissociate some molecular hydrogen into atomic hydrogen. The helium-hydrogen mixture gas expands from the discharge into the cell region. This process is described in Greg Kochanski's PhD thesis [58]. For more information about the discharge, also see Tom Killian's PhD thesis [54].

2.3.2 The superfluid-helium-coated cell

The atoms expanding from the discharge are first cooled in the helium-coated cryogenic cell.

Double-walled G10 cell

The cell is a double-walled G10 (plastic) cylinder. The G10 tubes are coated on the outside with Stycast 1266 epoxy [28] and are superfluid-leak tight. Liquid helium fills the space between the two G10 cylinders, providing the thermal contact from the cell bottom to the cell top. The thermal conductivity of G10 is extremely low: the helium layer between the two G10 cylinders (or helium "jacket") maintains the cell at a constant temperature from bottom to top. The helium jacket allows rapid heating and cooling of the cell. The helium jacket is filled slowly through a low-thermal conductivity capillary line (see Appendix B on the jacket fill line design). The fill system poses the risk of causing the cell to explode if the liquid helium is heated too fast (faster than it can escape through the capillary). A relief outlet at the jacket-to-capillary joint, made of a bellows with a puncture disk, prevents this eventuality.

To do rf evaporation (described below in Section 2.5.2), rf radiation from the coils wound around the 4 K vacuum tailpiece that surrounds the cell must penetrate the cell. If the cell were made of high thermal conductivity metal, this would not be possible, which is why the cell material we chose was G10 [30].

The surface of the inner G10 tube is coated with a thin layer of copper to reduce stray electric fields in the cell. To allow the rf fields through the cell walls into the cell volume, the copper coating inside the cell is very thin, thinner than or on the order of the rf skin depth. The copper coating is uneven. It follows the underlying fiber structure of the G10, and resembles a grid. For more information on the cell construction, see Dale Fried's PhD thesis [30] and Stephen Moss's PhD thesis [79].

Helium film

The inside of the cell is coated with a slightly subsaturated superfluid liquid film, which also covers the inside of the discharge. The quality of the film is crucial to success in trapping, and I describe it in some detail.

The properties of superfluid helium are well described by Tilley and Tilley [105] and Pobell [85]. Superfluid helium will coat any surface it is in contact with, but the thickness d of the film is a decreasing function of height H

$$d \simeq \left(\frac{\alpha}{mgH}\right)^{1/n} \tag{2.1}$$

with g the gravitational acceleration, n is between 3 and 4, and α is a function of the substrate.

The cell is tall, 70 cm from the cell bottom window to the discharge. If the helium film is too thin, it becomes fragile and tears at the top of the cell when the discharge is pulsed. The superfluid film is also weakened by the addition of substantial quantities of ^{3}He.

The film tear effect can be seen on the bolometer as a very large negative signal (dropout) following a discharge pulse. This can be seen in Fig. 2-2, showing individual discharge pulses on the bolometer, with the dropouts indicating film tears. In this figure, the discharge is pulsed every second for 7.5 milliseconds, at a power of 3 dBm. In this case, the helium film had 10% ^{3}He. This effect is intermittent, probably dependent on the spatial distribution of ^{3}He in the cell, which is not necessarily uniform or constant, and on the individual discharge pulse (the discharge output varies from pulse to pulse).

The exact mechanism of the dropout signal is not understood. The bolometer is

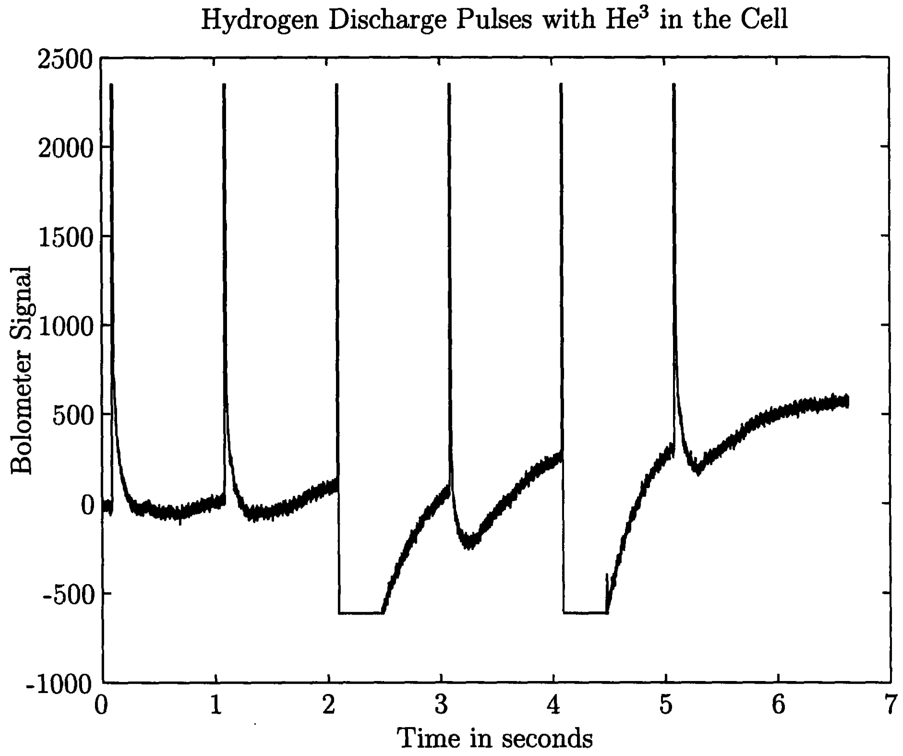

Figure 2-2: Helium film tears due to discharge pulses seen as dropouts on the bolometer. The film contains 10% ^{3}He, weakening the superfluidity. The flat part of the dropouts are due to railing of the bolometer readout electronics.

temperature controlled at a warmer temperature than the cell. Its signal rises when energy is deposited on it. It is possible that the helium vaporizing from the tear reaches the bolometer and *cools* it through thermal contact with the colder cell walls, thus causing a negative signal.

If the helium film is thin or covers the cell incompletely, the hydrogen atoms coming out of the discharge will bind permanently to the bare cell wall patches. This is a very large loss process.

2.3.3 Cooling and losses on the cell walls

The cell walls are heated to 300 mK, to minimize the residence time of hydrogen on the helium surface. Hydrogen recombination on the helium surface is a large loss process, which happens when the cell is not heated sufficiently and the hydrogen surface density and dwell time become large. A review of the recombination process has been given by Bell et al. [5].

Thermalizing with the cell walls

The cryogenic discharge at the top of the cell is pulsed. Each pulse generates dissociated hydrogen as well as vaporized helium atoms, which expand into the cell region.

The hydrogen collides with the gas of helium atoms and with the cell walls. It rapidly thermalizes to the temperature of the cell.

Hydrogen, deuterium, and tritium are special because they are not dissolved in liquid ^{4}He [94, 68]. Hydrogen and deuterium have known surface bound states on liquid ^{4}He. The bound state energy increases with mass.

Hydrogen atoms stick to the cell walls, because of the 1.1 K helium-surface binding energy E_b [77, 2, 95]. In the case where the hydrogen sample and helium wall are in thermal equilibrium, and the bulk and surface hydrogen are in equilibrium proportions the surface density σ of hydrogen is given by

$$\sigma_i = n_{i,\text{wall}}\,\lambda_{dB}\,\exp(E_b/k_BT) \tag{2.2}$$

where $n_{i,\text{wall}}$ is the bulk density of hyperfine state i near the wall, and $\lambda_{dB} = \sqrt{2\pi\hbar^2/mk_BT}$ is the thermal de Broglie wavelength.

Recombination and residence times on the helium surface

On the surface, hydrogen atoms thermalize at the cell wall temperature. However, if the hydrogen stays bound on the helium surface for too long, the surface density can become large enough that recombination occurs. The recombination rate is

$$\tau_{\text{rec}}^{-1} = \sigma l_c \bar{v}_s \tag{2.3}$$

where l_c is the cross length for recombination and $\bar{v}_s = \sqrt{\pi k_BT/2m}$ is the average speed of the surface atoms.

At equilibrium between the gas and surface hydrogen, the surface residence (or dwell) time can be described as the time it takes for all the adsorbed atoms to be replaced by bulk atoms. The surface residence time is given by

$$\tau_{\text{res}} = \frac{4\lambda_{dB}}{\bar{v}_g s}\exp(E_b/k_BT) \tag{2.4}$$

where $\bar{v}_g = \sqrt{8k_BT/\pi m}$ is the average speed of atoms in the gas, and s is the sticking probability of hydrogen on the helium surface.

The sticking probability of hydrogen was studied in detail in a similar cell by Yu et al. [118] and Doyle et al. [20]. The conclusion from these studies is that the sticking probability depends on the temperature, substrate, and film thickness. The sticking probability has not been measured in the current cell but can be assumed to be between 5% and 20 %.

The surface residence and recombination times are shown in Fig. 2-3. The upper right hand corner is the trap loading regime: the residence time is smaller than the recombination time. The lower left hand corner is the regime for wall-free magnetic confinement (see Section 2.4.2 below) and bolometric detection (see Section 2.6 below): the residence time is longer than the recombination time.

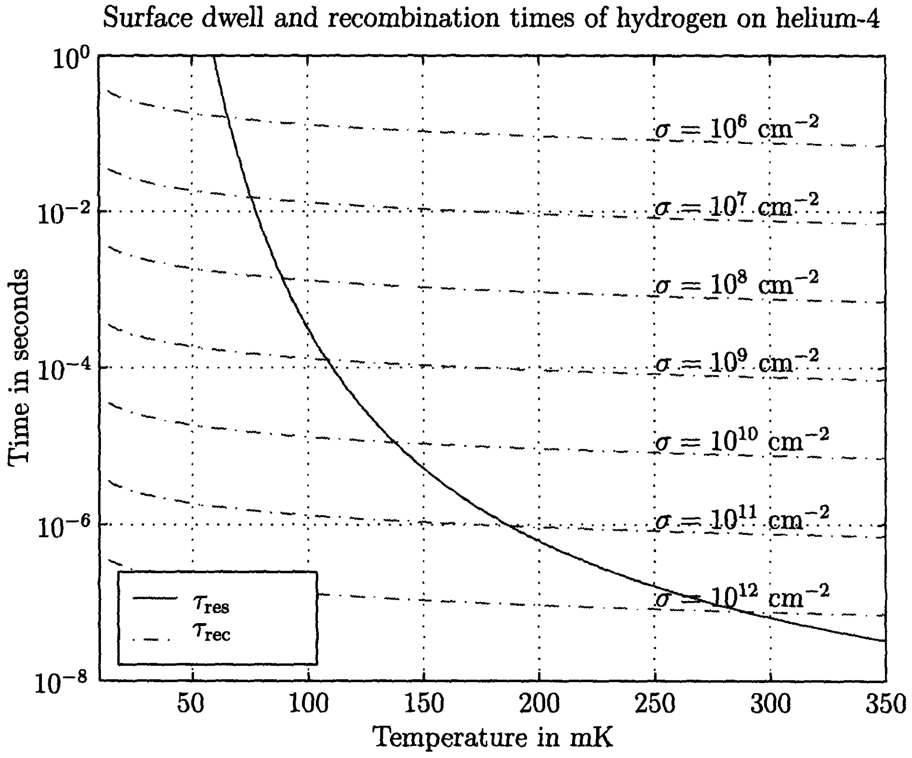

Figure 2-3: Surface residence and recombination times of hydrogen on ^{4}He, for difference surface densities σ, as a function of temperature. The value of the recombination cross length l_c used for the recombination time τ_{rec} is 0.21 Å. For the dwell time τ_{res}, the helium surface binding energy E_b is 1.11 K and the sticking probability is assumed to be 10 %. E_b and l_c are weighted averages from experimental values in table 4.2.

2.4 Trapping Spin-Polarized Hydrogen

2.4.1 Hydrogen in a magnetic field

Hydrogen atoms in a magnetic field can be in four different energy eigenstates, labelled $|a\rangle$, $|b\rangle$, $|c\rangle$ and $|d\rangle$ in order of increasing energy. The hyperfine Zeeman spectrum of $1S$ hydrogen is shown in Fig. 2-4. The lowest energy $|a\rangle$ state is high-magnetic-field seeking (its energy decreases with increasing magnetic field. Ideally, this state would be stably trapped in a magnetic field maximum, were it not impossible to create a magnetic field maximum in free space [116]. The doubly (electron and proton) spin-polarized stretched $|d\rangle$ state is metastable and can be trapped in a magnetic field minimum. Its interactions with the other spin states (spin-exchange) and with itself (dipolar decay) as a function of magnetic field are described by Stoof, Koelman and Verhaar [104].

At high magnetic fields, hydrogen separates into low ($|c\rangle$ and $|d\rangle$) and high ($|a\rangle$ and $|b\rangle$) field seekers. The high-field seekers follow magnetic field gradients to the largest possible magnetic fields to lower their energy, and the low-field seekers follow magnetic field gradients to the lowest possible magnetic field to lower their energy.

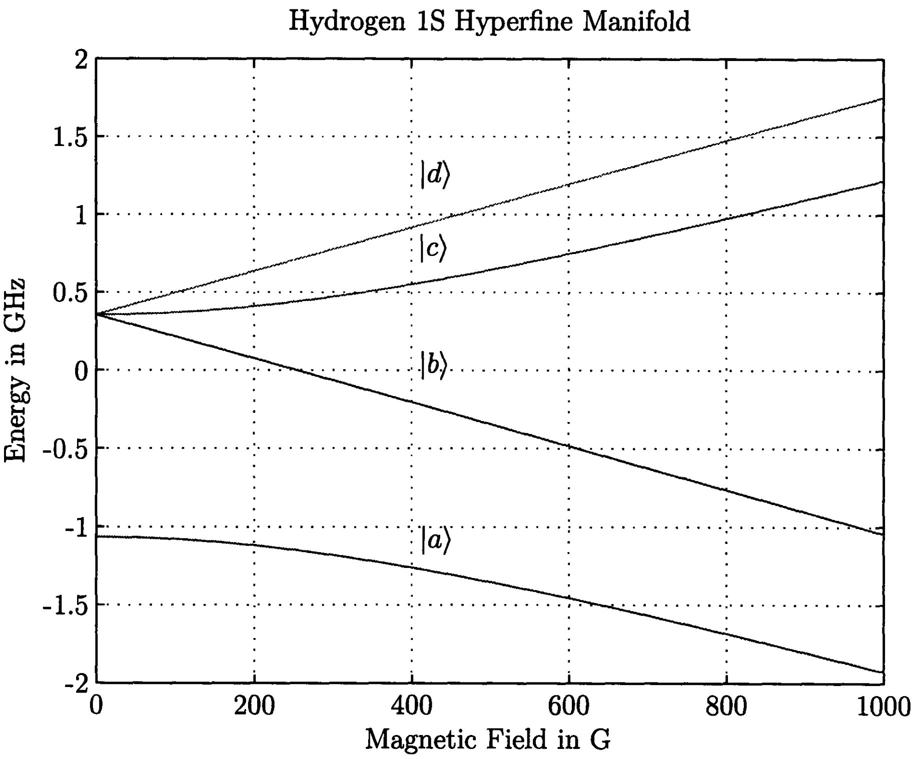

Figure 2-4: Hydrogen 1*S* hyperfine manifold. The uppermost state, the metastable doubly spin-polarized $|d\rangle$ state, is trapped in a magnetic field minimum. It is impossible to trap the stable $|a\rangle$ state, because it it impossible to create a magnetic field maximum in free space. Although both the $|d\rangle$ and $|c\rangle$ states are initially trapped in the magnetic field minimum, the $|c\rangle$ are removed through dipolar decay and spin-exchange collisions to untrapped states, and only $|d\rangle$ atoms remain.

The discharge creates all four states of hydrogen equally, only one of which is trapped.

2.4.2 Loading the magnetic trap

The fields of the trapping magnets and the loading magnet are raised before the discharge is run. The main trapping magnets are the upper and lower pinch magnets and the quadrupole magnet.

The upper and lower pinch magnets are coils that produce an 8300 G magnetic field above and below the trap region, axially confining the low-field-seeking atoms. The pinch magnets and their field and are shown in Fig. 2-5.

The quadrupole magnet consists of 8 vertical bars surrounding the cell, alternating positive-positive negative-negative currents, in a quadrupolar configuration. This produces a linear radial confining field for the low-field-seeking atoms, which is zero at the center of the trap and cell, and 9600 G at the cell walls.

The loading magnet is a coil located directly below the lower pinch, which produces a high field region at the cell bottom to prevent low-field-seeking atoms from accumulating there during the trap loading stage. The loading magnet is only raised

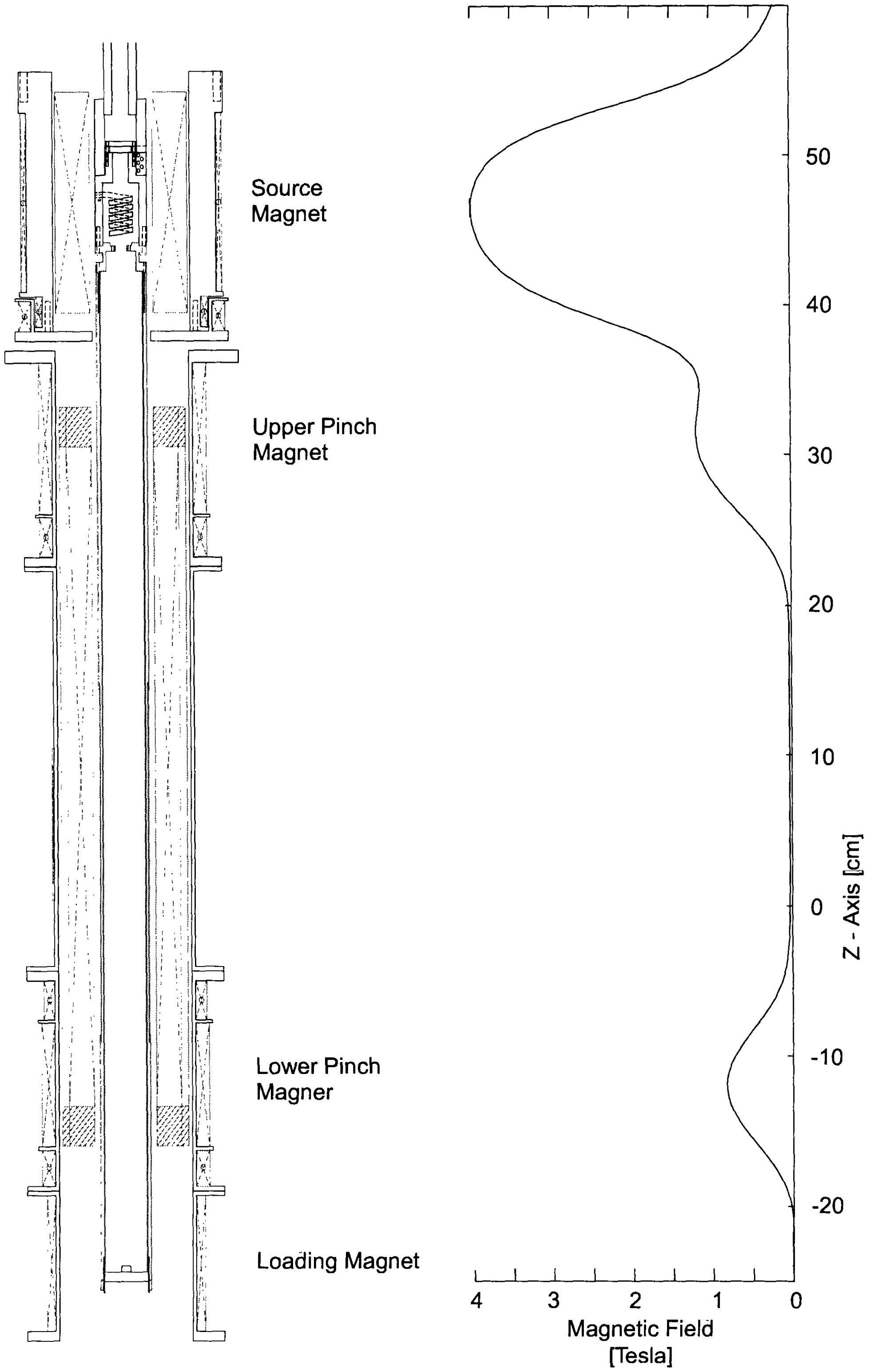

Figure 2-5: Magnet drawing and trap profile. This is the trap configuration after the loading magnet has been ramped down, at the start of magnetic evaporation.

during the trap loading, and is ramped down immediately afterwards to allow saddlepoint evaporation to occur (see Section 2.5.1 below).

The bias magnet is a long coil situated between the lower and upper pinches. A small constant field (2-5 G) is applied using the bias magnet to avoid zeroes in the trap, which would cause trap losses through adiabatic passage. The magnet system is described in more detail by John Doyle [22].

The other magnets, all horizontal coils, shape the vertical confining field.

When the low- and high- field-seeking hydrogen atoms are blown into the cell from the discharge and thermalize on the liquid helium walls, they experience different magnetic potentials. The high-field-seekers are pulled to the liquid helium walls by the quadrupole magnet field, and thus eventually stick until they recombine with other hydrogen atoms or are pulled back into the discharge, the location of the highest magnetic field. The low-field-seekers, in contrast, experience a local potential minimum in the magnetic trap, of a depth of approximately 620 mK. (The absolute minimum is the liquid helium surface potential of 1.1 K.) When the low-field-seekers unstick from the helium walls, they can have energy losing collisions with other atoms in the trap volume. If their energy falls below the 620 mK trap height, they are trapped in the magnetic potential.

Initially, the trapped sample is a mixture of roughly equal numbers of $|c\rangle$ and $|d\rangle$ state hydrogen atoms. The $|c\rangle$ state atoms decay very quickly through spin-exchange collisions as described in [104, 61], on a time scale of seconds. The $|d\rangle$ state atoms alone are left. These also decay to lower-energy high-field-seeking states through dipolar decay $d - d$ collisions [104]. The decay rate is proportional to the square of the density of the density of the $|d\rangle$ atoms At the trap loading density of $\sim 10^{12}$ cm^{-3}, the lifetime of the sample is on the order of one half hour, limited by this process.

The total number of trapped atoms depends on the discharge power and runtime, as well as the cell temperature, helium film thickness, and magnetic trap depth. However, there is no model that explains the loading process, in particular the upper limit on the number of atoms loaded into the trap.

The cell is cooled immediately after the discharge is run, going from 300 mK to below 100 mK in less than 20 seconds. This causes the helium vapor pressure to drop to negligible values, and shuts off the thermal contact between the trapped hydrogen sample and the cell walls. The confinement of the atoms then becomes "wall-free." The atoms which leave the trap through evaporation or other losses stick to the helium walls. At low temperatures, the residence time is much longer than the recombination time (see Section 2.3.3 and Fig. 2-3), and the probability of being re-emitted by the walls into the cell is very small. This is the desired regime for evaporative cooling.

The cell is cooled as rapidly as possible. Although the exact trap loading process is not understood, it is believed that there are regions of bad temperature where the helium walls become particularly "sticky," and the trapped sample still in thermal equilibrium with the walls suffers large losses [65]. At the same time as the cell cooling is initiated, the loading magnet is ramped down, allowing the start of saddlepoint magnetic evaporation.

2.5 Cooling Magnetically Trapped Hydrogen

2.5.1 Magnetic saddlepoint evaporation

The magnetically trapped doubly spin-polarized $|d\rangle$ state hydrogen is cooled through forced evaporation [43, 69]. The barrier formed by the lower pinch magnet at the bottom of the trap is lowered progressively. The most energetic atoms escape over the barrier, and the remaining ones redistribute their energy through collisions, thereby lowering the overall temperature of the sample.

As described by Luiten, Reynolds and Walraven [66], as well as Ketterle and van Druten [53], there is an optimal timescale for the forced evaporation. The time cannot be too fast, since the sample must be allowed to rethermalize during the evaporation. The timescale also cannot be too slow, since the sample is depleted through the dipolar decay two-body process. The thermalizing collisions are often called 'good' collisions, and the dipolar decay collisions are often called 'bad.' The colder atoms are in the lower, higher density part of the trap. The 'bad' collisions are not only a loss process, they tend to selectively remove colder atoms from the sample.

In this way, the 'bad' collisions are a heating mechanism. The cooling through forced evaporation must compete effectively with this heating, maximizing the number of atoms remaining in the trap.

Evaporative cooling is ultimately used with all atoms that are cooled to the quantum regime. Hydrogen, unfortunately, is difficult to cool by evaporation, because its elastic cross section is much smaller than typical cross sections for other atoms [53].

The saddlepoint evaporation over the lower pinch barrier is effective only above approximately 150 μK. This cooling method is inherently one-dimensional: only atoms with a large enough energy in the axial direction of the trap are removed. At lower energies, the mixing between dimensions through thermalizing collisions happens too slowly, and the evaporation shuts off. At the end of the magnetic evaporation stage, the sample has a density of 10^{14} atoms per cubic centimeter, and a temperature of 150 μK.

2.5.2 Hyperfine resonance rf evaporation

After the magnetic evaporation is no longer effective, rf evaporation is used to lower the temperature and increase the phase space density of the sample. Rf evaporation was first proposed by Pritchard, Helmerson and Martin [87]. The principle is simple and ingenious: use the hydrogen hyperfine spectrum to selectively remove atoms at certain magnetic fields by driving the $|d\rangle$ to $|c\rangle$ transition. At low enough fields (below 50 G), the $|c\rangle$ atoms are untrapped, and simply expand or fall out of the trap to the helium walls. As the frequency is decreased, so is the selected magnetic field and the trap edge.

This method of evaporation is clearly three-dimensional, since any atom resonant with the rf is removed, as long as the geometry of the magnetic field and rf polarization allows it. The cell has two separate rf coils wound around it on the 4 K vacuum tailpiece, one providing an axial rf field (axial coil) and one providing a radial or transverse rf field (transverse coil). These coils, as well as the mechanism of rf evaporation, are described in detail in Dale Fried's PhD thesis [30].

The magnetic component of the rf field must be perpendicular to the magnetic trapping field for the transition to be excited. Thus if an atom is energetic in the radial direction, the rf field should be applied axially (using the axial rf coil). If an atom is energetic in the axial direction, a transverse rf field should be applied (using the transverse rf coil). The probability of the transition can be calculated using the Landau-Zener formalism [63, 120, 109].

In this way, very cold, dense hydrogen samples, containing a hydrogen Bose condensate [31, 30] are obtained.

2.6 Use and Characterization of the Bolometer

The bolometer is our main diagnostic tool for detecting trapped atoms and understanding the helium film.

2.6.1 Operation of the bolometer

The bolometer is a heat-sensitive graphite resistance deposited on a thin quartz crystal. The quartz plate is thermally isolated from the rest of the cell; it is suspended by nylon threads at the bottom of the cell (below the lower pinch magnet). It is covered by a superfluid helium film replenished slowly along the nylon threads. The construction on the bolometer is described in detail in the PhD thesis of David Landhuis [65].

The bolometer is kept warmer than the cell, between 200 and 350 mK. It is actively controlled using an external resistance bridge which applies a bias voltage across it to keep it at a constant temperature. The drop in the power necessary to keep the bolometer at a fixed temperature (eg heating) is recorded as a voltage change.

The bolometer can be used to measure the superfluid ^{4}He film thickness (see Section 2.6.5), detect the presence of ^{3}He in the cell (see Section 2.6.6), and measure properties of the trapped atoms (see Section 2.6.2). The bolometer can also be used to measure the magnetic field of the trap bottom up to 50 G (see Section 3.3.1 for details).

The bolometer detects the 4.5 eV recombination energy of atomic hydrogen to molecular hydrogen on its surface. The atoms must be removed from the trap before they can be detected on the bolometer.

The means of removing the atoms from the trap can be magnetic or rf evaporation, or simply dumping the atoms out of the trap into the cell bottom region by rapidly lowering the lower pinch magnet's field.

The atoms arrive in the cell bottom, stick to the cold helium walls, and recombine with each other when their surface density is large enough. The molecular hydrogen deposits some of the recombination energy on the local helium surface, and proceeds to bounce around the cell bottom depositing rotational and vibrational energy on helium surfaces until it finally stops and is absorbed by the cell surface under the helium film [22]. The bolometer detects a fraction of the total recombination energy of the atoms released from the magnetic trap. This fraction is assumed to be constant, independent of most other parameters associated with the loading and decay of the hydrogen sample.

2.6.2 Bolometric density measurement

By comparing dumped atom signals of successive identical traps, only changing the delay time before the lower pinch magnet is lowered, the density of atoms in the trap can be measured. The integrated dump signal is proportional to the total atom number, and the main loss process is the two-body decay rate. The number of atoms in the trap thus varies as two-body decay equation

$$\dot{N}_{\rm dip} = -g\left(\frac{V_2(T)}{V_1^2(T)}\right)N^2(t) \tag{2.5}$$

where g is the decay constant, and $V_k = \int {\rm d}r^3 \exp(-k\, U(\mathbf{r})/k_BT)$ is an effective volume dependent on the potential $U(\mathbf{r})$. Assuming a constant sample temperature, equation 2.5 can be solved to show that N varies inversely with time

$$\frac{N(0)}{N(t)} = 1 + (1+\xi f)\frac{V_2(T)}{V_1(T)} g n_0(0) t. \tag{2.6}$$

$n_0(0)$ is the peak density in the trap at time $t = 0$, and the factor $(1 + \xi f)$ corrects for the evaporation and dipolar decay losses during the wait time t. ξ is the ratio of elastic to inelastic collisions, and f is the fraction of elastic collisions in which an atom escapes from the trap. This correction factor can be expressed in terms of the trap geometry and thermodynamic quantities [34]

$$1 + \xi f = \frac{\eta + \beta - 3/2 - \delta/2}{\eta + \beta - 3/2 - \delta}. \tag{2.7}$$

η is the ratio of the trap height to the sample temperature, and is usually between 8 and 11 [30]. β is the average fractional energy, in units of k_BT, that is removed from the sample by an evaporating atom. Our group as well as Luiten, Reynolds and Walraven [66] have shown β to be close to 0.8 for a cylindrical quadrupole trap and η values found in our experiment. δ is a geometrical quantity defined by ${\rm d}V_1 \propto U^{\delta-1}{\rm d}U$. Different values of δ are shown in table 2.1 for different trap geometries. Our trap can be taken to be axially harmonic and cylindrically linear (quadrupole) at trap bottom fields below 10 G, and spherically harmonic at trap bottom fields above 50 G or very low temperatures. We use the cylindrical quadrupole value of $\delta = 2$ (the axial confinement approximated as a box) for the density measurement.

Since the theoretical decay constant $g = 1.2 \times 10^{-15}$ cm^3/s is known the sample density can be measured, with a uncertainty on the order of 20%. This uncertainty arises from not knowing the trapping fields accurately.

δ for different trap geometries		
Dimension	Harmonic	Linear
1	1/2	1
2	1	2
3	3/2	3

Table 2.1: Geometrical factor δ for different trap geometries

2.6.3 Recombination sensitivity to cell temperature

The bolometer requires a low cell temperature to detect hydrogen recombination efficiently. At high temperatures (above 100 mK), the dwell time of hydrogen on a ^{4}He surface is shorter than the recombination time for most surface densities (see Fig. 2-3). This makes surface recombination inefficient: atoms will be re-emitted into the cell rather than stick on the surfaces and recombine. At temperatures below 100 mK, however, the dwell time is longer than the recombination time, and efficient surface recombination occurs.

The temperature dependence of the bolometer's sensitivity to hydrogen recombination is shown in Fig. 2-6. The data are taken with identical amounts and fluxes of hydrogen from the trap, but changing the temperature of the cell during the magnetic dump. The atom flux into the cell bottom region is estimated to be 10^{10} cm^{-2}·sec^{-1}.

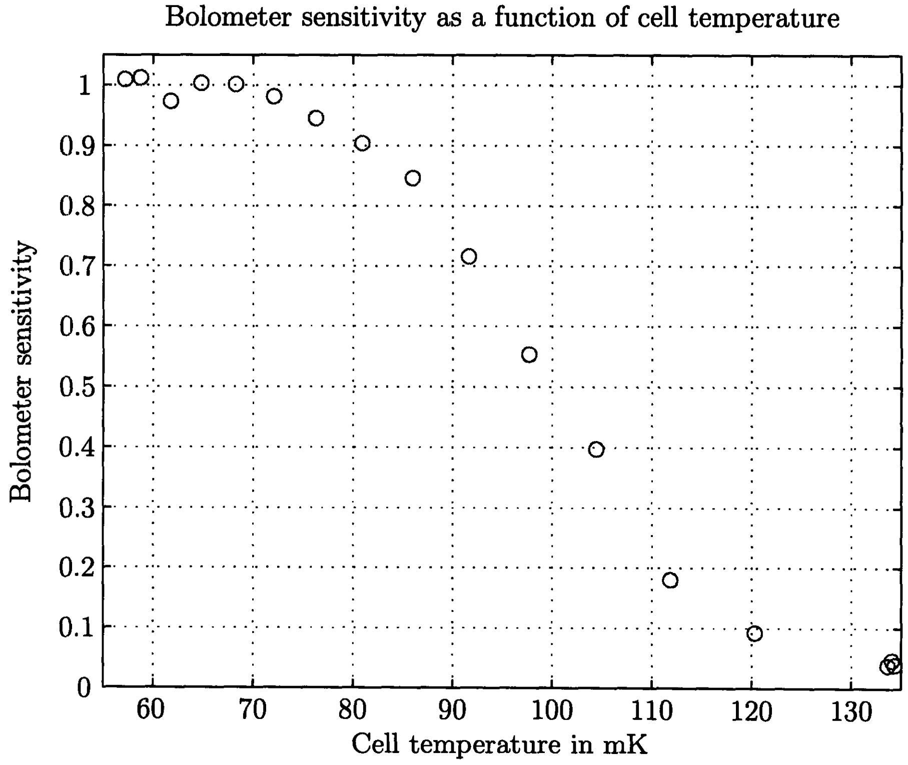
Bolometer sensitivity as a function of cell temperature

Figure 2-6: Bolometer sensitivity as a function of the cell temperature (pure ^{4}He film)

2.6.4 Recombination sites in the cell

Since the bolometer is usually significantly warmer (350 mK) than the cell (below 100 mK) during detection, recombination is less likely to happen on its surface (see Section 2.3.3). Hence the recombination signal comes mostly from hydrogen recombining on the cold cell walls. Molecular hydrogen is known to form in excited ro-vibrational states, and being non-magnetic, bounces around the cell depositing recombination energy on different helium surfaces, including the bolometer [22].

We can estimate how close the recombination site needs to be to the bolometer by dumping the atoms out of the trap using two different methods: by lowering the lower pinch magnet, which dumps the atoms into the cell bottom where the bolometer is located, or by lowering the quadrupole magnet, which dumps the atoms laterally onto the cell walls 10-30 centimeters above the bolometer. It should be taken into account that the cell surface available to the atoms is smaller in the first case (lower pinch dumping), which should increase the recombination rate.

The bolometer data in Fig. 2-7 shows magnetic field dumps done with very warm samples, right after the trap is loaded (before any forced evaporative cooling is done). Detection of hydrogen recombination in the cell bottom (below the lower pinch) is found to be approximately 10 times more efficient than recombination on the cell walls (above the lower pinch) by comparing the area under the curves.

The energy deposition of recombining hydrogen evidently is localized as a function of cell height. This is not surprising given the large height to diameter ratio of the cell.

2.6.5 Measuring the helium film thickness

The helium film thickness can be measured using the bolometer. Since the bolometer is weakly connected to the cell through thin nylon threads, it takes a finite time for the film on its surface to replenish. By running a current through the bolometer, the film is burnt off the crystal substrate. When the film is removed, the bolometer heats, and the voltage accross it (at constant current) drops suddenly as the resistance decreases. By measuring the duration of the film burnoff and voltage across the bolometer, we can calculate the total energy required to burn the film off the surface. By repeating this measurement for different current values, one can take into account the replenishment of the film during the burnoff time itself and find the energy required to burnoff the film instantaneously. The film thickness measurement is described in more detail in the PhD thesis of Ite Albert Yu [119].

Since ^{3}He is not superfluid, and hence does not replenish on the bolometer surface, it cannot be measured through the film burnoff method. However, it's presence can be detected with the bolometer in other ways.

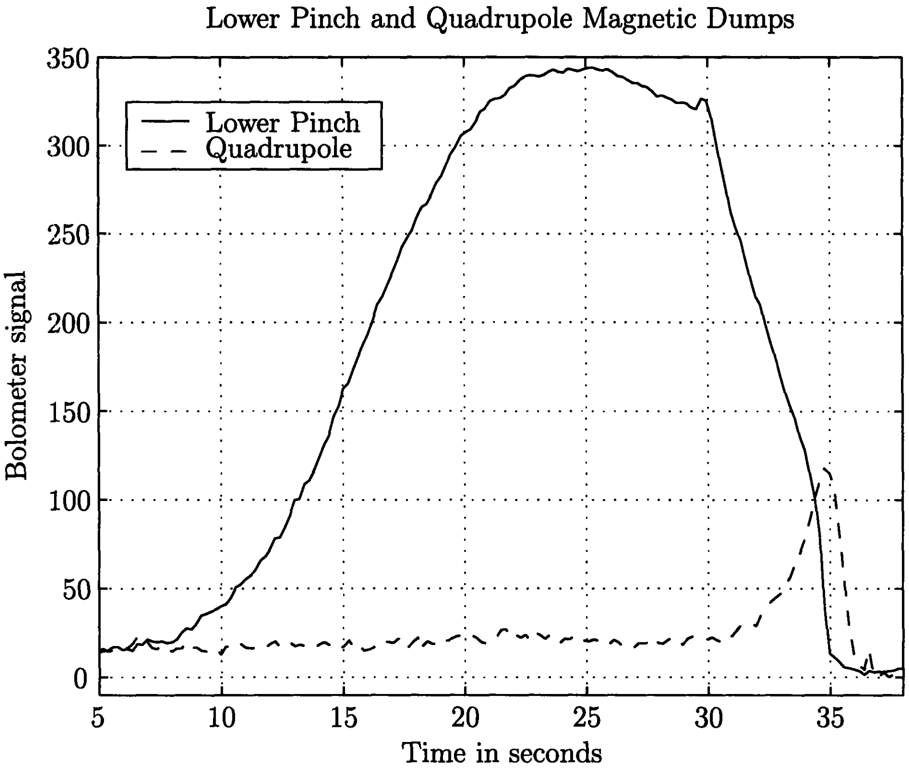

Figure 2-7: Bolometer signal from lower pinch and quadrupole magnet dumps: the total number of atoms trapped is the same for both curves. The area under the curves is proportional to the number of atoms detected. The area under the lower pinch curve is 10 times larger than that under the quadrupole curve. This demonstrates that the bolometer detects hydrogen that recombines in the cell bottom region roughly 10 times more efficiently than hydrogen that recombines on the cell walls above the lower pinch barrier.

2.6.6 Detecting ^{3}He in the cell

^{3}He-^{4}He mixtures at low temperatures

The low temperature quantum-mechanical properties of ^{3}He and ^{4}He are such that below 870 mK temperature, liquid ^{3}He and ^{4}He phase separate, with a ^{4}He rich solution below a pure ^{3}He liquid (see for instance Pobell [85].) Thus we can create a ^{3}He film covering our cell walls by simply adding ^{3}He to a ^{4}He film.

Lower binding energy of hydrogen and deuterium on ^{3}He

A ^{3}He film is interesting because hydrogen (and deuterium) have lower binding energies on ^{3}He than ^{4}He. Hence adding ^{3}He to the cell will modify the trap loading process, allowing us to load the trap at lower temperatures. Because of the lower binding energy, however, the bolometer temperature sensitivity to recombination will also be shifted to lower temperatures, since the residence time on the helium film is shorter (see Section 2.6.3 and Fig. 4-3).

Detecting ^{3}He in the cell

We cannot measure the quantity of ^{3}He in the cell the same way we measure ^{4}He (described above in Section 2.6.5).

As mentioned above, in Section 2.6.1, the temperature of the bolometer is actively controlled through an external resistance bridge circuit. A bias voltage is applied across the bolometer to keep it at a constant temperature. The bias voltage depends on the value of the set resistance in the bridge circuit, Thus the bolometer has a characteristic $R_{\mathrm{bridge}} - V_{\mathrm{bias}}$ curve. (This curves changes with the intrinsic resistance of the bolometer, and thus would be different from bolometer to bolometer.)

The presence of any ^{3}He in the cell will change the temperature control characteristics of the bolometer because of the higher vapor pressure and stronger thermal link to the cell walls. The temperature control regime can be characterized by measuring the $R_{\mathrm{bridge}} - V_{\mathrm{bias}}$ curve. The $R_{\mathrm{bridge}} - V_{\mathrm{bias}}$ curves are thus indicators of the presence of ^{3}He in the cell. This can be seen in Fig. 2-8.

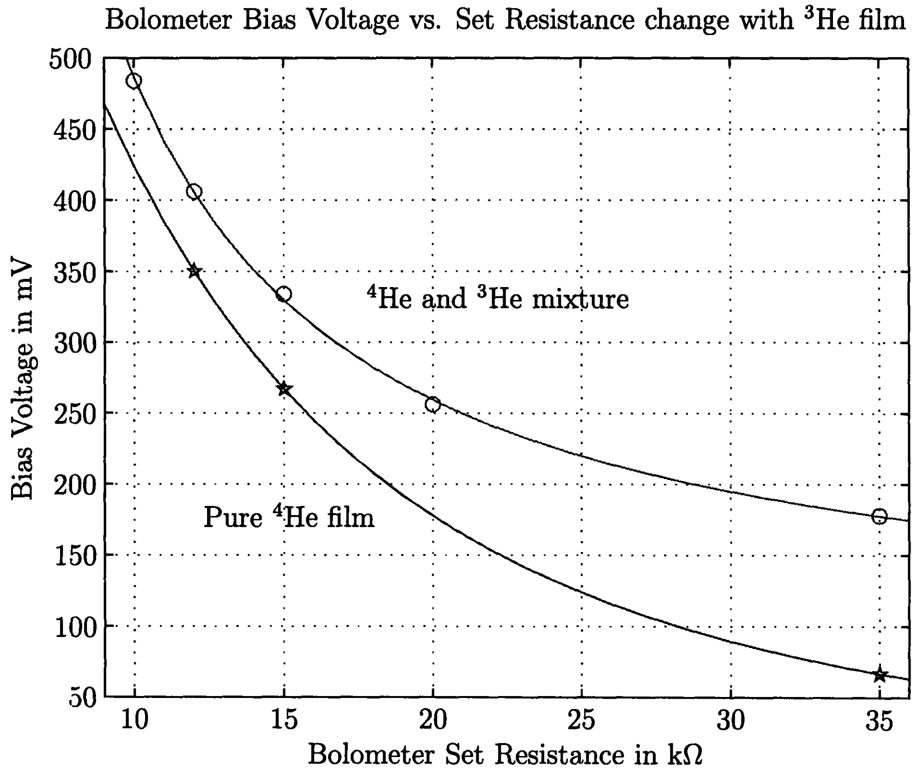

Figure 2-8: Change in the bolometer bias voltage V_{bias} vs. set resistance R_{bridge} curves in the presence of ^{3}He in the cell. The upper curve (with ^{3}He) changes a little depending on the ^{3}He concentration, but is also variable with time. The two curves are always very different if any ^{3}He is present in the cell. Because of the time variability, possibly due to non-uniform ^{3}He distribution in the cell, these curves cannot be used to measure the ^{3}He concentration or the ^{3}He -^{4}He ratio. However, they can be used to detect the presence or absence of ^{3}He in the cell.

Difficulty removing ^{3}He from the cell

While doing experiments on the effect of ^{3}He on trap loading, it would be useful to be able to remove and add ^{3}He at will. It is very easy to remove the ^{4}He film from the cell, simply by pumping on the capillary line going to the cell.

However, using the ^{3}He detection method described above, we understood that it is not possible to simply pump out ^{3}He from the cell through the capillary line as with ^{4}He. ^{3}He is not superfluid and does not flow through capillaries easily. Instead, the cell must be heated above 4 K to pump out all the ^{3}He as a gas, a lengthy and risky process since it also requires emptying the superfluid helium jacket surrounding the cell (see Section 2.3.2 and Appendix B).

2.7 $1S - 2S$ Detection of Hydrogen

Two-photon $1S - 2S$ spectroscopy is used to measure properties of the trapped gas such as temperature, density, and the presence of a Bose condensate.

2.7.1 The 243 nm laser system

A Krypton ion laser pumps a 486 nm (Coherent 699) dye laser, which is locked to an external reference cavity using the Pound-Drever-Hall locking technique [24]. In this way, 500 milliwatts of blue 486 nm light are generated, with a linewidth of 1 kHz. This light is then coupled into a bowtie doubling cavity, where it is passed many times through a BBO doubling crystal [81], generating 10-20 milliwatts of 243 nm laser light that is sent into the cell and reflected back from a retro-mirror at the bottom of the cell. The focus of the laser beam is designed to be close to the center of the magnetic trap.

For more detailed information on the laser system and principle of $1S - 2S$ detection, see the PhD theses of Jon Sandberg, Claudio Cesar, and Thomas Killian [96, 9, 54]. A summary description can also be found in Cesar et al. [11]. Further investigations of the complexities of $1S - 2S$ spectoscopy and interactions can be found in Killian et al. [55] (cold collision frequency shift), Cesar and Kleppner [10] (Doppler free feature), and Landhuis et al. [64] (inelastic collisions of 2S atoms).

A recent problem of damage of our BBO crystal is detailed in Appendix A.

2.7.2 Exciting the sample

The $1S$ hydrogen atoms are excited to the $2S$ state by absorbing two photons. Since this transition conserves angular momentum, the resulting $2S$ atoms are also in the magnetically trapped $|d\rangle$ state, and experience the same potential as the $1S$ atoms. As long as the photons do not impart significant momentum to the atoms, they remain trapped.

2.7.3 The $1S - 2S$ spectrum

The two photons absorbed by a $1S$ atom can be either part of the same laser beam (propagating in the same direction) or each from a separate laser beam (incoming and outgoing, counter propagating). The first type of excitation is Doppler-sensitive, and the atom's velocity determines the frequency of photons that can be absorbed. It is also recoil-shifted to the blue with respect to the resonance frequency due to momentum conservation [54].

Using the Doppler sensitive spectrum, a direct measurement of the velocity distribution, and hence temperature, can be made. This is only possible for temperatures below roughly 150 μK, however, otherwise the signal width is too large, and the signal strength too weak.

The second type of excitation is Doppler-free, and much stronger at any temperature, since the transition probability is independent of the atom's velocity. This type of excitation imparts no momentum to the atoms, and they remain trapped. The lineshape is complex, but can be modelled as a double-exponential, whose width depends on the temperature of the sample. Another factor is the $1S - 2S$ cold-collision density shift [55], which red shifts the resonant frequency with density. For more information about the Doppler-free lineshape, see Killian [54] and Section 3.4.

2.7.4 $1S - 2S$ Excitation rate and sample decay

The two-photon $1S - 2S$ transition has a small excitation probability. The strongest $1S - 2S$ signal (the peak of the Doppler-free spectrum) is estimated to excite at most 10^8 atoms per millisecond laser pulse. In this sense the $1S - 2S$ spectroscopy is non-destructive and allows study of the sample in real time (unlike the bolometer magnetic trap dumps).

However, the $1S - 2S$ spectroscopy destroys the sample faster than can be explained either by the excitation rate or the two-body dipolar decay. The laser beam heats the retromirror at the bottom of the cell and boils off the helium there, as well as any helium replenishing the boiled-off film. This causes the trapped sample to heat and decay through background helium gas collisions.

Several alternate construction schemes have been proposed to limit this process. One possibility is to place the mirror on a thin support, limiting the flow of helium and hence the boiloff rate during the spectroscopy. An alternative is to place a heater around the mirror base, and heat it sufficiently to remove helium slightly before and during the spectroscopy. Although the total amount of helium boiled off is still large in this case, it is boiled off in the direction of the cell bottom walls, rather than vertically up to the trapped sample. Another scheme involves a combination of these two techniques. These may become especially attractive or even necessary as new lasers for $2S - nS$ are introduced, with further losses in the retromirror, and more heating.

Chapter 3

2S Hyperfine Spectroscopy of Hydrogen

3.1 Introduction and Motivation

Spectroscopy of hydrogen has been used to advance the understanding of atomic and quantum physics since the earliest days of quantum mechanics. From the discovery of the Balmer series in 1885 to the failure of the Schrödinger and Dirac theories to predict features of the hydrogen spectrum such as the Lamb shift, detailed study of the hydrogen spectrum has inspired and challenged theoretical atomic physics.

The theory of quantum electrodynamics (QED) has had many successes in explaining and calculating features of the hydrogen spectrum. The current status of high precision experiments on hydrogen, deuterium, muonium and positronium, as well as the anti-hydrogen experiments, are all pushing calculations of QED theory to its limits (see Karsheboim and Ivanov [52] and references therein). However, the structure of the proton (requiring quantum chromodynamics, QCD) poses a severe obstacle to comparing theory and experiment of the structure of hydrogen.

In particular, in the most precise test of QED - the Lamb shift in the 1S state - the experimental uncertainty is 7.5×10^{-6} whereas the theoretical uncertainty is estimated to be 4.8×10^{-6} (Weitz et al. [114]). The proton size contribution is estimated to be 3.9×10^{-6}, one of the largest sources of uncertainty.

3.1.1 Comparing the 1S and 2S hyperfine splittings to test QED

Karsheboim and Ivanov [52, 51] have pointed out that by comparing the hyperfine splitting in the 1S and 2S states, the proton size correction vanishes, permitting a number of QED radiative and relativistic tests to be examined critically. The quantity of interest,

$$D_{21} \equiv 8 f_{\mathrm{HFS}}(2S) - f_{\mathrm{HFS}}(1S), \tag{3.1}$$

is the weighted difference between the 1S and 2S hyperfine splittings f_{HFS}. In the absence of QED and relativistic effects, $D_{21} = 0$. D_{21} includes mainly radiative cor-

Measured	$f_{\rm HFS}(2S)$
Heberle, Reich and Kusch (1956) [42]	177 556 860 (50) Hz
Rothery and Hessels (2000) [93]	177 556 785 (29) Hz
Kolachevsky et al. (2004) [62]	177 556 860 (15) Hz
Calculated	$f_{\rm HFS}(2S)$
Karshenboim and Ivanov (2002) [52, 51]	177 556 838.1(4) Hz

Table 3.1: Measured and calculated values of the 2S hyperfine splitting frequency. The experimental and theoretical values are in good agreement. However, the estimated error in the theoretical calculation is much smaller than the experimental error. More precise measurements are required to test the QED calculation.

rections and relativistic terms. D_{21} can be calculated by purely QED methods to a high order of precision: the QCD proton contributions vanish.

The hydrogen hyperfine splitting in the 1S state has been measured many times very precisely [88, 25], and is the one of the most accurately known quantity in physics with a with a fractional uncertainty of 6×10^{-13} [29]. (The most accurately known quantity in physics is currently the hydrogen 1S-2S transition frequency measured by Udem et al. [107] and Niering et al. [80].)

Hence the accuracy of D_{21} depends entirely on the accuracy with which $f_{\rm HFS}(2S)$ can be measured. The 2S hyperfine interval has been measured by using rf techniques in 1956 by Heberle, Reich and Kusch [42] and in 2000 by Rothery and Hessels [93]. More recently, Kolachevsky et al. [62] measured $f_{\rm HFS}(2S)$ optically by comparing the absolute frequencies of the 2-photon transition from the $1S$ to the $2S(F = 1, m = 0)$ and $2S(F = 0, m = 0)$ states. This optical result is the most precise to date, and involves the difference of two large frequencies rather than a direct frequency measurement. These results are summarized in Table 3.1.

A theoretical value for $f_{\rm HFS}(2S)$ has also been calculated by Karshenboim and Ivanov [52, 51] via the quantity

$$D_{21} = 8 f_{\rm HFS}(2S) - f_{\rm HFS}(1S) = 48953(3)\text{Hz} \tag{3.2}$$

and the extraordinarily well known 1S hydrogen hyperfine splitting energy [88]. This value is also shown in Table 3.1.

Precise measurements of hyperfine structure are almost invariably made by measuring transition frequencies between field-independent states, such as the $(F = 1, m = 0) \rightarrow (F = 0, m = 0)$ states in hydrogen (the $|c\rangle$ and $|a\rangle$ states in the notation of Fig. 3-1). In these states, the transition frequency varies quadratically with magnetic field at low field. All the experiments previously mentioned measured the hyperfine splitting at zero or very small magnetic field. However, in our studies with magnetically trapped ultracold hydrogen, such a transition is unsuitable.

The current chapter will describe an attempt by the MIT ultracold hydrogen group to use our ultracold metastable spin-polarized 2S hydrogen sample to measure the 2S hyperfine splitting $f_{\rm HFS}(2S)$ by rf spectroscopy. In our situation, a $|c\rangle \rightarrow |a\rangle$

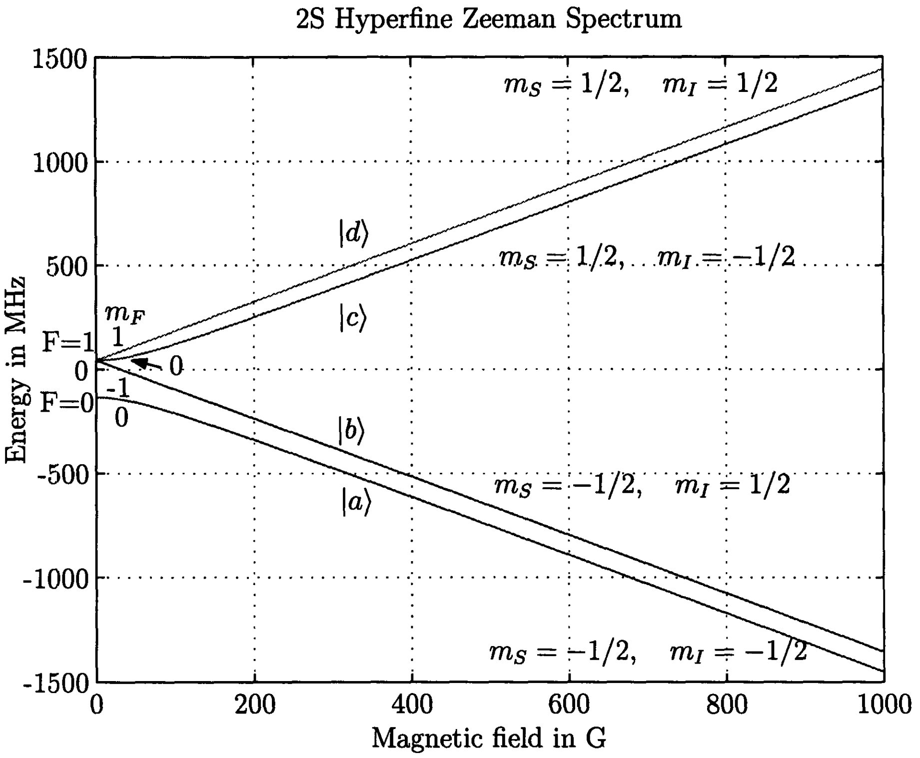

Figure 3-1: Hyperfine Zeeman structure of the hydrogen 2S state.
The four states are labelled $|a\rangle$ to $|d\rangle$ in order of increasing energy, as for the 1S hyperfine structure. The good quantum number as low fields (F and m_F) and high fields (m_S and m_I) are indicated.

transition is unsuitable, because we trap $|d\rangle$ state atoms in non-zero magnetic fields, and the $|c\rangle \rightarrow |a\rangle$ measurement requires a magnetic field as close to zero as possible. Although it would be possible to transfer some of the 2S $|d\rangle$ population to the 2S $|c\rangle$ state, the $|c\rangle$ state is only weakly trapped in our magnetic minimum potential, and can very easily fall out of the trap (the average trap thermal energy is enough for a $|c\rangle$ state atom to leave the trap). Moreover, the large $f_{\mathrm{HFS}}(2S)$ transition frequency of 178 MHz could not be applied in our trap without an extensive redesign.

Our strategy is to measure the 2S $|d\rangle \rightarrow |c\rangle$ transition at a point where the frequency is field independent, approximately 810 G. The transition frequency, 82 MHz, is approximately half $f_{\mathrm{HFS}}(2S)$. Knowledge of the 2S $|d\rangle \rightarrow |c\rangle$ transition frequency at the field-independent point is sufficient to determine $f_{\mathrm{HFS}}(2S)$. (Note that the magnetic field itself does not need to be measured separately.)

The hyperfine frequency can be extracted from the data in a straightforward fashion using the Breit-Rabi formula, as explained in Section 3.2.1. This formula involves the electron and proton Landé g-factors. There is, however, a complication. At the level of precision needed for the measurement, relativistic and bound state corrections to the g-factors are important. The Landé g-factor corrections, which are described in Section 3.2.4, are non-trivial.

This experiment was our group's first endeavor to do high precision spectroscopy on our ultracold 2S hydrogen sample. Future experiments will focus on the 2S-8S transition [115], referencing this transition energy to the 1S-2S using an optical frequency comb. These efforts are very promising. The knowledge gained in the pursuit of the high-field 2S hyperfine measurement can be used in these future experiments. In particular, this chapter pays special attention to systematic effects in our temperature and magnetic field estimates. Both of these quantities will be important to characterize completely to analyze the $2S-8S$ data properly.

3.1.2 Summary of the experimental procedure

The essential steps of the experiment are as follows (with more details below).

- The trap is loaded with 1S atoms, with a low magnetic field trap bottom.
- The trap bottom is raised to 810 G, adiabatically.
- Trapped 2S $|d\rangle$ state atoms are created by two-photon excitation at 243 nm.
- An rf field at approximately 82 MHz is applied to excite the 2S $|d\rangle$ to $|c\rangle$ transition.
- Because both the 2S $|d\rangle$ and $|c\rangle$ states are trapped, the transition is detected by depopulating one or the other state by driving the $2S-3P$ transition, using a 656 nm laser system.
- The remaining atoms are detected by quenching the 2S state by applying an electric field, then observing the emitted Lyman-α photons on a MicroChannel Plate (MCP) detector.
- The 2S $|d\rangle$ to $|c\rangle$ transition is scanned by repeating the procedure at different rf frequencies until the trap is depleted.
- The entire process is repeated at a series of magnetic fields.
- By measuring the transition spectrum as a function of magnetic field, the maximum transition frequency is found. This corresponds to the field-independent point transition (see Fig. 3-5).

Trapping, cooling and raising the magnetic field

The main source of broadening in the 2S $|d\rangle \rightarrow |c\rangle$ transition is the magnetic field broadening from the trap field. Thus the colder the 2S sample, the narrower the transition.

The 2S sample is at the same temperature as the 1S sample. Thus we must start from a cold 1S sample. Unfortunately, we cannot do magnetic or rf forced evaporation from a high magnetic field trap.

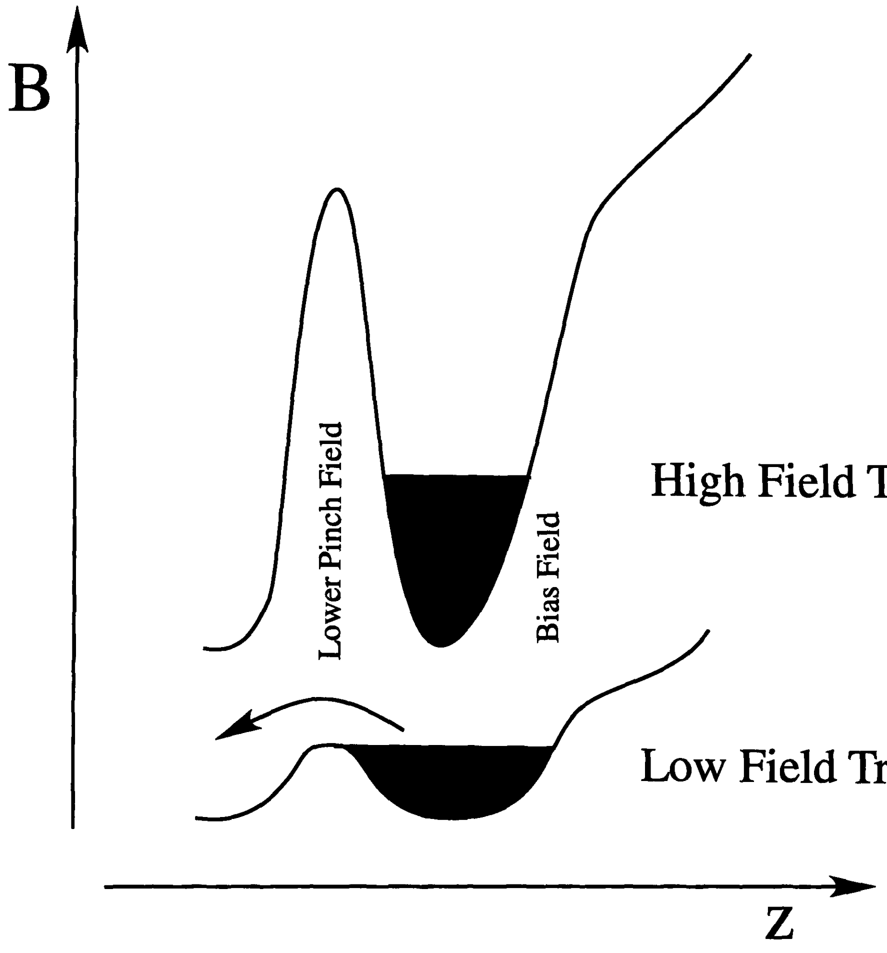

Figure 3-2: Schematic of high and low field traps. The high field trap is a wedge between the large slopes of the bias and lower pinch magnets. Magnetic evaporation happens over the lower pinch barrier, as indicated for the low field trap, and is impossible in the high field configuration.

Our magnet design does not allow us to add a constant magnetic field to the entire trap. Instead, we need to raise both the bias magnet and the lower pinch to reach the required field of 810 G (a schematic of the low and high field traps is show in Fig. 3-2). Since the magnetic evaporation requires the *lowering* of the lower pinch, clearly magnetic evaporation at high fields is out of the question. Hyperfine rf evaporation is equally impossible. At 810 G, the 1S $|d\rangle \rightarrow |c\rangle$ transition frequency is far too large for our coils. Moreover the 1S $|c\rangle$ state atoms are also trapped at such high fields; thus we would require a second, larger rf frequency to excite the $|c\rangle \rightarrow |b\rangle$ transition, or else the removal of atoms from the trap would be too slow to be efficient for forced evaporation.

Thus we first trap and cool the 1S $|d\rangle$ state atoms in a low magnetic field trap, and then raise the magnetic field of the trap in a controlled manner to 810 G, changing the potential adiabatically (see Section 3.4.4).

Magnet configuration at low and high fields

In effect, our high field magnetic trap is formed by the slopes of the lower pinch magnet (from below) and bias magnet (from above), with the lower pinch contribution being roughly 300 G and the bias contribution being roughly 500 G at the trap bottom. This is a markedly different situation from the low magnetic field trap. In our low magnetic field trap, the vertical confinement is provided by the lower pinch and middle lower coils below, and the middle upper coil above. The bias magnet contributes only a small field gradient, and is run at 0.1 or 0.2 A, compared to 40 A at high magnetic fields. Fig.3-3 shows the trap model results for a low and high field trap.

The magnetic trap shape as well as the vertical trap position are expected to be very different at low and high fields. Particularly worrisome is the axial compression of the trap resulting from the two very large slopes of the lower pinch and bias. Such compression causes sample heating and thus magnetic field broadening. Using our magnetic field model, computed from the known magnet coil geometry and the Biot-Savart law (see Appendix G of Dale Fried's PhD thesis [30]), we estimated that we could use the smaller (middle upper, middle lower, middle lower compensation) coils to mitigate the axial trap compression. By varying the relative fraction of the bias and lower pinch contributions, moreover, we can move the trap center up and down vertically, and thus move the trap center to coincide with the fixed laser focus.

However, as described in Section 3.3, we discovered that our magnetic trap model is inaccurate, probably due to incorrect recording of our coil geometries. We try to use the characteristics of the $1S-2S$ spectrum to optimize the sample temperature and trap shape. This is non-trivial due to systematics of the $1S-2S$ double-exponential lineshape described in Section 3.4. The uncertainties in trap shape and sample temperature are severe impediments to optimizing the experiment for observing the 2S $|d\rangle$ to $|c\rangle$ transition.

2S $|d\rangle \rightarrow |c\rangle$ transition and detection

Some of the high magnetic field 1S $|d\rangle$ state atoms are excited through two-photon excitation to the 2S $|d\rangle$ state. We then drive the 2S field-independent point $|d\rangle \rightarrow |c\rangle$ transition. The rf B-field component should be perpendicular to the trap field. Since the high magnetic field is mostly along the vertical axis, we use the transverse rf coil. The rf coils and their normal use for hyperfine evaporation are described in Section 2.5.2.

The 2S $|c\rangle$ and $|d\rangle$ atoms are trapped in the same magnetic potential close to the field independent point. The $|c\rangle$ atoms normally decay through spin-exchange collisions, however the timescale for this is on the order of seconds. This means that on the timescale of the lifetime of the 2S atoms (roughly 80 milliseconds in our trap), our usual detection process of quenching the 2S atoms and detecting the emitted Lyman-α photon detects both the $|c\rangle$ and $|d\rangle$ state atoms.

We developed a new technique by which we could selectively detect one or the other of the 2S hyperfine states. This is done by driving the $2S-3P$ transition on one of the states to remove it from the trap, and then quench and detect the remaining

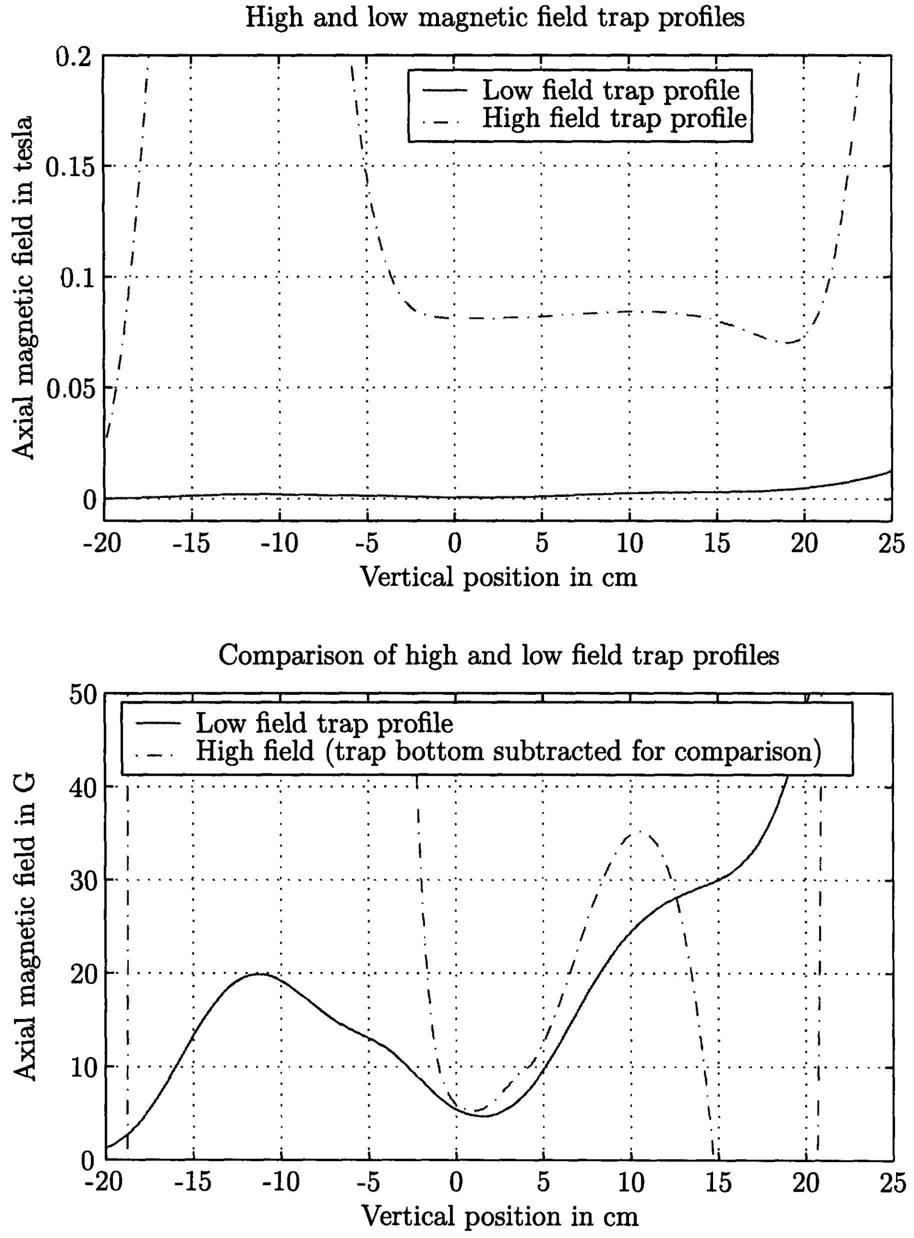

Figure 3-3: Axial magnetic field profiles of low and high field traps.
The low field trap is used at the end of the magnetic evaporations. Both profiles are given by a magnetic field model that we know to be inaccurate. However the main features at high fields are clear. The first is the extremely large barrier below the trap formed by the lower pinch magnet. The second is the axial compression in the trap (shown clearly in the second plot, compared to the low field trap profile). The high field trap axial confinement is created by the slopes of the lower pinch magnet (from below) and bias magnet (from above). This results in a very large axial trap frequency, probably underestimated by the trap model.
The vertical position of the trap bottom, crucial for overlap of the sample and the laser beam focus (estimated to be at 0 cm on the plots) is also uncertain.

state. The natural linewidth of the $2S_{1/2} - 3P_{3/2}$ transition is 20 MHz, smaller than the 82 MHz field-independent transition frequency separating the 2S $|d\rangle$ and $|c\rangle$ states at 810 G.

By depleting the 2S $|d\rangle$ state atoms using the $2S-3P$ transition, we can study the change in 2S $|c\rangle$ population produced by varying the rf frequency, and thus expect to see the 2S signal detected on the MCP increase when going through the transition. Vice-versa, if depleting the 2S $|c\rangle$ state atoms, we can expect to see a depletion in the 2S signal on the MCP when sweeping the rf through the transition.

The ultimate goal of doing spectroscopy of the 2S manifold was not possible in our current experiment, however a better magnetic field design could make it possible in the future.

3.2 Theory of the 2S Hyperfine Spectrum

The fully relativistic quantum-mechanical treatment of spin 1/2 particles is the Dirac equation. However, the Dirac picture uses classical electric and magnetic fields. The complete interaction of an electron with fields requires QED, which can be incorporated in the Dirac or other equations as radiative corrections. The Hamiltonian we use is not derived from the Dirac equation, and thus requires relativistic as well as radiative corrections. These are described in the section on the Landé electron and proton g-factors (section 3.2.4).

The Hamiltonian for a one-electron atom in a magnetic field $\mathbf{B}$ can be written

$$\begin{aligned} H &= ah\mathbf{I}\cdot\mathbf{J} - \vec{\mu}_N\cdot\mathbf{B} - \vec{\mu}_J\cdot\mathbf{B} & (3.3)\\ &= ah\mathbf{I}\cdot\mathbf{J} - g_I\mu_B\mathbf{I}\cdot\mathbf{B} + g_J\mu_B\mathbf{J}\cdot\mathbf{B} & (3.4)\end{aligned}$$

where ah is the hyperfine splitting energy, $ah = h\cdot f_{\mathrm{HFS}}$. $\mathbf{I}$ is the intrinsic spin angular momentum of the proton nucleus, and $\mathbf{J} = \mathbf{S} + \mathbf{L}$ is the total (intrinsic spin and orbital) angular momentum of the electron. For the S states, $L = 0$ and $\mathbf{J} = \mathbf{S}$. $\mu_B = \frac{e\hbar}{2m_e c}$ is the Bohr magneton in esu, g_J is defined as

$$g_J = \frac{\mathbf{L}\cdot\mathbf{J} + g_e\mathbf{S}\cdot\mathbf{J}}{|\mathbf{J}|^2}. \tag{3.5}$$

For S states $g_J = g_e \simeq 2$. $g_I = g_N\frac{m_e}{m_N} \ll g_J$ is the nuclear Landé g-factor weighted by the electron-to-nucleus mass ratio. For hydrogen,

$$g_I = \frac{m_e}{m_N}g_N = \frac{m_e}{m_p}g_p \simeq 5.6\frac{m_e}{m_p}. \tag{3.6}$$

3.2.1 The Breit-Rabi formula

The framework for calculating the 2S $|d\rangle \to |c\rangle$ transition frequency in relation to the 2S hyperfine frequency $f_{\mathrm{HFS}}(2S)$ is the Breit-Rabi formula.

The total angular momentum of the atom is $\mathbf{F} = \mathbf{J} + \mathbf{I}$. In a small magnetic field **J** and **I** are mostly parallel to **F**, hence F and m_F are good quantum numbers. $(2I+1)ah/2$ is the hyperfine splitting, the energy difference between the $F = I + 1/2$ and $F = I - 1/2$ states at zero field.

The S-state $J = S = 1/2$ Hamiltonian (equation 3.4) energies are given by the Breit-Rabi formula [8, 74],

$$W(F, m_F) = -\frac{ah}{4} - g_I\, \mu_B\, B\, m_F \pm (2I+1)\frac{ah}{4}\sqrt{1 + \frac{4\, m_F\, x}{2I+1} + x^2}, \tag{3.7}$$

where the positive sign is for $F = I + 1/2$, the negative for $F = I - 1/2$, and $m_F = \pm I \pm 1/2$. The parameter x is the ratio of the paramagnetic Zeeman energy to the hyperfine splitting energy:

$$x = \frac{2}{(2I+1)} \frac{(g_e + g_I)\mu_B\, B}{ah}. \tag{3.8}$$

For hydrogen, $I = 1/2$. The hyperfine spectrum of the hydrogen 2S manifold is shown in Fig. 3-1, along with the good quantum numbers in the low and high field limits.

3.2.2 Eigenstates

The zero-field eigenstates of the hydrogen atom are the triplet and singlet $|F, m_F\rangle$ states, which can be written in the $|m_S, m_I\rangle$ basis:

$$\begin{aligned} |1,1\rangle &= |+,+\rangle \\ |1,0\rangle &= \sqrt{\frac{1}{2}}(|+,-\rangle + |-,+\rangle) \\ |1,-1\rangle &= |-,-\rangle \\ |0,0\rangle &= \sqrt{\frac{1}{2}}(|+,-\rangle - |-,+\rangle). \end{aligned} \tag{3.9}$$

At any field, we can express the eigenstates of the Hamiltonian of equation 3.4 for $J = S = 1/2$ in terms of the $|F, m_F\rangle$ basis:

$$\begin{aligned} |d\rangle &= |1,1\rangle \\ |c\rangle &= \cos(\theta)|1,0\rangle + \sin(\theta)|0,0\rangle \\ |b\rangle &= |1,-1\rangle \\ |a\rangle &= \sin(\theta)|1,0\rangle - \cos(\theta)|0,0\rangle, \end{aligned} \tag{3.10}$$

where θ is set by

$$\tan(\theta) = \frac{1 - \sqrt{1 + x^2}}{x}, \tag{3.11}$$

and x is defined in equation 3.8.

3.2.3 Field-independent points

The hydrogen S-state hyperfine spectrum contains field-independent points, where

$$\frac{\mathrm{d}}{\mathrm{d}B}\left(W(F_1, m_{F1}) - W(F_2, m_{F2})\right) = 0. \tag{3.12}$$

The best known of these is the hyperfine splitting at $B = 0$, between the two $m_F = 0$ states, but there are two other field-independent points at higher magnetic fields:

$$\begin{aligned} \tfrac{\mathrm{d}}{\mathrm{d}x}\left(W(1,1) - W(1,0)\right) &= \tfrac{\mathrm{d}}{\mathrm{d}x}\tfrac{ah}{2}\left(1 + x\left(\tfrac{g_e - g_I}{g_e + g_I}\right) - \sqrt{1+x^2}\right) = 0 \\ \tfrac{\mathrm{d}}{\mathrm{d}x}\left(W(1,-1) - W(0,0)\right) &= \tfrac{\mathrm{d}}{\mathrm{d}x}\tfrac{ah}{2}\left(1 - x\left(\tfrac{g_e - g_I}{g_e + g_I}\right) + \sqrt{1+x^2}\right) = 0 \end{aligned} \tag{3.13}$$

both at

$$x_0 = \left(\left(\frac{g_e + g_I}{g_e - g_I}\right)^2 - 1\right)^{-1/2} \simeq 12.81. \tag{3.14}$$

The magnetic field corresponding to x_0 is

$$B_0 = \frac{ah}{\mu_B(g_e + g_I)}\left(\left(\frac{g_e + g_I}{g_e - g_I}\right)^2 - 1\right)^{-1/2}. \tag{3.15}$$

$B_{0,nS}$ scales as $B_{0,1S}/n^3$ (like ah). Thus the 1S manifold, two field-independent points are at a magnetic field of 6482 G, while in the 2S manifold, they are at 810 G (see Fig. 3-4 for the $|d\rangle \rightarrow |c\rangle$ transition), which is experimentally accessible in our apparatus.

The field-independent transition frequency f_{FIP} between the two upper hyperfine states $|d\rangle$ and $|c\rangle$ at x_0 is

$$f_{\mathrm{FIP}} = \frac{f_{\mathrm{HFS}}}{2}\left(1 - \frac{2\sqrt{y}}{1+y}\right) = 0.922162618\frac{f_{\mathrm{HFS}}}{2}, \tag{3.16}$$

where $y = g_I/g_e$. This frequency is dependent only on the hyperfine splitting f_{HFS}, the ratio of the hydrogen (bound) electron and proton Landé g factors, and the ratio of the masses of the electron and proton (through $g_I = g_p(m_e/m_p)$). Thus a measurement of f_{FIP} in the 2S manifold is equivalent to a measurement of $f_{\mathrm{HFS}}(2S)$ as long as the Landé g factors and the proton-to-electron mass ratio are well known.

Around B_0, $\nu(B)$ is approximately parabolic (see Fig. 3-5), with a curvature given by

$$\left.\frac{\partial^2\nu}{\partial B^2}\right|_{B_0} = \frac{1}{2}\frac{((g_e + g_I)\mu_B)^2}{ah\,h}(1 + x_0^2)^{-3/2} \equiv \beta \simeq -10.462\frac{\mathrm{Hz}}{\mathrm{G}^2}. \tag{3.17}$$

This approximation is useful for calculating the magnetic broadening and lineshape of the expected signal.

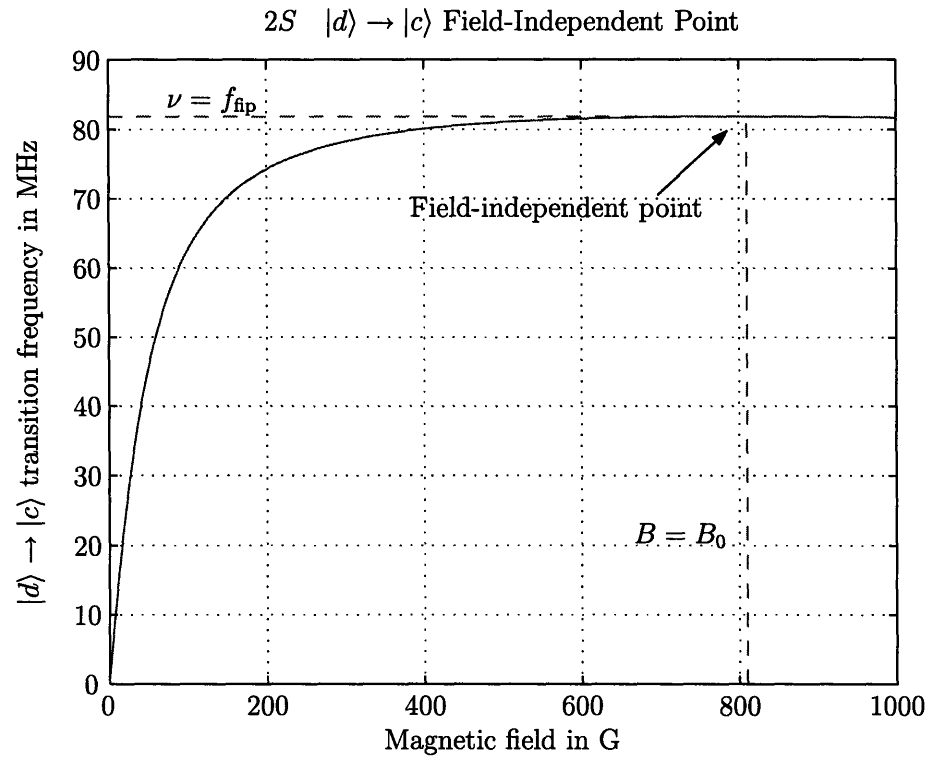

Figure 3-4: The 2S field-independent point between $|d\rangle$ and $|c\rangle$.

3.2.4 Corrections to the Landé electron and proton g factors

The electron g factor g_e can be calculated entirely from QED. There are two sources of contributions that cause it to differ from the Dirac equation value of 2: the anomalous magnetic moment of the free electron, and bound state corrections of the electron bound to a nucleus (the nucleus could be hadronic as in hydrogen, or leptonic as in positronium).

The proton g factor g_p is not a calculable quantity for QED, but a measured value of the Standard Model. It also has bound state corrections to its measured free value, and these can be calculated.

The anomalous magnetic moment of the electron

The anomalous magnetic moment of the electron arises from radiative corrections, which take into account interactions of the electron with itself through photon emission-absorption, and photon-electron-positron processes. The electron magnetic moment anomaly, $a_e = (g_e - 2)/2$ was calculated to first order in the fine structure constant $\alpha = e^2/\hbar c$ by Schwinger [98],

$$a_e = \frac{g_e - 2}{2} = \frac{\alpha}{2\pi} + A^{(4)}\left(\frac{\alpha}{\pi}\right)^2 + A^{(6)}\left(\frac{\alpha}{\pi}\right)^3 + \ldots \tag{3.18}$$

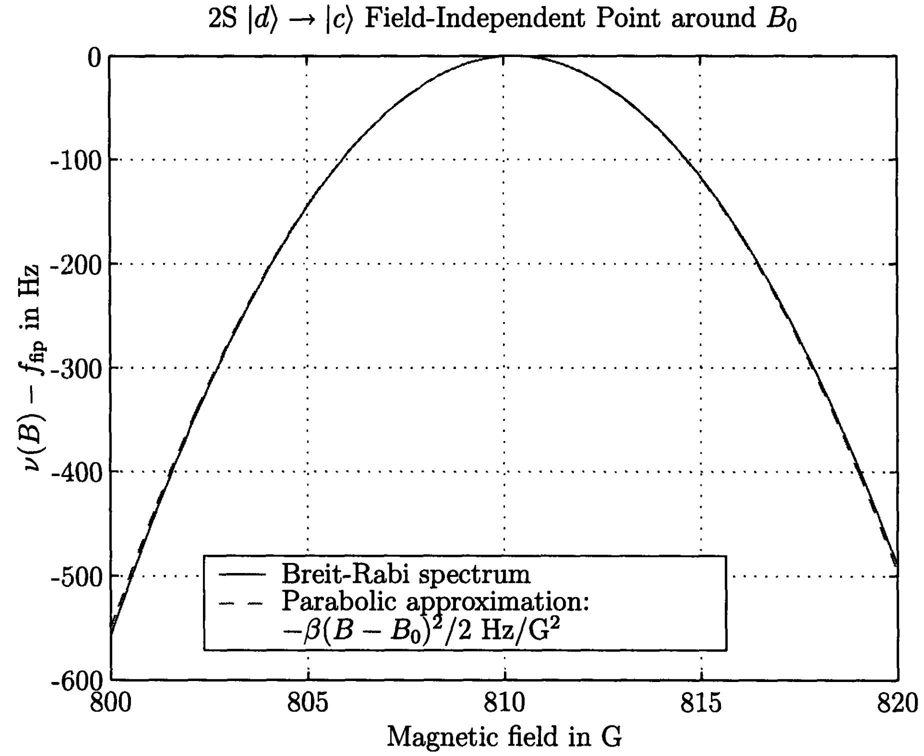

Figure 3-5: The 2S $|d\rangle$ to $|c\rangle$ transition around field-independent point. Close to the field-independent point, the transition can be well approximated by a parabola, whose curvature is given by equation 3.17.

The current status of the experiments and calculations of the anomalous moment of the electron are overviewed by Kinoshita [56]. The QED calculated and experimentally measured values agree to a high level of accuracy. The uncertainty in the measured value of the fine structure constant α is the limiting factor in comparing experiment and theory, and thus the comparison of theoretical and experimental values of a_e can be reinterpreted as a measurement of α [56]. The recommended value of g_e from the 2002 CODATA database [76] is included in Table 3.2.

Bound state corrections for the electron magnetic moment

The binding of the electron to the proton in hydrogen contributes several types of corrections to the Landé g factor. The most important of these is a relativistic correction, accounting for the larger effective mass of the electron due to its bound state kinetic energy. This correction is dependent on the energy and angular momentum (n and L state) of the electron, and decreases with larger n (larger orbitals imply smaller kinetic energy). The first few correction terms in $(Z\alpha)$ were calculated for the 1S state by Grotch and Hegstrom [35]. The generalization to higher n and l states was done by Grotch and Kashuba [36] analytically, and more recently by Anthony and Sebastian [1].

The analytic results given by [36] are

$$\begin{aligned} g_J = \quad & \tfrac{3J(J+1)-L(L+1)+3/4}{2J(J+1)} - \tfrac{m_e}{m_N}\tfrac{J(J+1)+L(L+1)-3/4}{2J(J+1)} + \tfrac{\epsilon}{m_e}\tfrac{4J(J+1)+1}{4J(J+1)} \\ & + \tfrac{\epsilon}{m_e}\tfrac{m_e}{m_N}\tfrac{-3J(J+1)-L(L+1)-3/4}{2J(J+1)} + a_e\tfrac{J(J+1)-L(L+1)+3/4}{J(J+1)} \\ & + a_e\tfrac{\epsilon}{m_e}\tfrac{-2J(J+1)+2L(L+1)+1/2}{2J(J+1)} + a_e\tfrac{\epsilon}{m_e}\tfrac{m_e}{m_N}\tfrac{4J(J+1)-4L(L+1)-1}{2J(J+1)} \end{aligned} \tag{3.19}$$

where $\epsilon = -(m_e/2)(Z\alpha/n)^2$ is the non-relativistic infinite-nuclear-mass electron binding energy. The relativistic $a_e(\epsilon/m_e)$ terms should use $a_e = \alpha/2\pi$ (first order in α) to be consistent in the expansion of α. The other term in a_e should use the expansion in equation 3.18 to third order, with the expansion coefficients from Kinoshita [56].

The numerical value computed by Anthony and Sebastian [1] using this formula and their own calculations, as well as a new numeric value computed using the 2002 CODATA [76] constant values are shown for the 1S as well as 2S states in Table 3.2. The Anthony and Sebastian values [1] date from 1994, and thus are pre-CODATA 1998 [75], and use the CODATA 1986 values [13].

Landé g factor of the proton in hydrogen

The g factor for the proton is based on an experimental measurement of the dimensionless ratio

$$\frac{\mu_e(\mathrm{H})}{\mu_p(\mathrm{H})} = \frac{g_e(\mathrm{H})}{g_p(\mathrm{H})}\frac{\mu_B}{\mu_N} = \frac{g_e(\mathrm{H})}{g_p(\mathrm{H})}\frac{m_p}{m_e} = \frac{g_e(\mathrm{H})}{g_I(\mathrm{H})} = 658.2107058(66) \tag{3.20}$$

by Winkler, Kleppner, Myint and Walther [117] in 1972, and is the best measured value to date. In this relation,

$$\mu_p = \frac{1}{2}g_I\mu_B = \frac{1}{2}g_p\mu_N \tag{3.21}$$

where $\mu_N = e\hbar/2m_pc$ and $g_I = (m_e/m_p)g_p$ (as in equation 3.6). From this we get the 1S hydrogen bound state value of g_p from the 1S hydrogen bound state value of g_e and the proton-to-electron mass ratio.

From this quantity, Karshenboim [50] derives the free proton g factor:

$$\frac{g_p}{2} = \frac{\mu_p}{\mu_N} = 2.792847353(28). \tag{3.22}$$

The bound 2S state proton g factor can then be found from the relations in [1] or [36]. I will use the relation of Grotch and Kachuba [36] since it is more compact:

$$\begin{aligned} g_p = \quad & 2(1+a_p)\left\{1 + \tfrac{\epsilon}{mZ}\left[1 - \tfrac{m_e}{2m_p}\left(\tfrac{3+4a_p}{1+a_p}\right)\right]\right. \\ & \left.\times\left[1 - \tfrac{1}{4J(J+1)}\left(\tfrac{J(J+1)-I(I+1)+F(F+1)}{F(F+1)-J(J+1)+I(I+1)}\right)\right]\right\}, \end{aligned} \tag{3.23}$$

where $a_p = (g_p - 2)/2$ (of the free g_p) and $F = J + I$ is the total angular momentum of the atom.

Values obtained using this formula are shown in Table 3.2.

3.2.5 Calculating the Field-Independent Point Transition Frequency

To estimate which frequency interval to scan in order to measure $f_{\mathrm{FIP}}(2S)$, we will use the measured and calculated values of $f_{\mathrm{HFS}}(2S)$ in Table 3.1.

Landé g factors

When calculating $f_{\mathrm{FIP}}(2S)$, care must be taken to use the corrected values of g_e and g_p for the 2S state in hydrogen (see Section 3.2.4 for details). However, as can be seen in Table 3.2, there are 3 different options for both g_e and g_p.

We can compare the g_e and g_p values for the hydrogen 1S state in Table 3.2 with the precisely measured quantity $\mu_e(H)/\mu_p(H)$ [117], see section 3.2.4. The quantity can be computed as

$$\frac{g_e}{g_p}\frac{m_p}{m_e}. \tag{3.24}$$

Table 3.3 summarizes the results of this comparison. The fractional error is taken as

$$\left(\frac{g_e}{g_p}\frac{m_p}{m_e} - \frac{\mu_e(H)}{\mu_p(H)}\right) \Big/ \frac{\mu_e(H)}{\mu_p(H)}. \tag{3.25}$$

The values of g_e and g_p calculated using the CODATA 2002 [76] constant set and the analytic expressions of Grotch and Kashuba [36] perform comparably to the others, (using old CODATA 1986 values for the proton-electron mass ratio [13]), matching the measured value within the experimental uncertainty. This indicates that it is safe to use these values within the CODATA 2002 framework of constants to predict the value of the 2S $|d\rangle$ to $|c\rangle$ field-independent frequency. If one used the other g factor values with CODATA 2002 constants, a significant error would be made.

We find

$$f_{\mathrm{FIP}}(2S) = 81\,868\,149(14)\mathrm{Hz}, \tag{3.26}$$

where the 2S hyperfine splitting frequency obtained by Kolachevsky et al. [62] was used. The uncertainty is mostly due to the error in the 2S hyperfine splitting measurement (2σ estimate).

The uncertainty due to the Landé g factors values contributes less than 1 Hz. Thus a measurement of the field-independent $2S$ $|d\rangle$ to $|c\rangle$ transition frequency f_{FIP} is indeed equivalent to a measurement of the 2S hyperfine splitting at low magnetic fields. In this sense our proposed experiment provides an interesting new avenue for measuring the zero-field hyperfine splitting, with experimental factors (and not the conversion factor) dominating the experimental error.

Name	Value	Relative Uncertainty
Electron g factor (g_e)		
Free [76]	2.0023193043718(75)	3.8×10^{-12}
Bound: H 1S [36, 1]	2.0022838524	1×10^{-9}
Bound: H 1S [1]	2.0022838524	1×10^{-9}
Bound: H 1S [36, 76]	2.0022838531	1×10^{-9}
Bound: H 2S [36, 1]	2.0023104409	1×10^{-9}
Bound: H 2S [1]	2.0023104409	1×10^{-9}
Bound: H 2S [36, 76]	2.0023104416	1×10^{-9}
Proton g factor (g_p)		
Free [76]	5.585694701(56)	1.0×10^{-8}
Bound: H 1S [36, 1]	5.58559572	1×10^{-7}
Bound: H 1S (F=1) [1]	5.58559572	1×10^{-7}
Bound: H 1S (F=1) [36, 76]	5.58559565	1×10^{-7}
Bound: H 2S (F=1) [36, 1]	5.58567001	1×10^{-7}
Bound: H 2S (F=1) [1]	5.58567001	1×10^{-7}
Bound: H 2S (F=1) [36, 76]	5.58566994	1×10^{-7}
Electron Magnetic Moment Anomaly a_e[76]	0.0011596521859(38)	3.2×10^{-9}
Proton $a_p = (g_p - 2)/2$ [76]	1.7928473505(28)	1.6×10^{-8}
Proton-to-electron mass ratio m_p/m_e [76]	1836.15267261(85)	4.6×10^{-10}

Table 3.2: Electron and proton Landé g factors in hydrogen, and related quantities. The first two of the bound state numerical values are taken from Anthony and Sebastian [1], using CODATA 1986 values [13] and theoretical calculations from Anthony and Sebastian [1] and Grotch and Kashuba[36]. The third value is calculated here from the results of Grotch and Kashuba [36] and CODATA 2002 physical constant values [76]. It is important to know the corrected (bound state) g factor values, consistent with the CODATA 2002 physical constants, for estimating the 2S field-independent transition frequency.

Reference used	$\frac{g_e}{g_p}\frac{m_p}{m_e}$	Fractional error
Winkler, Kleppner, Myint and Walther [117]	658.2107058	1×10^{-8}
CODATA 2002 [76] (free g factor values)	658.2106862	-3×10^{-8}
Grotch and Kashuba, Anthony and Sebastian [36, 1]	658.2107061	4×10^{-10}
Anthony and Sebastian [1]	658.2107061	4×10^{-10}
Grotch and Kashuba, CODATA 2002 [36, 76]	658.2107044	-2×10^{-9}

Table 3.3: Comparison of different g factors in calculating $\frac{g_e}{g_p}\frac{m_p}{m_e}$

3.3 Magnetic Field Measurement

As described in Section 3.1.2, the characteristics of our magnetic potentials are of great importance to this experiment. The trap field field model developed by our group (see Appendix G of Dale Fried's PhD thesis [30]) based on the Biot-Savart law and the geometry of our coils allows us to predict a certain trap bottom magnetic field and trap shape, with an estimated uncertainty of less than 20% in the trap shape. It is clearly also important to measure the actual value of the trap field. In doing so, we discovered that our trap model (and thus probably recorded coil geometry) is inaccurate.

This section details the different methods of measuring both the trap bottom and average trap field. These allow us to be certain that the trap field is close to 810 G for the 2S field-independent point transition measurement. These methods may also be useful in future experiments, such as $2S-nS$ transition measurements. Measuring and varying the magnetic field will help understand the impact of the trapping field on systematics and experimental error.

3.3.1 Trap bottom magnetic field: 1S hyperfine resonance

We developed a method of testing our trap field model by measuring the trap field precisely at low magnetic fields. This method uses the rf 1S $|d\rangle$ to $|c\rangle$ hyperfine transition.

At low fields, we can use the 1S hyperfine spectrum (see Fig. 3-6) to measure the smallest magnetic field in our trap, at the trap bottom. This is done by driving the $|d\rangle \rightarrow |c\rangle$ transition. At low fields, the $|c\rangle$ state is untrapped. At intermediate fields of 50 G or higher, the $|c\rangle$ is weakly trapped, as can be seen in Fig. 3-6. This feature ultimately limits the range of magnetic fields over which the 1S hyperfine resonance can be used to measure the magnetic field of our trap.

The experimental technique consists in trapping a cold, dense sample in the magnetic trap, and then applying a linearly increasing rf ramp through the rf coils while observing the bolometer signal (see Fig. 3-7). At a frequency corresponding to a magnetic field below the trap bottom, no atoms will be resonant, and no signal will be seen on the bolometer. As the frequency is ramped up, it becomes resonant with the $|d\rangle \rightarrow |c\rangle$ transition and some of the $|d\rangle$ state atoms are transfered to the $|c\rangle$ state. If the magnetic field is small enough, and hence the transition frequency similar enough, some of these $|c\rangle$ state atoms may in turn be transferred to the anti-trapped $|b\rangle$ state. It is worth noting that this situation is different from the usual Landau-Zener treatment [63, 120, 109] used to describe rf evaporation of atoms from the top of magnetic traps. The Landau-Zener treatment depends on a finite slope of the magnetic trap at the resonance point, and at the trap bottom this slope is zero.

The $|b\rangle$ state atoms are high-field seeking, and hence follow the field gradient of the quadrupole magnet to the cell walls. But the $|c\rangle$ state atoms are untrapped at low fields: they expand and fall in the cell, enough falling on the bolometer that we can measure a signal. This signal is strongest exactly when the rf frequency is at the field bottom (effectively opening a hole in the trap). Thus we can measure the

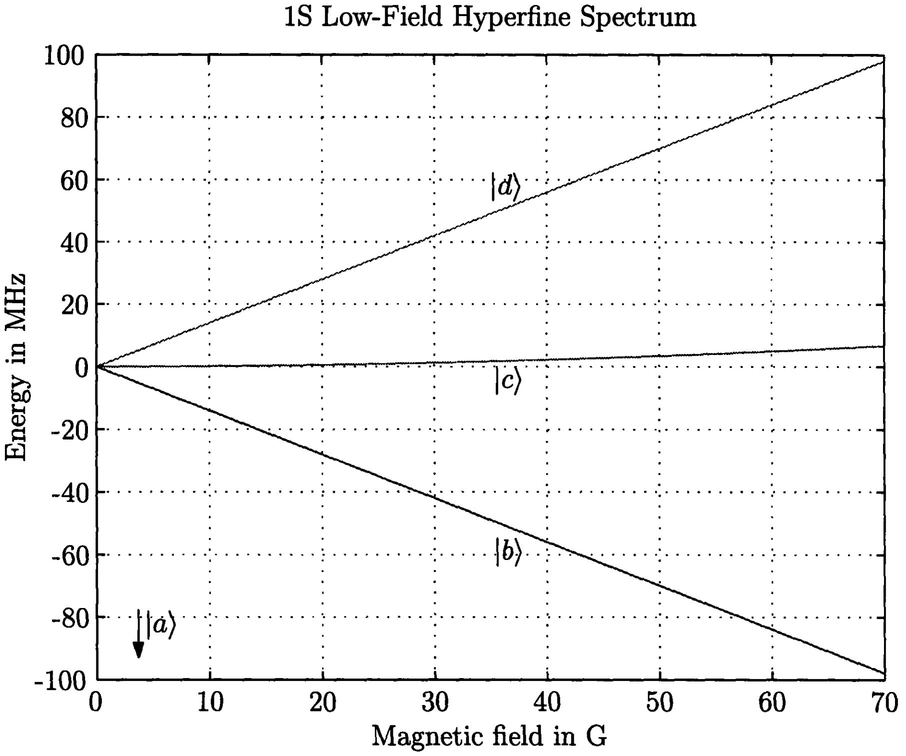

Figure 3-6: $F = 1$ low-field hyperfine structure of the hydrogen 1S state. At low fields (below 20 G), the $F = 1$ manifold is approximately linear, with slopes of 1 Bohr magneton μ_B per G, or 1.4 MHz/G between the $|d\rangle$ and $|c\rangle$, and the $|c\rangle$ and $|b\rangle$ states. At higher fields, the difference between the $|d\rangle \rightarrow |c\rangle$ and $|c\rangle \rightarrow |b\rangle$ transition frequencies becomes considerable. The $|c\rangle$ state is untrapped at very low fields. At intermediate fields, of 50 G or higher, the $|c\rangle$ state is weakly trapped.

frequency, and the magnetic field, of the trap bottom.

To use this technique effectively, the rf power must be large enough remove many atoms rapidly, but not so large that there is significant power in the second harmonic of the frequency (which would be resonant with the trapped atoms before the fundamental, and hence give a measurement of the trap bottom transition frequency exactly half of the real one.)

Error estimation and method limitations

The accuracy of this technique is limited by the time-of-flight of the $|c\rangle$ atoms This results in a magnetic trap bottom measurement error of half a gauss, which is systematic. Hence this technique always indicates a trap bottom half a gauss larger than the real trap bottom. This effect is corrected for in the values of Fig. 3-7. However, half a gauss is a good figure of merit for the accuracy provided by this method of measuring the magnetic field of our trap. It is by far the most accurate magnetic field measurement technique we possess.

As mentioned above, this technique does not work for trap bottom fields higher

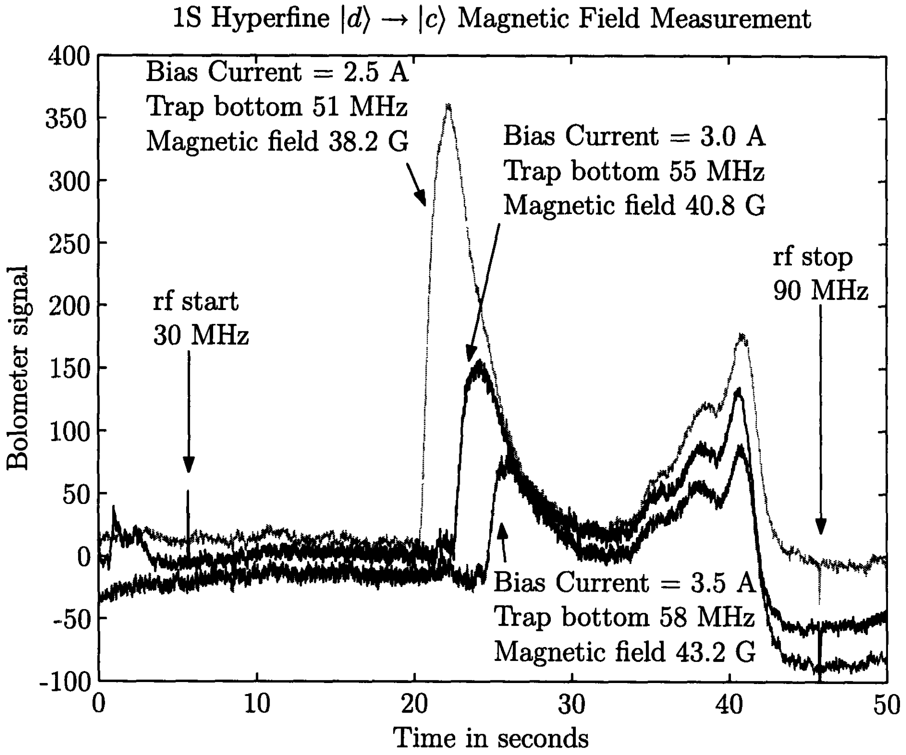

Figure 3-7: 1S Hyperfine magnetic trap bottom measurement.

The magnetic fields are held constant, and the atoms are released from the trap by driving the $|d\rangle \rightarrow |c\rangle$ transition The rf frequency is swept linearly from 30 MHz to 90 MHz, as indicated by the start and stop arrows. Only the transverse rf coil is used in this measurement. The bolometer detects the atoms removed from the trap when the rf is resonant with the trapped atoms. The first and largest atom signal happens when the rf is resonant with $|d\rangle \rightarrow |c\rangle$ transition at the trap bottom. By comparing the time of the atom signal rise with the value of the rf sweep, we can determine the trap bottom resonant frequency and hence the trap bottom magnetic field.

The rf coils also interact with the bolometer electronics. To compensate for this effect, a bolometer trace with no atoms in the trap is taken, and subtracted from the traces with atoms in the trap. The result of this subtraction are the curves shown here.

The dip close to 85 MHz in all three traces can be explained by a strong resonance of the cell (and bolometer) with the transverse rf coil at 83 MHz. This resonance is so large, it is hard to subtract correctly. This resonance and its impact on our 2S experiment experiment is described in more detail in Section 3.5.4. The bolometer curve subtraction in that case is possible because of the lower rf power used.

than approximately 50 G, due to weak trapping of the $|c\rangle$ atoms.

In summary, the 1S hyperfine resonance method for measuring the trap bottom magnetic field works extremely well for trap bottoms below 50 G. The estimated accuracy of the measurement is half a gauss.

Comparison to the trap field model

We used this technique to compare our magnetic trap model to the actual magnetic field, and measure gauss/ampere slope of each individual magnet.

The main conclusion was that our magnetic field model calculation is inaccurate for many magnets, in particular overestimating the lower pinch magnet field contribution to the trap bottom by as much as 30 %. The model can be expected to get worse as fields get larger and errors multiplied. To ensure that we could set the trap field to 810 G, we required another magnetic field measurement technique. For this we measured higher magnetic fields using the $2S_{1/2} \rightarrow 3P_{3/2}$ transition, as described in the following section.

3.3.2 Average magnetic field: $2S_{1/2} \rightarrow 3P_{3/2}$ transition

The $2S_{1/2} \rightarrow 3P_{3/2}$ optical transitions have first-order Zeeman shifts and can be used to measure magnetic fields above 50 G. This technique measures the average magnetic field in the trap. Since the trap bottom magnetic field $B_{\rm min}$ is of interest for the $2S$ $|d\rangle$ to $|c\rangle$ transition, we need to understand the connection between the average field $\langle B\rangle$ and the trap bottom field $B_{\rm min}$ through the sample temperature. The ultimate accuracy of this technique in measuring $B_{\rm min}$ is 5 G, if the temperature of the sample is known.

The $3P_{3/2}$ spectrum, allowed transitions and linewidth

For the $3P_{3/2}$ state above 10 G, we can use the high field Zeeman limit (see Fig. 3-8). The good quantum numbers at high fields are $m_J = [-3/2, -1/2, 1/2, 3/2]$ and $m_I = [-1/2, 1/2]$. At high fields, the splitting between states of the same m_J and different m_I is negligible.

The highest 3 m_J states in Fig. 3-8 have allowed transitions from the 2S state $|d\rangle$, since angular momentum conservation rules dictate that $\Delta m = +1, 0$ or -1. The natural lifetime of the $3P$ state is 0.54×10^{-8} seconds [6], hence the natural linewidth of the $2S \rightarrow 3P$ transition is approximately 20 MHz. At very low magnetic fields, the three allowed transitions overlap, making a measurement difficult. However, at intermediate fields (upwards of 50 G) the three allowed transitions are distinguishable, and can provide an absolute magnetic field measurement.

Due to the differences in transition probabilities due to polarization and relative ingoing and return red beam intensities, to excite the different m_J states sufficiently often means power-broadening at least one of them. This effect can be mitigated by using a polarizer. However for our magnetic field measurements, spurious power-broadening is not important as long as the broadening is not too large (eg. washing

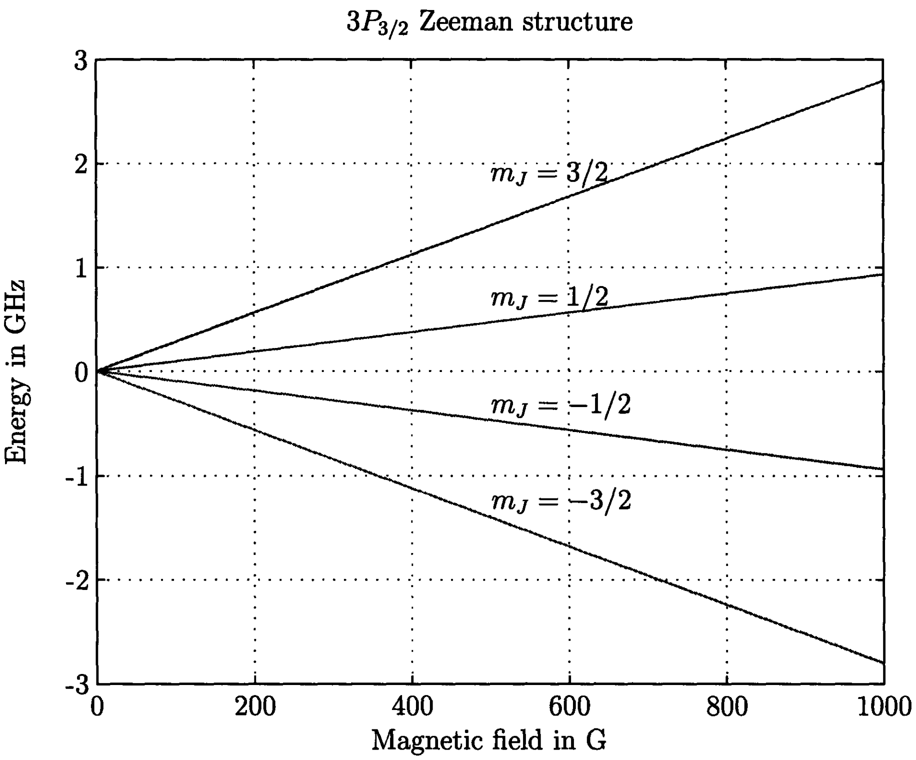

Figure 3-8: Zeeman structure of the hydrogen $3P_{3/2}$ state. The three upper m_J have allowed transitions from the 2S $m_J = 1/2$ state. Each of the four m_J levels shown contains both a nuclear spin m_I up and down level as well. The splitting between these is negligible.

out the neighboring transitions).

At trap fields above 50 G, the ratio of the radial field B_ρ (quadrupole magnet field) to the axial field B_z (all other magnet coils) is small. This causes the hydrogen's electron to be spin-polarized mainly in the z direction. Since the red laser beam is aligned along the z-axis, the light is polarized in the plane perpendicular to the direction of propagation: the polarization is in the radial direction. This geometry causes the $\Delta m = \pm 1$ transitions to be favored over the $\Delta m = 0$ one, which would require the polarization of the light and the electron spin to be along the same axis. Consequently, of the three possible transitions, transitions to the $m_J = 3/2$ and $m_J = -1/2$ states are favored

The 656 nm diode laser system

To drive the $2S_{1/2}$ to $3P_{3/2}$ transition, a 656 nm (red) diode laser system was built in our group [108] for purposes of investigating red absorption as an alternative detection technique to quenching of the 2S atoms. The laser system consists of two diode lasers, one locked to an iodine line through saturated absorption spectroscopy of an iodine cell, the other offset locked to the the first one at a computer-controlled frequency. To do the magnetic field measurement, we fix the UV 243 nm laser at the peak of the 1S-2S resonance, and scan the red 656 nm laser. The signal is apparent as a depletion of detected 2S atoms as a function of red frequency. We adjust the red laser alignment and power so as to be co-aligned with the UV laser, and not power-broaden the 2S-3P transition.

$2S - 3P$ magnetic field measurements

The $2S - 3P$ magnetic field measurement is possible from intermediate (greater than 50 G) to high fields. Measurements at intermediate fields (50 to 150 G) can be done in one step, and are referred to as an *absolute* field measurement. At high fields (above 150 G), measurements must be done in two steps, and are referred to as *relative.*

Absolute field measurement: Correction for sample temperature

The absolute field measurement uses the difference between the transition from the 2S $|d\rangle$ state to the 3P $m_J = -1/2$ and the transition from the 2S $|d\rangle$ state to the 3P $m_J = 3/2$ to measure the magnetic field. In our experiment, these two transitions are the strongest, as explained above. At fields below 50 G, it is difficult to resolve the two lines clearly. At fields higher than 150 G, the splitting between the two $\Delta m = \pm 1$ states becomes prohibitively large to scan without losing the offset lock (larger than 550 MHz). Between 50 and 150 G, it is possible to clearly resolve both lines in a single red scan, and make an absolute magnetic field measurement from the difference between the $m_J = 3/2$ and $m_J = -1/2$ transition frequencies.

It should be noted that it is possible to set the offset lock to frequencies as large as 1.4 GHz, but the scan range around these set lock points is best kept below 300-500 MHz, or the offset lock may be lost.

Relative field measurements

To measure larger magnetic fields, we scan only the $m_J = 3/2$ transition, and refer the transition frequency to a lower absolute magnetic field measurement. We compare the high magnetic field $m_J = 3/2$ to the lower field $m_J = 3/2$ transition frequencies.

The starting 2S $|d\rangle$ state and the final 3P $m_J = 3/2$ state are both stretched states, with slopes of 1 and 2 Bohr magnetons μ_B per G respectively. Thus the transition energy between the two states changes by 1 Bohr magneton per G, or 1.4 MHz/G. To measure a magnetic field of 810 G, the red laser's offset lock needs to be set at frequencies ranging from 260 MHz (low field lock point) to 1.4 GHz (high field lock point), without losing the iodine lock or skipping to another iodine line. At each field, the red laser is scanned around the lock point over a 500 MHz range (low field) or 300 MHz range (high field). The locking electronics must work smoothly at very high frequencies ($>$ 1 GHz).

Average field measurement

The magnetic field measured using the $2S - 3P$ transition is the average magnetic field of the trap (as opposed to the trap bottom magnetic field measured by the

$1S\,|d\rangle \rightarrow |c\rangle$ transition, as described in Section 3.3.1). For the purposes of the 2S hyperfine spectroscopy experiment, we are mainly interested in knowing the magnetic field of the trap bottom, and the following describes how to go from the average to the minimum field.

If we approximate our magnetic potential for the $|d\rangle$-state atoms as harmonic (see Section 3.4.5), the magnetic field is

$$B(\mathbf{r}) = B_{\min} + \frac{2\,U(\mathbf{r})}{(g_e - g_I)\mu_B} = B_{\min} + \frac{m}{(g_e - g_I)\mu_B}\left(\omega_\rho^2(x^2+y^2) + \omega_z^2 z^2\right) \tag{3.27}$$

where $B_{\min}$ is the trap bottom field, and ω_ρ and ω_z are the radial and axial trap frequencies respectively. The coefficient of U in Eq. 3.27 is approximately μ_B^{-1}. Using the equipartition theorem, we find the expectation value of the magnetic field in the trap is

$$\langle B\rangle = B_{\min} + \frac{3k_BT}{2\mu_B}. \tag{3.28}$$

Details of the absolute $2S - 3P$ measurement

When we are measuring an absolute magnetic field value using both the $3P$ $m_J = -1/2$ and $m_J = 3/2$ transitions, we find

$$\begin{aligned}
\nu_- = {} & \nu_{\text{ol}} + \kappa_-\langle B\rangle & = \nu_{\text{ol}} + \kappa_-\left(B_{\min} + \frac{3k_BT}{2\mu_B}\right) \\
\nu_+ = {} & \nu_{\text{ol}} + \kappa_+\langle B\rangle & = \nu_{\text{ol}} + \kappa_+\left(B_{\min} + \frac{3k_BT}{2\mu_B}\right) \\
\nu_+ - \nu_- = {} & (\kappa_+ - \kappa_-)\langle B\rangle & = (\kappa_+ - \kappa_-)\left(B_{\min} + \frac{3k_BT}{2\mu_B}\right)
\end{aligned} \tag{3.29}$$

where ν_{ol} is the offset lock frequency at zero magnetic field, κ_+ and κ_- are the slopes of the $m_J = 3/2$ and $m_J = -1/2$ lines in Fig. 3-8 (using the $m_I = +1/2$ lines in each doublet, since the nuclear spin orientation should not be affected by the transition). The coefficients for these two transitions are $\kappa_+ = 1.400$ and $\kappa_- = -2.331$ MHz/G.

An example of absolute magnetic field measurement is shown in Fig. 3-9.

Details of the relative $2S - 3P$ measurement

At higher magnetic fields, we measure only $\nu_+ = \nu_{+\text{hi}}$ and reference the lower magnetic field $\nu_+ = \nu_{+\text{lo}}$ frequency:

$$\nu_{+\text{hi}} - \nu_{+\text{lo}} = \kappa_+\left(\langle B_{\text{hi}}\rangle - \langle B_{\text{lo}}\rangle\right) = \kappa_+\left(B_{\min,\text{hi}} - B_{\min,\text{lo}} + \frac{3k_B(T_{\text{hi}} - T_{\text{lo}})}{2\mu_B}\right). \tag{3.30}$$

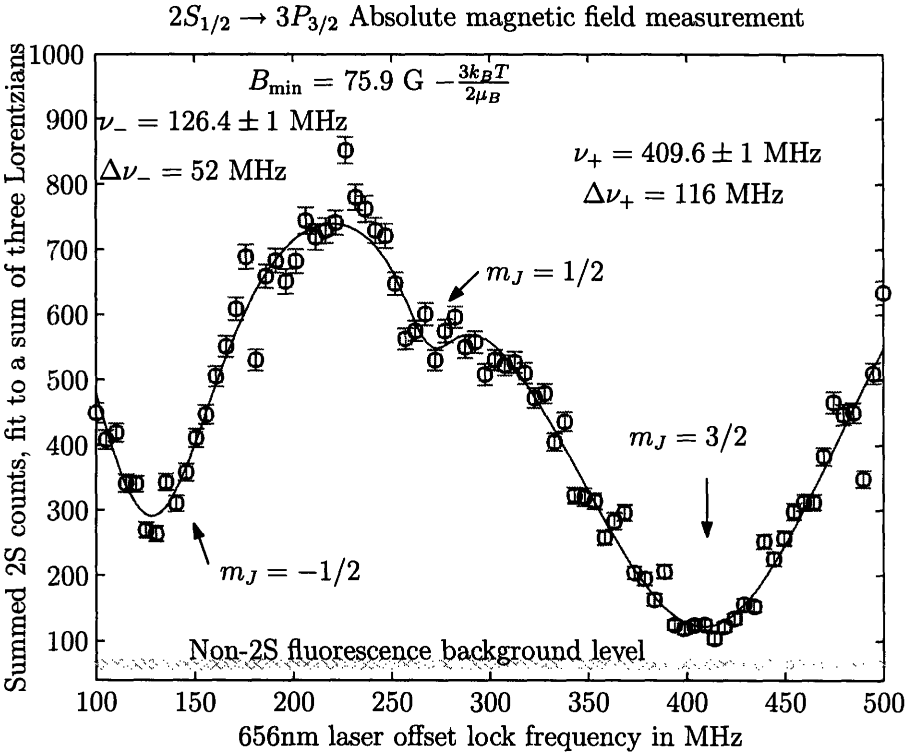

Figure 3-9: Example of a $2S_{1/2} - 3P_{3/2}$ absolute magnetic field measurement.
The center frequencies and linewidths are results of a Levenberg-Marquardt non-linear regression fit to a sum of three Lorentzians (the third, $m_J = +1/2$ component is fit so as not to induce a systematic shift in either the $m_J = 3/2$ or $m_J = -1/2$ components). The widths are half-width at half-maximum of the Lorentzian. The errors suggested by the fit for the center frequencies are underestimates: repeating the measurement for several traps gives a more realistic standard deviation of 5 MHz in each center frequency, which corresponds to 2 G standard deviation in the magnetic field measurement.
The estimated Zeeman broadening due to the thermal spread of the atoms should be close to 4 G, or 6 MHz in the upper $m_J = 3/2$ state and 9 MHz in the lower $m_J = -1/2$ state. Since the width of the upper state is double that of the lower, thermal Zeeman broadening is not responsible for the much-larger-than-natural linewidth. In this case, the lineshapes are no longer exact Lorenztians, but for our purposes the Lorentzian fit is good enough.
The large linewidth is most likely due to power broadening. For both lines to be clearly visible, we use a higher red power than necessary for just the $m_J = 3/2$ line. Typical red laser beam powers are on the order of 60 μW. We typically only leave the red beam in for 1 millisecond (the timescale necessary for the 2S atoms in a 1 kHz radial trap to cross the beam).

Solving for $B_{\mathrm{min,hi}}$, and using our previous relations for $B_{\mathrm{min,lo}}$ (Eq. 3.29), we obtain

$$B_{\mathrm{min,hi}} = \frac{\nu_{+\mathrm{hi}} - \nu_{+\mathrm{lo}}}{\kappa_+} + \frac{\nu_{+\mathrm{lo}} - \nu_{-\mathrm{lo}}}{\kappa_+ - \kappa_-} - \frac{3k_B T_{\mathrm{hi}}}{2\mu_B} \tag{3.31}$$

which is dependent only on the $2S - 3P$ transition frequencies and the sample temperature at high magnetic field.

An example of a high magnetic field measurement is shown in Fig. 3-10.

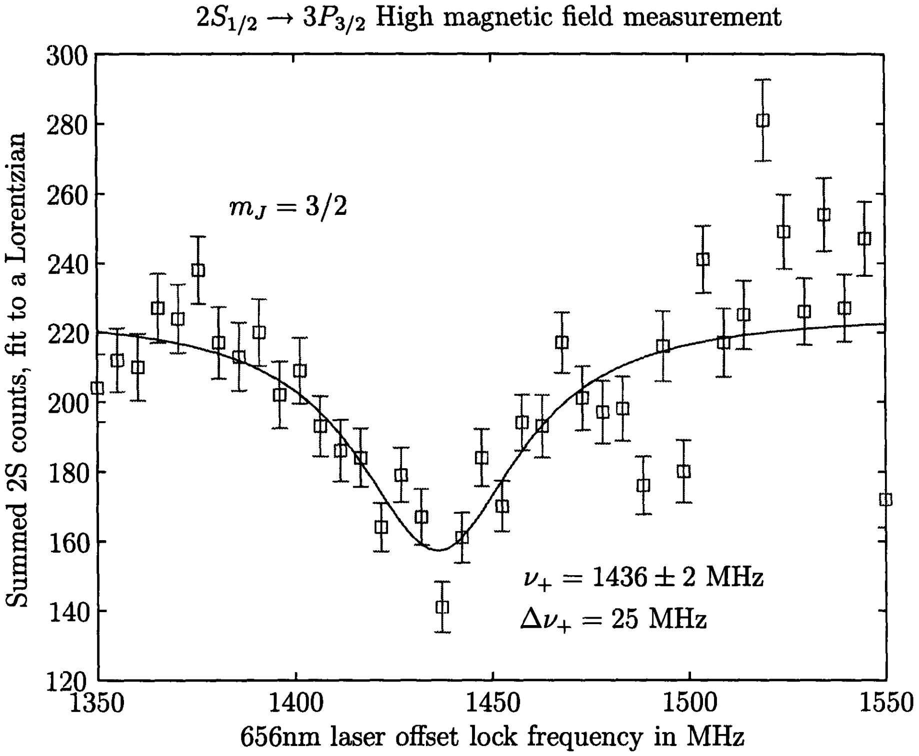

Figure 3-10: An example of a $2S_{1/2}$–$3P_{3/2}$ high magnetic field (relative) measurement. The center frequency and linewidth are results of a Levenberg-Marquardt non-linear regression fit to a Lorentzian curve. The width is the half-width at half-maximum of the Lorentzian. By using this measurement in conjunction with Eq. 3.31 and the lower absolute magnetic field measurement shown in Fig. 3-9 we can find the magnetic field $B_{\mathrm{min}} = 809$ G - $3k_BT/2\mu_B$.
Care was taken during these measurements to ensure that the 656 nm laser's iodine lock point had not changed between high field and low field traps. As for the absolute field measurement, the fitted error in the center frequency is too low - repeated measurements at the same magnetic field give a standard deviation of 7 MHz, corresponding to 5 G standard deviation in the magnetic field. The larger frequency standard deviation at high fields is due to the lower signal-to-noise ratio.

Assessment of the $2S - 3P$ field measurement technique

The $2S_{1/2} - 3P_{3/2}$ magnetic field measurement technique can be used over a wide range of magnetic fields (larger than 50 G), with an accuracy of 5 G. However, since the measurement is of the average field, and not the trap bottom field, it is also important to know the sample temperature if the latter quantity is important.

3.3.3 Magnetic field dependence of 1S-2S transition

The frequency of the 1S $|d\rangle$ to 2S $|d\rangle$ transition depends on the magnetic field through the bound state corrections to the electron and proton Landé g factors, which are dependent on the energy level n (see Section 3.2.4).

The main contribution is the first order relativistic correction to g_e (see Eq. 3.19):

$$\frac{\epsilon}{m_e}\frac{4J(J+1)+1}{4J(J+1)} = -\frac{2}{3}\left(\frac{\alpha}{n}\right)^2 . \tag{3.32}$$

Both g_e and g_p can be expressed to first order in the relativistic correction as

$$g = g\left(1 - \frac{1}{3}\left(\frac{\alpha}{n}\right)^2\right) . \tag{3.33}$$

We can express the 1S-2S $|d\rangle$ state to $|d\rangle$ state frequency shift as a function of magnetic field as

$$\nu_{1S-2S}(B) - \nu_{1S-2S}(0) = \frac{\alpha^2}{4}(g_e - g_I)\frac{\mu_B B}{2h} \simeq 18.63\frac{\text{Hz}}{\text{G}} , \tag{3.34}$$

where the free (unbound) values of g_e and $g_I = g_p(m_e/m_p)$ are used.

At a magnetic field of 810 G, the shift at 121 nm is 15 kHz, which translates to 7.5 kHz at 243 nm (the frequency of our doubled laser) and 3.8 kHz at 486 nm (the frequency of the pre-doubled laser, which we control). Although this shift is clearly visible, and must be taken into account when doing spectroscopy at high fields, our 486 nm laser's linewidth is on the order of 1 kHz and it can drift by as much as 1 or 2 kHz between traps, making this magnetic field-dependent frequency shift unreliable as a magnetic field indicator.

A future 243 nm laser is planned with a linewidth of 100Hz and better stability. With such a narrow linewidth, changes in magnetic field of roughly 20 G (as opposed to 200 G) could be detected. However, this method will never be competitive with either the 1S hyperfine resonance (see Section 3.3.1) or the 2S-3P transition (see Section 3.3.2) as a magnetic field measurement technique.

3.4 Temperature Measurement

It is important for us to measure the temperature of the trapped sample at low as well as high magnetic fields. For the 2S hyperfine spectroscopy experiment, the temperature is a crucial quantity. It is necessary to interpolate between the measured average magnetic field and the trap bottom magnetic field as explained in Section 3.3.2. It is also important in understanding our expected signal strength as described in Section 3.5. The lower the temperature of the 810 G sample, the larger the expected signal, and the smaller the broadening. Thus the temperature is an important quantity to optimize during the trapping-cooling-field raising sequence.

We measure the temperature of the hydrogen sample by analyzing the two photon $1S-2S$ (243 nm) spectrum. This spectrum contains both Doppler-sensitive and Doppler-free components [54]. The Doppler sensitive spectrum provides a direct measurement of the sample temperature, since the linewidth is directly related to the momentum distribution of the atoms and the geometry of the trap and 243 nm laser beam. However, this spectrum is much broader, and hence smaller in amplitude, than the Doppler-free spectrum, and not measurable for us at high magnetic fields, where the $1S-2S$ signal is weaker.

3.4.1 The doppler-free double-exponential lineshape

We can use the Doppler-free spectrum to obtain an approximate temperature measurement. The Doppler-free spectrum (number of excitations per second of the sample) is given by the following expression (neglecting the $1S-2S$ cold collision shift) [7, 54]

$$S(\nu)=\frac{\pi^2}{16}\frac{\Omega_0^2 w_0^4}{\bar{v}}\int_{-\infty}^{\infty}\mathrm{d}z\frac{n(z)}{w(z)}\exp\left(-\frac{|\nu-\nu_0|4\pi w(z)}{\bar{v}}\right), \tag{3.35}$$

where Ω_0 is the the $1S-2S$ transition Rabi frequency at the center of the counter-propagating laser beams, w_0 and $w(z)$ denote the laser beam waist at the laser focus and along the z-axis. $\bar{v}=\sqrt{2k_BT/m}$ is the most probable speed of the atoms, $n(z)$ is the sample density, ν is the laser frequency and $\nu_0=E_{1S-2S}/2h$ is the exact resonance frequency at 243nm.

This lineshape can be simplified in the limit where the vertical z extent of the atom cloud is much smaller than the divergence or Rayleigh length of the laser beam $z_0=\pi w_0^2/\lambda$ (λ is the 243 nm laser wavelength). In this limit, the laser beam waist can be assumed to be constant $w(z)=w_0\sqrt{1+z^2/z_0^2}\approx w_0$ over the extent of the atom cloud, and the integral in Eq. 3.35 simplifies to

$$S(\nu)=\frac{\Omega_0^2\pi^2 w_0^3}{16\bar{v}}N\exp\left(-\frac{|\nu-\nu_0|4\pi w_0}{\bar{v}}\right). \tag{3.36}$$

The spectrum has the form of a double-exponential with a 1/e half width given by

$$\Delta\nu=\frac{1}{4\pi w_0}\sqrt{\frac{2k_BT}{m}}\approx 10^3\frac{\sqrt{T}}{w_0}\ \mathrm{Hz\,cm\,K^{-1/2}}. \tag{3.37}$$

Thus the measurement of the $1S-2S$ double-exponential linewidth is an absolute measurement of the temperature, as long as the beam waist at the location of the atomic cloud is known. For the same laser beam configuration, we can use this method as a relative temperature measurement technique, even if the beam waist is not exactly known, as long as the different atom samples are at roughly the same z-axis location (whether at the focus or not).

3.4.2 Systematics of the double-exponential linewidth

If we are attempting to measure the relative temperatures of the atoms trapped in different trap configurations, it is important to understand the systematics introduced by changing the vertical z extent of the sample, and the vertical position of the trap center.

Long sample systematics

If the sample is long, on the order of the divergence length of the laser beam, the spectrum is still a double-exponential, but an effective beam waist $w_{\text{eff}} > w_0$ should be used in Eq. 3.36. Thus the measured width $\Delta\nu$ will be smaller than that predicted by Eq. 3.37, which can be misleading when inferring a temperature. Two separate phenomena can lead to a long sample: a large temperature, or a long shallow trap.

The thermal half length of the sample (if we assume a harmonic trap configuration along the z-axis) is $\bar{z} = 1/\omega_z\sqrt{k_BT/m}$, where ω_z is the axial, or vertical, trap frequency. For a beam waist at the laser focus of 40 μm, the corresponding z_0 is 2 cm. The approximation used to obtain Eq. 3.36 can be written $\bar{z} \ll z_0$. A typical trap sample temperature at the end of our magnetic evaporation is 200 μK. This corresponds to a thermal half length $\bar{z}$ of 1.5 cm, on the same order as z_0. of the sample. Thus for such samples and warmer ones, the temperature estimates given by the double-exponential linewidth using Eq. 3.37 have a systematic error.

We have studied this effect numerically. As can be seen in Fig. 3-11, the linewidth as a function of temperature deviates significantly from the simple constant beam waist model even at low temperatures, especially for small axial trap frequencies ω_z.

Trap-laser vertical offset systematics

The vertical location of the trap center also plays a role. If $\bar{z} \ll z_0$, but the trap center and the laser beam focus are not at the same vertical position, the beam waist in Eq. 3.37 should be replaced with a (larger) beam waist at the trap center, closer to $w(z) = w_0\sqrt{1 + z^2/z_0^2}$ than to w_0. We have studied this effect numerically.

A vertical displacement of a few centimeters will again cause the temperature calculated using 3.37 to be smaller than the actual sample temperature, as can be seen from Fig. 3-12. The lower the trap frequency, the less sensitive the double-exponential linewidth is to a vertical offset of the trap and laser. However, a vertical offset between the laser beam and the trap center will also decrease the total 2S excitation rate, and can thus also be seen as a decrease in overall signal.

Conclusion of double-exponential systematics study

Hence the double-exponential linewidth method of temperature measurement should be done with great care, understanding that when seeking a lower temperature sample, it is possible to be misled. One may simply be moving the trap center out of the laser focus or lowering the axial trap frequency, which both have the result of reducing the linewidth without lowering the temperature.

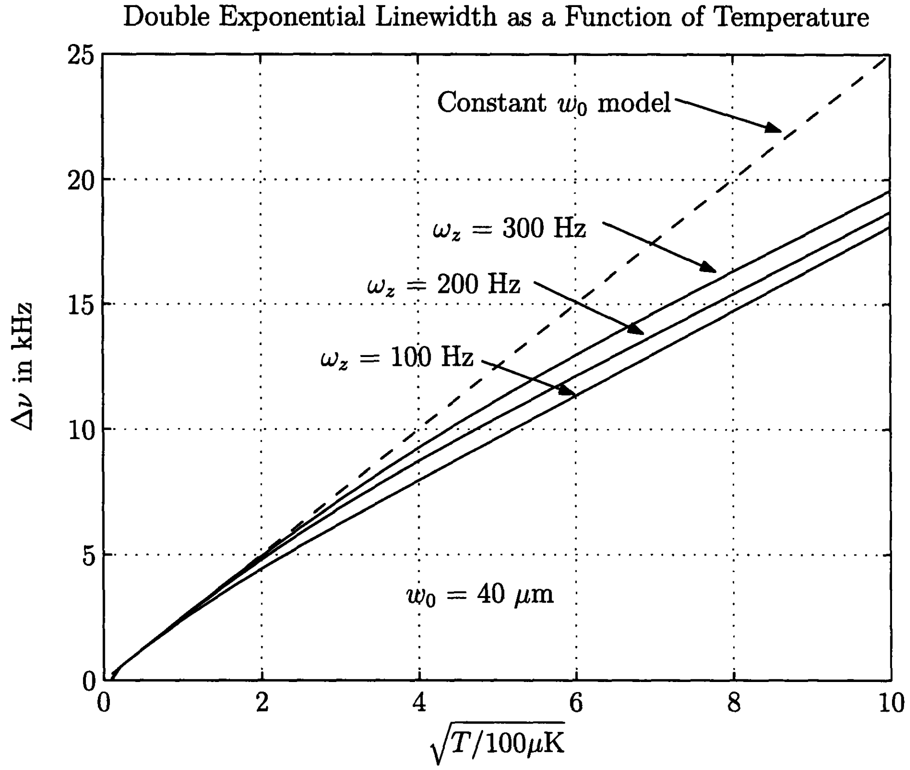

Figure 3-11: Double-exponential linewidth as a function of temperature and axial trap frequency. The linewidths (half width at 1/e point) in this figure are calculated numerically from Eq. 3.36. The result of the constant beam waist approximation, Eq. 3.37, is shown as a dashed line. At temperatures above 400 μK, one must know the axial trap frequency ω_z in order to infer the temperature from the measured linewidth. In our magnetic trap at the end of the magnetic evaporation, our axial trap frequency is modelled to be 90 Hz.

3.4.3 High-magnetic-field temperature measurement

At high magnetic fields, neither our trap frequencies nor our trap center position are known. However, some estimates can be made using several assumptions:

- if we can measure a $1S - 2S$ signal, the trap must be close to the laser focus
- no significant atom loss occurs during the magnetic field ramp-up
- if the magnetic field ramp-up is smooth and slow enough, the low-field to high-field process is adiabatic.

The second assumption is made because the high-field ramp raises the magnetic trap barriers tremendously, shutting off the evaporation process, and confining atoms up to 300 mK (over 1000 times the initial temperature) in energy. This assumption could be tested by doing a ramp-up then ramp-down and detecting the number of atoms remaining (which we did not do).

To be able to make the third assumption, great care was taken to make the magnetic field ramp smooth and reproducible, see Appendix C.

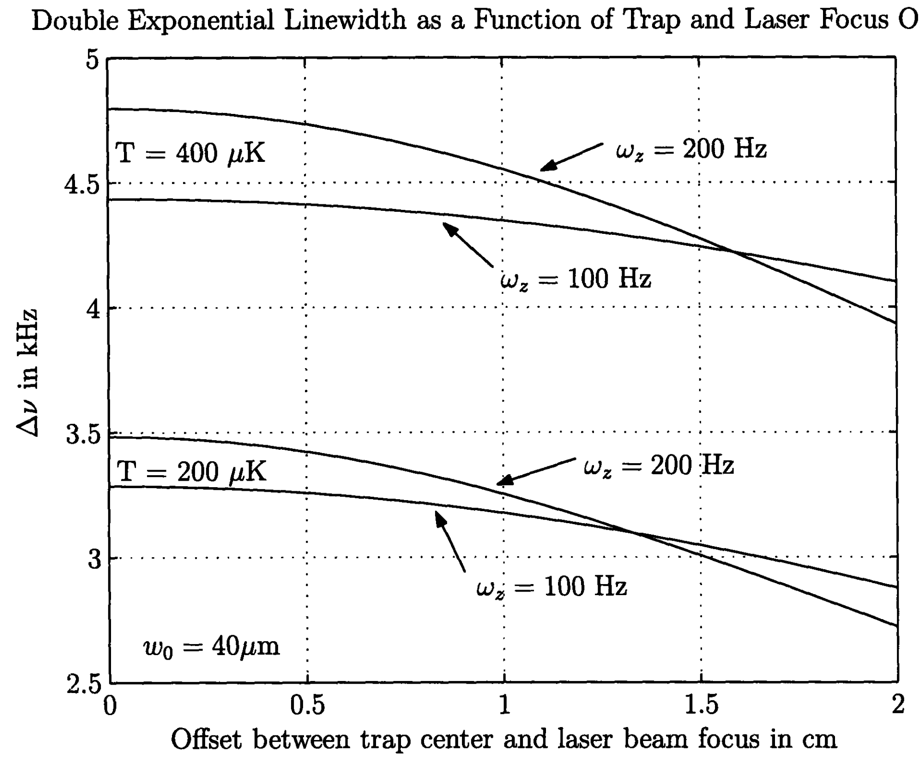

Figure 3-12: Double-exponential linewidth as a function of trap center and laser focus vertical offset. The linewidths in this figure are calculated using Eq. 3.36 as a function of laser beam focus and trap center vertical offset.

3.4.4 Adiabatically changing a harmonic trap

We make the assumption that our low magnetic field to high magnetic field ramp is adiabatic, and takes a sample of N atoms at temperature T_1 in a harmonic trap with radial and axial frequencies $\omega_{\rho 1}$ and ω_{z1} to another harmonic trap with radial and axial frequencies $\omega_{\rho 2}$ and ω_{z2} and sample temperature T_2 with no change in phase space density. This treatment follows the description of adiabatic compression described in [53].

In general, one can express a power law potential as

$$U(r) = Cr^{d/\delta} \tag{3.38}$$

where d is the dimensionality of the system. For a 3-dimensional harmonic trap, $d/\delta = 2$ and $\delta = 3/2$. The volume V scales as r^d, so the potential U scales as $V^{1/\delta}$. Since the expectation value $\langle U \rangle$ is proportional to $k_B T$, we find that the thermal volume of the system scales as

$$V \propto T^{\delta}. \tag{3.39}$$

Changing the system adiabatically means that the phase space remains constant. The phase space density is $n\lambda_{dB}^3$ where n is the particle density and $\lambda_{dB} = \sqrt{2\pi\hbar^2/mk_BT}$ is the thermal de Broglie wavelength. The adiabaticity condition thus means that

$$n_1/{T_1}^{3/2} = n_2/{T_2}^{3/2}. \tag{3.40}$$

How does the atom density n change with the trap frequencies and temperature in a harmonic potential U?

$$U(\mathbf{r}) = \frac{m}{2}\left((\omega_x x)^2 + (\omega_y y)^2 + (\omega_z z)^2\right) \tag{3.41}$$

By the equipartition theorem [84], each quadratic term in U should have the expectation value $k_B T/2$. Hence the thermal volume can be expressed

$$V = \sqrt{\langle x^2\rangle\langle y^2\rangle\langle z^2\rangle} = \left(\frac{k_b T}{m}\right)^{3/2} \frac{1}{\omega_x\omega_y\omega_z} = \frac{N}{n} \tag{3.42}$$

Our trap is axially symmetric, $\omega_x = \omega_y = \omega_\rho$. The adiabaticity condition of Eq. 3.40 reduces to

$$\frac{\omega_{\rho 1}^2\omega_{z1}}{T_1^3} = \frac{\omega_{\rho 2}^2\omega_{z2}}{T_2^3}. \tag{3.43}$$

When going from low to high magnetic fields, it is desirable to maintain the same radial confinement, since this determines the atom density in the narrow vertical laser beam. If ω_ρ remains unchanged, the adiabatic temperature change depends only on the difference between the low and high field axial trap confinement.

3.4.5 Harmonic frequencies in a Ioffe-Pritchard trap

We have good estimates of the trap parameters and temperature in our low magnetic field trap, but only have a robust estimate of ω_ρ in our high magnetic field trap. Our magnetic trap is a Ioffe-Pritchard [86, 66] configuration, which is the combination of a linear radial field gradient, and an axial field that can approximated as quadratic near the trap bottom. These two magnetic field components are perpendicular, and hence add in quadrature:

$$U_{IP}(\rho, z) = \sqrt{(\alpha\rho)^2 + (\beta z^2 + U_0)^2} - U_0 \tag{3.44}$$

where α is the linear radial potential coefficient, with units of (energy/length), β is the axial potential curvature with units of (energy/length^2) and U_0 is the bias of the potential (corresponding to $B_{\min}$ in Eq. 3.27), and the notation is the same as used in [66].

We can expand this expression in powers of $\alpha\rho/(\beta z^2 + U_0)$ as long as we understand this is only valid when $\rho \ll U_0/\alpha$. Then

$$\begin{aligned} U_{IP}(\rho, z) &\simeq \beta z^2 + \frac{1}{2}\frac{\alpha^2\rho^2}{\beta z^2 + U_0} - \frac{1}{8}\frac{\alpha^4\rho^4}{(\beta z^2 + U_0)^3} + \mathcal{O}\left(\frac{\alpha^6\rho^6}{U_0^5}\right) \\ &\simeq \beta z^2 + \frac{1}{2}\frac{\alpha^2\rho^2}{U_0}\left(1 - \frac{\beta z^2}{U_0}\right), \end{aligned} \tag{3.45}$$

where the second expansion supposes $|z| \ll \sqrt{U_0/\beta}$. Then we can identify the trap frequencies as

$$\begin{aligned}\omega_z &= \sqrt{2\beta/m} \\ \omega_\rho &= \alpha/\sqrt{mU_0}\end{aligned} \tag{3.46}$$

and rephrase the expansion conditions in terms of the sample temperature:

$$U_{IP} = \frac{m}{2}\left(\rho^2\alpha^2/m\,U_0 + 2z^2\beta/m\right) \simeq \frac{3k_BT}{2} \ll \frac{3}{2}U_0, \tag{3.47}$$

which means that we can use the harmonic approximation to a Ioffe-Pritchard trap when the average potential energy values are less than the bias energy U_0, or $k_BT \ll U_0$. This is clearly the case in the high-field traps where $U_0 \approx 50$ mK (for an 800 G trap bottom). However, in the low-field traps, $U_0 \approx 200\ \mu$K (for a 3 G trap bottom), on the order of the sample temperature. In this case, the harmonic potential approximation is no longer valid, as the expansion parameters are close to unity. However, we can use an intermediate field of 50 G or higher, with $U_0 \approx 3$ mK to do our adiabatic trap analysis.

Since the linear radial magnetic field is created by a quadrupole magnet described by Doyle [22] alone, α is simply proportional to the quadrupole magnet current. According to field calculations [30], $\alpha = 48\,\mu_B\,I$ G/cm $= 3.2\,k_B\,I$ mK/cm, where I is the quadrupole current in amperes.

The axial magnetic field is shaped by 10 separate magnet coils, and is not calculated accurately by our model (see Section 3.3.1 on the 1S hyperfine resonance magnetic field measurement).

Putting all the pieces together, we can measure the average trap field and hence U_0 using the $2S - 3P$ resonance technique described in Section 3.3.2,

$$U_0 = \mu_B B_{\min} = \mu_B\langle B\rangle - 3k_BT/2 \simeq \mu_B\langle B\rangle \tag{3.48}$$

using Eq. 3.28, and the harmonic expansion condition Eq. 3.47.

Understanding α and U_0 means that ω_ρ is well known:

$$\omega_\rho = \frac{\alpha}{\sqrt{mU_0}} \simeq \frac{48\,\mu_B\,I}{\sqrt{m\mu_B\langle B\rangle}} \tag{3.49}$$

and our adiabatic relation Eq. 3.43 becomes

$$\frac{I_1^2\,\omega_{z1}}{T_1^3\langle B_1\rangle} = \frac{I_2^2\,\omega_{z2}}{T_2^3\langle B_2\rangle}, \tag{3.50}$$

which relates T and ω_z to measurable quantities, the quadrupole magnet current I and the average magnetic field $\langle B\rangle$.

If the radial confinement is maintained, the temperature depends only on the axial confinement (as in Eq. 3.43).

Our magnet system does not allow us to have a small axial confinement at high magnetic fields. As described in Section 3.1.2, the high field trap's axial confinement is provided by the large slopes of the lower pinch and bias magnets. Moreover, because our magnetic field model is inaccurate, we cannot know exactly the axial frequency of the high magnetic field trap. We estimate that, at 810 G, ω_z is anywhere from two to twenty times as large as the estimated low field value of 60 Hz. This means that to maintain a low sample temperature, we are forced to open the radial confinement by a factor of roughly two, reducing the density of atoms in the laser beam by a factor of four (and the $1S - 2S$ signal amplitude proportionally, as in Eq. 3.36).

Strategies for lowering the sample temperature at high magnetic fields are discussed in more detail in the next section.

3.4.6 Methods to lower the trap temperature at high magnetic fields

The lower the high magnetic field trap temperature, the narrower the thermal broadening induced in the 2S $|d\rangle$ to $|c\rangle$ transition, and the larger the 2S $|d\rangle$ to $|c\rangle$ resonance signal expected. Thus it is necessary for us to maintain a low sample temperature at high magnetic fields.

If the magnet ramp-up to high fields is adiabatic, starting from a fixed phase-space density, lowering both the radial and axial trap frequencies ω_ρ and ω_z of the high magnetic field trap will lower the temperature, with the radial frequency having the larger (quadratic) impact. However, reducing the radial frequency also reduces the $2S$ signal magnitude by reducing the density of atoms in the laser beam path. The density of the sample n is proportional to $\omega_\rho^2\omega_z$. The density distribution is integrated along the z-axis by the 243 nm laser beam (as in Eq. 3.35). Radially, however, the laser only samples a very small fraction of the sample, since the laser beam waist $w_0 \simeq 40\mu\text{m}$ is smaller than the thermal trap radius $\sqrt{k_BT/m}/\omega_\rho$ for most samples. Thus the $2S$ signal magnitude is expected to decrease quadratically with ω_ρ.

The fact that a reduction in axial trap frequency ω_z also reduces the temperature at high fields has an impact on how we interpret our double-exponential linewidth: we no longer need to worry that our lowering of the axial trap frequency will cause a false lower temperature measurement (as shown in figure 3-11), since lowering the axial trap frequency really does result in a lower sample temperature. Lowering the axial trap frequency does not lower the $2S$ signal magnitude. The problem of mistaking a lower linewidth for a lower temperature when it really is a vertical trap offset (as in figure 3-12) still remains, however. We can try to avoid this pitfall if we also look for signal magnitude changes (since a vertical trap offset from the laser beam focus should reduce the $2S$ signal magnitude as well as the linewidth).

Since our magnetic field model is inaccurate, it is only through a process of trial and error that we can shape the axial trap to obtain the lowest temperature (or double-exponential linewidth) we can measure. This is then understood to be the lowest ω_z possible in a high field trap. The temperature (and linewidth) can be lowered further by reducing the radial trap frequency ω_ρ, however, this will also decrease the $2S$ signal magnitude.

Using these techniques, we are able to obtain temperatures lower than 400 μK at high fields, as determined by measuring the double-exponential linewidth. In these traps, we find $\omega_\rho = 1.5$ kHz from Eq. 3.49, and estimate ω_z to be between 300 and 400 Hz.

3.5 Calculating the 2S $|d\rangle$ to $|c\rangle$ Transition Strength

3.5.1 Introduction

This section calculates the expected transition rate for the 2S $|d\rangle \longrightarrow |c\rangle$ transition in our experiment. The transition rate can be calculated from Fermi's Golden Rule from

$$\gamma_{|d\rangle \rightarrow |c\rangle} = \frac{2\pi}{\hbar} \left|H_{dc}\right|^2 \rho(\nu) \tag{3.51}$$

where H_{dc} is the matrix element for the rf field and $\rho(\nu)$ is the normalized lineshape function. (We have generalized the usual Fermi Golden Rule to a system in which the number of final states is 1, but the interaction is spread over energy.) Because $\rho(\nu)$ is normalized, we can take $\rho(\nu) \approx 1/\Delta\nu$, where $\Delta\nu$ is the linewidth.

The 2S $|d\rangle \longrightarrow |c\rangle$ field-independent transition occurs at a magnetic field of 810 G, at a frequency close to 82 MHz. The detailed lineshape from the field-independent transition is a complicated problem that is discussed in Section 3.6.4. However, we can make a reasonable estimate of the width, as described below.

Because we cannot determine the strength of the rf field with any accuracy, we obtain an estimate of our expected transition rate using the following procedure. We measure the $|d\rangle \longrightarrow |c\rangle$ transition in the 1S state at the same frequency, which corresponds to a magnetic field of 62.5 G. Because this transition has an approximately linear Zeeman shift around 82 MHz, the linewidth is easily calculated. The transition rate is found from the measured $\gamma_{dc}(1S)$ using

$$\gamma_{dc}(2S) = \gamma_{dc}(1S) \frac{|\langle d|H_{dc}(2S)|c\rangle|^2}{|\langle d|H_{dc}(1S)|c\rangle|^2} \frac{\Delta\nu(1S)}{\Delta\nu(2S)}. \tag{3.52}$$

3.5.2 Linewidths

In the 1S state, the linewidth is found from the first order Zeeman effect

$$\Delta\nu(1S) = \frac{k_B T}{\mu_B} 1.25 \frac{\mathrm{MHz}}{\mathrm{G}} \approx 5.5\,\mathrm{MHz}, \tag{3.53}$$

at a magnetic field of 62.5 G and a temperature of 300 μK.

The thermal broadening in the 2S system $\Delta\nu(2S)$ can be estimated from

$$\Delta\nu(2S) = \left(\frac{k_B T}{\mu_B}\right)^2 5.231 \frac{\mathrm{Hz}}{\mathrm{G}^2} \approx 100\,\mathrm{Hz}, \tag{3.54}$$

at a magnetic field of 810 G and a temperature of 300 μK (see Eq. 3.17). This width is strongly temperature-dependent which is why we tried to find the lowest possible trap temperature at high fields (see Section 3.4.6).

3.5.3 Matrix element

In either the $1S$ or $2S$ manifolds, transitions between the $|d\rangle$ and $|c\rangle$ states are caused by the magnetic component of the rf: $\mathbf{B}_{rf} = B_{rf}\hat{x}\cos(\omega_{rf}t)$. The rf interaction energy is found from $H_{d,c}\cos(\omega_{rf}t) = \langle d| - \mathbf{B}_{rf} \cdot (\vec{\mu}_S + \vec{\mu}_I)|c\rangle$ (following the notation of Dale Fried [30]).

The matrix element between $|d\rangle$ and $|c\rangle$ is

$$H_{d,c} = \frac{\mu_B B_{rf}}{2\sqrt{2}} \left((g_e - g_I)\cos(\theta) + (g_e + g_I)\sin(\theta)\right), \tag{3.55}$$

with θ defined in Eq. 3.11. For the 1S measurement, $B = 62.5$ G, we have $\theta = -0.061$ radians. For the 2S measurement, $B = 810$ G, we have $\theta = -0.75$ radians. The quantity of interest,

$$\left|\frac{H_{dc}(2S)}{H_{dc}(1S)}\right|^2 = \left(\frac{(g_e - g_I)\cos(\theta_{2S}) + (g_e + g_I)\sin(\theta_{2S})}{(g_e - g_I)\cos(\theta_{1S}) + (g_e + g_I)\sin(\theta_{1S})}\right)^2 \approx \left(\frac{1}{18}\right)^2 \tag{3.56}$$

Note that the selection rule is the same for both transitions: $\Delta m = -1$. To satisfy this, $\mathbf{B}_{rf}$ must be perpendicular to the trapping field. At high trap bottom fields, the spins are mostly aligned along the z -axis, and the rf transition is possible only if $\mathbf{B}_{rf}$ is radial. We have two sets of rf coils wrapped around our cell: one designed to produce an axial rf field, the other designed to produce a radial one. For details and characterizations of these coils, see Fried [30]. At high fields, we thus use the transverse rf coil.

3.5.4 The transverse rf coil at 82 MHz

The transverse rf coil exhibits a resonance with the cell peaking at 83 MHz. This resonance causes heating in the cell, and atom loss unrelated to any hyperfine resonance. This can be seen in Fig. 3-13. All the atoms in this trap are at magnetic fields much lower than 63.3 G (the magnetic field corresponding to 83 MHz). Thus the atom loss is due to another mechanism, which we believe to be eddy-currents in the cell's copper coating, which absorb part of the rf, heat the cell, and in some spots, are hot enough to boil helium off the cell walls, causing background gas collisions that remove atoms from the trap.

Since we are interested in a transition at 82 MHz, we need to understand the response of a resonant atomic sample (whether 1S or 2S) to both the cell heating atom losses and the rf transition. A sample decay model must include both the decay due to rf heating and to the $|d\rangle \rightarrow |c\rangle$ transition.

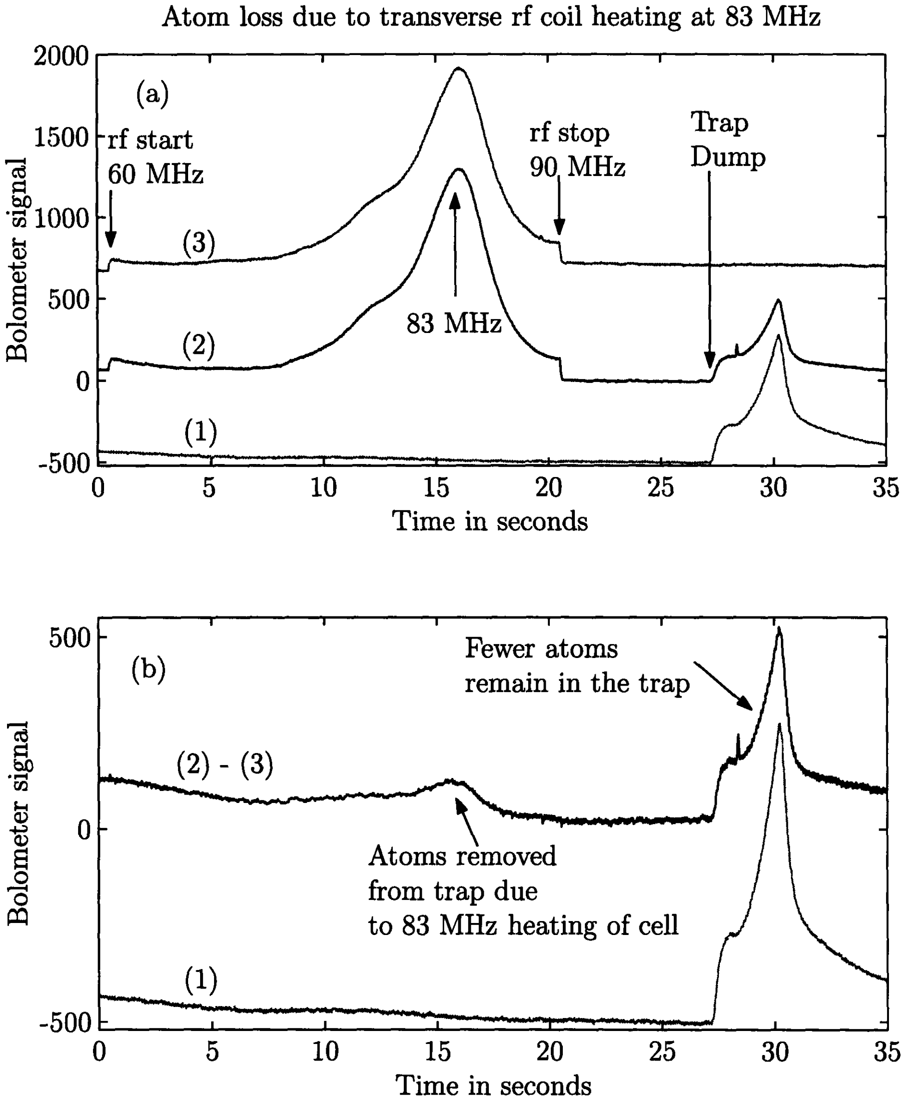

Atom loss due to transverse rf coil heating at 83 MHz

Figure 3-13: Transverse rf coil resonance with the cell at 83 MHz and resulting atom loss.

In this figure, the transverse rf coil frequency is ramped linearly from 60 MHz to 90 MHz, as indicated by the arrows, at a power of -6 dBm. After a few seconds, the lower pinch magnet is ramped down and the atoms are dumped out of the trap onto the bolometer.

Plot(a): Curve (1) shows a simple atom dump, without rf ramp. Curve (2) has an rf ramp, with atoms in the trap. Curve (3) shows the rf coil 83 MHz resonance without atoms in the trap (hence the lack of atom dump signal).

Plot(b): Curve (1) is the same as in Plot(a), simple atom dump without rf. The other curve is the subtraction of curve(3) from curve(2): a the rf resonance signal is subtracted and only atomic recombination signal is left. A small recombination signal due to atom removal from the trap is visible at a frequency of 83 MHz, the peak of the resonance in Plot(a). This is consistent with the relative size of the atom dump: the atomic dump signal is smaller with rf than without.

The 83 MHz atom loss is due to cell heating, not to rf hyperfine resonance, since all the atoms in this trap are at magnetic fields far below 63.3 G (the magnetic field corresponding to a 1S $|d\rangle$ to $|c\rangle$ transition frequency of 83 MHz).

	Decay Rates (second^{-1})	
rf power	on resonance	off resonance
-9 dB	0.047(5)	0.038(2)
-12 dB	0.023(3)	0.021(2)
-100 dB	0.017(2)	0.014(1)

Table 3.4: 1S $|d\rangle \rightarrow |c\rangle$ decay rates at 82 MHz as a function of rf power and sample magnetic field. The on-resonance decay rates correspond to magnetic traps where the trapped $|d\rangle$ atoms atoms are resonant with the 82 MHz frequency. The off-resonance decay rates correspond to traps with magnetic fields either too high or too low to be resonant at 82 MHz.

3.5.5 Estimate of the 2S $|d\rangle \rightarrow |c\rangle$ decay rate from the 1S results

We can measure the decay of the 1S sample as a function of time at magnetic fields above, below, and at 62.5 G, where 82 MHz is resonant with the $|d\rangle$ to $|c\rangle$ transition.

The measurement method is to trap the 1S atoms at the desired fields, and then perform $1S-2S$ spectroscopy at the peak of the $1S-2S$ resonance while simultaneously applying the rf field, and fitting the $|d\rangle$ state $1S-2S$ signal as a function of time to a decaying exponential. Although the 1S $|c\rangle$ atoms are mostly trapped at traps with $B_{\text{min}} > 50$ G, the $1S-2S$ transition is very narrow and resonant only with 1S $|d\rangle$ state atoms, and hence detects the $|d\rangle \rightarrow |c\rangle$ decay.

For the atoms detuned from the 82 MHz rf (at magnetic fields too low or too high to be resonant),

$$N_d(t) = N_d(0)\exp(-\gamma t). \tag{3.57}$$

γ incorporates the loss processes described below.

Several processes go into the 1S $|d\rangle$ sample decay. The first is the usual two-body decay of the $|d\rangle$ state atoms through dipolar decay. The second is the collisions loss due to helium background gas boiled off the retromirror by the $1S-2S$ laser beam. This second process dominates during spectroscopy. It may not be entirely accurate to model the decay as exponential (it involves both one- and two- body processes), however for the purposes of this measurement, such a fit is adequate.

If the trapped atoms are resonant with the 82 MHz rf,

$$N_d(t) = N_d(0)\exp(-\gamma' t) = N_d(0)\exp(-(\gamma+\gamma_{dc})t) \tag{3.58}$$

where γ_{dc} is the decay rate due to the 1S $|d\rangle \rightarrow |c\rangle$ losses.

The measured decay rates are listed in the table 3.4. The power listed is the frequency synthesizer's output power, after this the rf frequency is amplified by a 20 dB amplifier before going to the transverse rf coil. Although the decay rates are always larger on resonance, they are only significantly so at a power of -9 dBm. At this power, the atom loss due to coil heating is already quite large.

Using the 1S $|d\rangle \rightarrow |c\rangle$ decay rates at 82 MHz and -9 dBm of the transverse rf coil listed in table 3.4, we can estimate the 2S $|d\rangle \rightarrow |c\rangle$ at 82 MHz using Fermi's Golden Rule, Eq. 3.52, the ratio of the matrix elements Eq. 3.56 and the linewidths Eqs. 3.53 and 3.54.

Altogether this results in a 2S $|d\rangle \rightarrow |c\rangle$ decay rate

$$\gamma_{dc}(2S) \simeq 170\,\gamma_{dc}(1S) = 170 \times 0.009\,\mathrm{sec}^{-1} = 1.5\,\mathrm{sec}^{-1}. \tag{3.59}$$

It should be noted that this result is strongly dependent on the temperatures at low and high fields, and $\gamma_{dc}(2S)$ could be as low as 0.5 sec^{-1} or as high as 2 sec^{-1} for temperatures in the 200 to 400 μK range.

3.5.6 Complete model of the time dependence of the 2S $|d\rangle \rightarrow |c\rangle$ signal

We can use the inferred value of $\gamma_{dc}(2S)$ to model the expected 2S hyperfine $|d\rangle$ to $|c\rangle$ state transition signal strength, and find the optimal parameters for the observation.

The 2S signal is subject to four separate decay rates, two for each time scale of the observation.

The first time scale is the overall duration of the spectroscopy, usually close to 200 seconds, during which roughly 10,000 243 nm laser pulses interact with the atoms. We denote this time as t_l where l is for "long". The second time is the interval between the laser pulse creating the 2S atoms and the 2S atom quench (observation). We denote this time as t_q where q is for "quench".

The two decay rates associated with the long time t_l are

- γ_{laser} = decay rate of 1S atoms during the spectroscopy, due to collisions with helium boiled off the cell retromirror by the laser. This decay rate also includes the 1S two-body decay, which is a smaller effect than the losses due to helium boiloff.

- γ_{rf} = decay rate of 1S atoms during the spectroscopy, due to collisions with helium boiled off the cell walls by rf coil eddy-current heating.

$\gamma_{rf} \gg \gamma_{laser}$ for an appreciable rf power. The total is $\gamma_l = \gamma_{rf} + \gamma_{laser}$.

The two decay rates associated with the quench time t_q are

- γ_{dc} = decay rate of 2S atoms from the $|d\rangle$ state to the $|c\rangle$ state, driven by rf

- γ_{nat} = natural decay rate of 2S atoms in our cell due to the natural lifetime of the 2S state and the stray electric fields in the cell.

Then the number of detected 2S $|c\rangle$ state atoms as a function of t_l and t_q can be written

$$N_{(2S,c)}(t_l, t_q) = \underbrace{\overbrace{\xi N_{(1S,d)}(t_l)}^{N_{(2S,d)}(t_l,t_q=0)} \exp(-\gamma_{nat}t_q)}_{N_{(2S,d)}(t_l,t_q)}(1 - \exp(-\gamma_{dc}t_q)), \tag{3.60}$$

where ξ is a factor including the $1S-2S$ excitation rate and the 2S detection efficiency, meaning that $N_{(2S)}$ corresponds to the detected number of Lyman-α counts.

The total number of detected 2S $|c\rangle$ state atoms is

$$N_{(2S,c)}(t_q) = \underbrace{\overbrace{N_{(2S,d)}(t_l = 0)\int_0^{t_l} \exp(-\gamma_l t)\mathrm{d}t}^{\text{Total } N_{(2S,d)}(t_q=0)}\exp(-\gamma_{nat} t_q)}_{\text{Total } N_{(2S,d)}(t_q)}(1 - \exp(-\gamma_{dc} t_q)). \tag{3.61}$$

The fraction of detected 2S $|c\rangle$ state to $|d\rangle$ state atoms is thus simply $1 - \exp(-\gamma_{dc} t_q)$.

The optimal quench time as a function of the 2S $|d\rangle$ decay rates

The signal-to-noise ratio (SNR) can be written

$$\begin{aligned} \text{Signal} &= N_c(t_q) = N_d(0)\exp(-\gamma_{nat} t_q)(1 - \exp(-\gamma_{dc} t_q)) \\ \text{Noise} &= \sqrt{N_c(t_q) + B} \\ \text{SNR} &= N_c(t_q)/\sqrt{N_c(t_q) + B}, \end{aligned} \tag{3.62}$$

where B is the background level, which is taken here to be a constant with respect to t_q, but is in fact a slowly decaying exponential due to fluorescence excited by the laser beam in some cell materials. We can then find the optimum t_q as a function of γ_{dc} and γ_{nat} by maximizing the SNR:

$$\frac{\mathrm{d}}{\mathrm{d}t_q} SNR = 0 = \dot{N}_c(t_q)\frac{(N_c(t_q)/2 + B)}{(N_c(t_q) + B)^{3/2}} \Rightarrow \dot{N}_c(t_q) = 0. \tag{3.63}$$

The resulting optimal quench time t_q is

$$t_q = \frac{1}{\gamma_{dc}} \ln\left(1 + \frac{\gamma_{dc}}{\gamma_{nat}}\right). \tag{3.64}$$

If we use our result from Section 3.5.5 $\gamma_{dc} = 1.5$ sec^{-1} and a natural decay rate $\gamma_{nat} = 12$ sec^{-1} (this is a typical value in our trap, larger than the real natural $2S$ decay rate of 8.2 sec^{-1}, because of the presence of stray electric fields, see [64]), we obtain $t_q \approx 80$ milliseconds. This time is extremely long, on the order of the 1/e time of the natural 2S decay. Our normal t_q, used for looking at 2S $|d\rangle$ atoms only, is usually closer to 5 ms.

This optimal value for t_q is only weakly dependent on γ_{dc}, as long as $\gamma_{dc} \ll \gamma_{nat}$.

Unfortunately, when we attempted to detect the 2S $|d\rangle$ to $|c\rangle$ signal at $t_q = 80$ ms, we discovered that one of our electric field plates used to quench the 2S atoms had an electric break in the cryostat, and was floating. The large resulting stray electric field (on the order of 0.5 volts/cm) reduces the lifetime of the 2S atoms from 80 milliseconds to 20 milliseconds. Under these conditions, the experiment is not feasible (the 2S $|d\rangle \rightarrow |c\rangle$ signal strength is on the level of the noise, as described in the next section).

3.5.7 Estimating the 2S $|c\rangle$ state signal strength

Now that we have estimates for both γ_{dc} and t_q, we know the fraction of 2S $|c\rangle$ atoms $N_c(t_q)$ expected for a certain total number of 2S $|d\rangle$ state atoms $N_d(t_q)$

$$\frac{N_c(t_q)}{N_d(t_q)} = 1 - \exp(-\gamma_{dc} t_q) \approx 4\% \text{ to } 14\% \tag{3.65}$$

for γ_{dc} ranging from 0.5 to 2 sec^{-1}.

For t_q of 80 ms, we find a total 2S $|d\rangle$ signal of $N_d(80\text{ms}) \approx 230$ counts per trap at 810 G. Thus $N_c(80\text{ms})$ can be estimated to be between 10 and 35 counts. Our noise (total background + 2S count shot noise) is approximately 17 counts, on the same order as the $|c\rangle$ state signal. Moreover the shot-to-shot laser power fluctuations make the noise level effectively much higher. The 243 nm laser power changes due to pointing instability, dye jet bubbles, doubling cavity dropouts, up to one third from shot to shot. The 2S signal is dependent on the square of the laser power, and can thus change by a factor of 2 from shot to shot. This results in $\sqrt{N}$ noise which is much larger than what is listed here.

Thus unless the high field 2S $|d\rangle$ signal can be enhanced by a factor of 4 or more, the 2S $|d\rangle \rightarrow |c\rangle$ signal will not be easily visible in our experiment. With the large stray electric field due to the floating quench field plate, it is not surprising that we never were able to detect a signal.

3.6 Expected Sources of Broadening and Shifts

3.6.1 Accuracy of rf source

Our rf source is a Hewlett-Packard 8662A Frequency Synthesizer [46]. It uses an external 10 MHz source (provided by a LORAN-C frequency standard [103] locked to the Nantucket transmitting station) as a clock. The LORAN-C maintains a long term stability of 1×10^{-12}.

When we compare 10 MHz output from the HP 8662A and the LORAN-C, the drift is less than 2 degrees per day, or $\Delta\nu/\nu < 7\times10^{-13}$. This means that our frequency source has the same characteristics as the source of the LORAN transmitter.

3.6.2 Magnetic and thermal broadening

Our main source of broadening and systematic error is Zeeman broadening through the thermal distribution of our sample in a magnetic trap. The frequency as a function of magnetic field is shown in figure 3-5. We can estimate the broadening as in equation 3.54:

$$\Delta\nu(2S) = \left(\frac{k_B T}{\mu_B}\right)^2 5.231 \frac{\text{Hz}}{\text{G}^2}, \tag{3.66}$$

which is between 50 and 300 Hz for temperatures between 200 and 500 μK.

Since the 2S atoms are orbiting the magnetic trap while the the resonant field is on, the signal may in fact exhibit motional narrowing [112].

The quadratic nature of the frequency-vs-magnetic field around the 2S $|d\rangle \rightarrow |c\rangle$ field-independent point means that not only will the thermal magnetic field spread broaden the signal, but it will also systematically shift the frequency downwards. To do an accurate measurement of the frequency, we need to be able to realistically model our lineshape as a function of trap parameters and temperature, so that we can extract the correct field-independent point.

To help us understand the systematic shifts and broadenings, we can change our experimental parameters in controlled ways. We can make our sample colder or warmer by changing the quadrupole current (radial trap frequency, see equations 3.43 and 3.50). We can change the magnetic trap bottom by a fraction of a gauss by changing the bias magnet current by small amounts. These changes should allow us to test our lineshape model and measure the field-independent frequency accurately, despite these shifts and broadenings.

3.6.3 Magnetic field fluctuations

Our magnets are powered by computer-controlled current supplies. The two magnets that contribute the most to the bias field (trap minimum) are the bias magnet and lower pinch magnet. Their currents are monitored across 0.01 Ohm air-cooled shunts. The power supplies are ramped up to roughly 40 A, or 500 G for the bias magnet, and 100 A or 300 G for the lower pinch magnet. Fluctuations in these power supplies would cause the largest magnetic field fluctuations.

Initially, the bias magnet power supply (an HP 6012A [45]) drifted by more than 1% in the first minute after ramp-up, corresponding to a magnetic field drift of 8 G during the time of the spectroscopy (roughly 2 minutes). We designed an external proportional feedback limiting the drift to below 1 part in 10,000 per minute, or less than 1 gauss drift for the duration of spectroscopy (see Appendix C).

The lower pinch magnet power supply (an HP 6260B [44]) drifts by 1 part in 1000 per minute, again less than 1 gauss drift for the duration of spectroscopy. Since the thermal spread of the atoms is on the order of several gauss, this we consider a 1 gauss drift to be acceptable.

Future experiments may want to incorporate proportional feedback on all large power supplies, although this requires an bulky external shunt and fine tuning the electronics to avoid amplifying the natural oscillation of the power supply - magnet coil inductance system.

3.6.4 Lineshape modelling

We can model the lineshape using numeric calculations of a two-level system, where the motion of the atom is included as a time-varying interaction frequency. The diagonal part of the Hamiltonian is

$$H_0 = E_1|1\rangle\langle 1| + E_2|2\rangle\langle 2|. \tag{3.67}$$

The interaction potential is

$$U(t) = H_{12}\exp(i\omega(t)t)|1\rangle\langle 2| + H_{12}\exp(-i\omega(t)t)|2\rangle\langle 1|, \tag{3.68}$$

and $H_{12} = H_{dc}$ is defined for us in equation 3.55.

In the usual case where $\omega(t) =$ constant and $U_{12} = U_{21}^* = H_{12}\exp(i\omega t)$, the time evolution of the state coefficients is described by

$$i\hbar\dot{c}_k(t) = \Sigma_{n=1}^{2} U_{kn}(t)\exp(i\omega_{kn}t)c_n(t) \tag{3.69}$$

where $\omega_{kn} = (E_k - E_n)/\hbar$. The result is Rabi's formula:

$$\begin{aligned} |c_2(t)|^2 &= \frac{H_{12}^2}{\Omega^2\hbar^2}\sin^2(\Omega t) \\ |c_1(t)|^2 &= 1 - |c_2(t)|^2. \end{aligned} \tag{3.70}$$

$$\Omega = \sqrt{(H_{12}/\hbar)^2 + (\omega - \omega_{21})^2/4} \tag{3.71}$$

is the Rabi frequency.

In our case, the detuning $\omega - \omega_{21}$ is time varying as the atom moves through the trap, and the differential equations for the state coefficients are

$$\begin{aligned} i\hbar\dot{c}_1(t) &= H_{12}\exp(i(\omega(t) - \omega_{21})t)c_2(t) \\ i\hbar\dot{c}_2(t) &= H_{12}\exp(-i(\omega(t) - \omega_{21})t)c_1(t). \end{aligned} \tag{3.72}$$

$\omega(t)$ is set by the particular trajectory of each atom.

Time-dependent frequency shift

The frequency shift from the field-independent point $f_{\rm FIP}$ (equation 3.16) can be written in terms of the potential

$$U(\mathbf{r}) = \frac{m}{2}\left(\omega_\rho^2(x^2+y^2) + \omega_z^2 z^2\right) = \mu_B(B(\mathbf{r}) - B_{\min}), \tag{3.73}$$

where $B_{\min}$ is the lowest field in the magnetic trap.

We can approximate $\nu(B)$ around B_0 as a parabola (see figure 3-5, equation 3.17).

To calculate the frequency shift seen by an atom in the trap, we use

$$\Delta\nu = \nu(B) - f_{\rm FIP} \simeq \beta(B - B_0)^2. \tag{3.74}$$

Since $B - B_0 = U/\mu_B + B_{\min} - B_0$,

$$\Delta\nu(\mathbf{r}) \simeq \beta \left(\frac{U(\mathbf{r})^2}{\mu_B^2} + \frac{2U(\mathbf{r})}{\mu_B}(B_{\min} - B_0) + (B_{\min} - B_0)^2 \right). \tag{3.75}$$

The equations of motion of an atom in the potential U are

$$\begin{aligned} x(t) &= x_0 \sin(\omega_\rho t + \phi_x) \\ y(t) &= y_0 \sin(\omega_\rho t + \phi_y) \\ z(t) &= z_0 \sin(\omega_z t + \phi_z), \end{aligned} \tag{3.76}$$

for an atom with energy $E = m/2\left((x_0^2 + y_0^2)\omega_\rho^2 + z_o^2\omega_z^2\right)$. The equations of motion along with equation 3.75 describe $\omega(t) - \omega_{21} = 2\pi(\Delta\nu_{rf} - \Delta\nu(t))$ where $\Delta\nu_{rf} = \nu_{rf} - f_{\mathrm{FIP}}$ is the detuning of the rf frequency synthesizer from the field-independent frequency f_{FIP}.

The differential equations 3.72 can be numerically integrated for different trajectories and energies, and a lineshape (sum of $|c_2(t)|^2$ for different $\Delta\nu_{rf}$) can be found for varying temperatures, magnetic trap frequencies and minimum field $B_{\min}$.

3.7 Future Possibilities for 2S $|d\rangle$ to $|c\rangle$ Precision Measurements

Several difficulties prevented us from successfully completing the 2S hyperfine splitting experiment.

The electric disconnect of one of the quench field plates, and the resulting large stray electric fields in the cell, contributed to the low $1S - 2S$ count rate. In combination with the relatively small 2S $|d\rangle$ to $|c\rangle$ decay rate $\gamma_{dc}(2S)$ (described in section 3.5.5), and the large sample decay rate due to the transverse rf coil heating, the estimated signal is too small to be detectable.

The quench field plate can be reconnected, but the other factors would require a new cell and a more favorable rf coil design. It is not clear why the cell has a heating resonance with the transverse rf coil at 83 MHz, making specific design recommendations difficult. If a new cell without a heating resonance were made, a special rf coil designed to deliver more power at 82 MHz would be helpful. In the current circumstances, however, we are not limited by rf power, but by heating losses.

Other problems in the current experiment are the low count rate at high magnetic fields, and the relatively high temperatures. These are related: they are both due to the possible axial magnetic field profiles at high magnetic fields.

Our high magnetic field mainly has contributions from two magnet coils: the lower pinch and the bias. The trap is located at the dip between the two. In our usual low field traps, the bias is almost zero, and the axial trap shape is determined by secondary coils. This allows us to maintain a low axial trap frequency, less than 100 Hz.

However, at high magnetic fields, the axial shape of the trap is basically a wedge between two very large magnetic fields, with an axial trap frequency that is probably closer to several hundred Hz. This causes the sample temperature to warm considerably (see section on adiabatic trap change 3.4.5). To cool the sample, we are forced to open the trap radially, which reduces the signal rate (see section 3.4.6).

Our $2S|d\rangle \rightarrow |c\rangle$ signal depends crucially on the overall 2S signal rate and the temperature of the initial sample (see equation 3.54). In our current system we have to choose between the signal rate and the sample temperature.

If our magnetic field configuration were different, and allowed for a constant field to be added to our low field trap, through a separate coil, we could maintain the trap frequencies and temperature of the low field trap (if the low-to-high field ramp were done adiabatically). Then the 2S signal rate would be as high as at low fields, roughly a four-fold increase, and we could expect to see a $2S|d\rangle \rightarrow |c\rangle$ signal well above the noise.

Although adding such a new coil is not conceptually difficult, our current magnet system does not allow such an addition without a major overhaul due to space and wiring constraints. However, in a new magnetic trap design, it may be desirable to add the capability of raising the overall trap field by up to 1000 Gauss, to study the $2S|d\rangle \rightarrow |c\rangle$ transition as well as systematic effects due to large magnetic fields.

Chapter 4

The Quest to Trap Deuterium

4.1 Introducing Deuterium

In our experiment, deuterium is a natural candidate for trapping. Deuterium is the fermionic isotope of hydrogen, with a nucleus (the deuteron) consisting of one proton and one neutron. The most important differences between hydrogen and deuterium are their quantum statistics, mass, the binding energy and recombination cross length on the surface of liquid helium, and the hyperfine spectrum.

Deuterium-hydrogen collisions may be beneficial for hydrogen trap-loading (compared to hydrogen-helium collisions): thermalization with a lighter species is usually beneficial. Deuterium is not a good candidate for fermion superfluidity, since its cross-section is quite small [61, 47].

Interest in deuterium is high because trapped fermions and fermi-bose mixtures are of great current interest. Although fermions do not exhibit a Bose-Einstein-condensation-like phase transition when their phase space density is increased, they have been cooled to temperatures below the Fermi degeneracy temperature in many laboratories [18, 106, 97, 33, 37, 92].

The search for a superconductivity-like Cooper pairing [4] of the fermions, and Bose condensation of these pairs, is underway (see, for instance, Viverit et al. [110] and Onofrio and Presilla [82]).

4.1.1 Overview of past deuterium experiments

Historically, atomic deuterium has been difficult to study as a gas in cryogenic environments, with experiments conducted by different groups producing varying results or no results at all. Different observation techniques and uncertainty in the confinement cell volume-surface geometry, helium film-thickness, or detection calibration, usually prohibit the measurement of a full set of physical characteristics (surface binding energy, surface or bulk recombination cross lengths, different decay rates). Often only one or the other of the binding energy or recombination cross length is measured. Moreover, the experiments are conducted at different temperatures and magnetic fields, making it difficult to compare experimental results directly.

In 1980, in Amsterdam, Silvera and Walraven [101] confined high-field-seeking spin-polarized $D_\downarrow$ deuterium in a superfluid ^{4}He coated cell. The density of 10^{14} cm^{-3} was two orders of magnitude less than had been achieved with hydrogen [111, 12]. Silvera and Walraven measured a large surface binding energy of deuterium on ^{4}He, $E_b = 2.5(4)$ K, compared to 1.1 K for hydrogen. In 1985, Mayer and Seidel attempted to carry out low-temperature (<1K) electron-spin resonance (ESR) experiments on deuterium at Brown University, but were unable to detect a signal [70]. Mayer and Seidel conjectured that deuterium possesses an extremely large surface recombination cross length, on the order of 300 $\AA$, and thus recombines very fast on helium surfaces. For this estimate, Mayer and Seidel used the binding energy value of Silvera and Walraven.

In 1986, Shinkoda, Reynolds, Cline and Hardy [100] succeeded in carrying out low-temperature ESR experiments on deuterium. By measuring the recombination rate, Shinkoda et al. found a recombination cross length of 5600 $\AA$. The measured lifetime of deuterium in their experiment was 27 minutes, compared to more than 7 days for hydrogen under similar conditions. Shinkoda et al. suggested that this was mainly due to a larger one-body surface nuclear relaxation rate. The group of Walter Hardy at the University of British Columbia continued to carry out successful ESR and hyperfine resonance experiments on low-temperature deuterium [90, 41, 91, 40]. In particular, in 1995 Hayden and Hardy [40] estimated that the deuterium surface cross length is smaller than 30 $\AA$, which contradicts their previous result [100] as well as the estimate of Mayer and Seidel [70]. Hayden and Hardy explain the latter discrepancy by possible errors introduced by extrapolation from high magnetic fields (ESR experiments of Mayer and Seidel [70] at 0.3 tesla and Shinkoda et al. [100] at 4 tesla) to low magnetic fields (hyperfine resonance experiments of Hayden and Hardy [40]).

The most recent series of experiments on deuterium were carried out at Kyoto University by Arai, Yamane, Fukuda and Mizusaki in 1998 [2] using hyperfine resonance at low magnetic fields and in 2001 by Mosk, Reynolds and Hijmans [78] using 122 nm spectroscopy on deuterium's $1S - 2P$ transition at magnetic fields ranging from 4 to 6 tesla. These groups both find a significantly larger surface binding energy than Silvera and Walraven [101], between 3 and 4 K. Arai et al. report a much smaller recombination cross length than any previously found: 0.55(13) $\AA$. Both Arai et al. and Mosk et al. agree that the discrepancies in experimental results are likely due to the different magnetic field values. Magnetic field dependent Feshbach resonances [89] of deuterium can increase the recombination cross length at nonzero magnetic fields.

The MIT Ultracold Hydrogen group has previously unsuccessfully endeavored to trap deuterium. Working with deuterium is clearly much more challenging than working with hydrogen. The current interest in fermion trapping convinced our group to try once again to trap deuterium in our experiment. This chapter describes what we learned in the process.

4.1.2 Comparison of deuterium and hydrogen

The hyperfine structure of deuterium is shown in Fig. 4-1. As in hydrogen, the only trappable state is the low-field-seeking stretched state, denoted $|\zeta\rangle$. One can immediately see one disadvantage compared to hydrogen: in the case of hydrogen, one out of four atoms emitted by the discharge is in the low-field-seeking stretched state $|d\rangle$, which is the metastably trapped state. In the case of deuterium, only one out of six atoms emitted from the discharge is in the $|\zeta\rangle$ state.

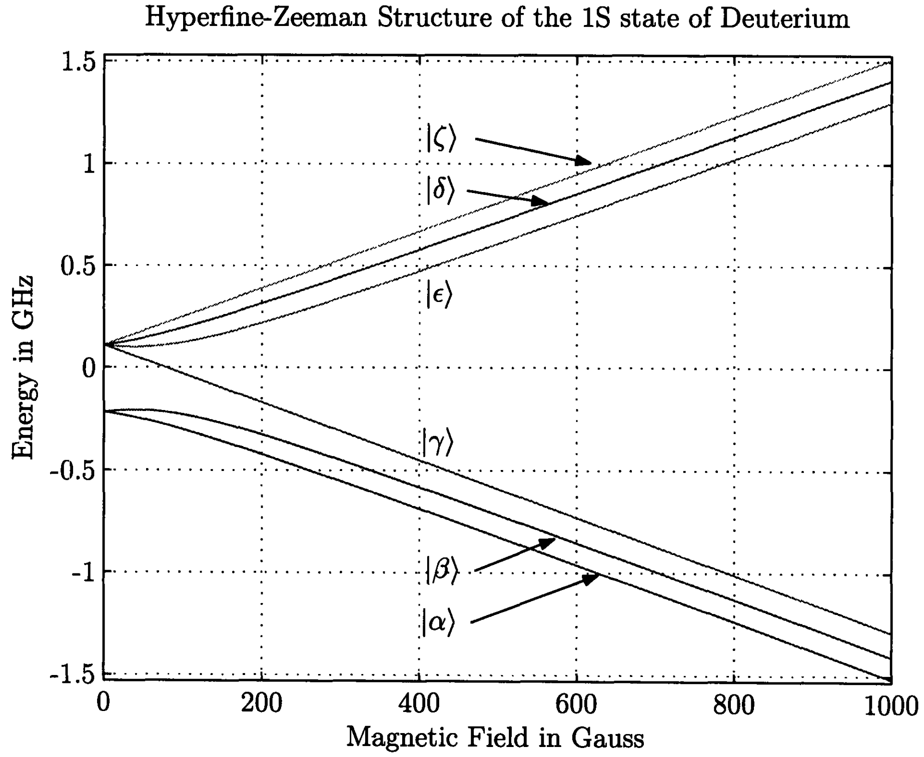

Figure 4-1: Hyperfine-Zeeman spectrum of the deuterium 1S state. 1S deuterium has 6 eigenstates in a magnetic field, compared to 4 for hydrogen. This is due to the spin 1 deuteron. These states are labelled $|\alpha\rangle$ to $\zeta\rangle$ in order of increasing energy. The trappable state is the stretched state $|\zeta\rangle$.

Properties of hydrogen and deuterium of interest in our experiment are summarized in Tables 4.1 and 4.2. These include physical and spectroscopic properties of molecular (4.1) and atomic (4.2) deuterium and hydrogen.

Deuterium's binding energy on liquid ^{4}He surfaces is much larger than that of hydrogen. Experiments have found values ranging from 2.5 K [101] to 4.0 K [2] for the binding energy of atomic deuterium on liquid ^{4}He. These varying results may be due to the recombination properties of deuterium at different magnetic fields (as explained by Arai et al. [2] and Mosk et al. [78]).

There are widely conflicting reports of the helium surface recombination cross length of deuterium, which are possibly due to magnetic-field-dependent recombination, such as Feshbach resonances [2, 78].

Property	Hydrogen	Deuterium
Molecular Binding Energy (eV) [113]	4.52	4.60
Boiling Point (K) [113]	20.35	23.45
Melting Point (K) [113]	14.0	18.55

Table 4.1: Physical properties of molecular hydrogen and deuterium

Property	Hydrogen		Deuterium	
Particle Type	Boson		Fermion	
Weight in amu	1.007825		2.014	
	1.14(1)	[95]	3.1(2)	[78]
^{4}He Binding Energy (K)	1.00(2)	[2]	3.97(7)	[2]
	1.15(5)	[77]	2.5(4)	[101]
Weighted average	1.11(1)		3.8(1)	
^{3}He Binding Energy	0.38(5)	[95]	2(1)	est.
Surface Recombination	0.20(3)	[77]	5600	[100]
Cross Length (Å)			300	[70]
	0.25(5)	[2]	0.55(13)	[2]
Weighted average	0.21(3)		?	
Dipolar decay (cm^3·sec^{-1})	1.2×10^{-15}	[104]		
(cm^3·sec^{-1}×K^{-1})			2.2×10^{-13} at 10 G	[60]
(cm^3·sec^{-1}×K^{-1})			1.3×10^{-14} at 1 T	[60]
$1S - 2S$ Energy (Hz)	2 466 061 413 187 103(46)	[80]	2 466 732 407 521 743(160)	[48]
Closest Tellurium Feature at 486 nm	b2 line 144 MHz away	[71]	b1 line 4.245 GHz away g1 closer, not measured	[32]

Table 4.2: Physical and spectroscopic properties of atomic hydrogen and deuterium. The deuterium surface recombination cross length value of Arai et al. [2] was measured at 39 gauss. Shinkoda et al. [100] measured a value of 5600 Å, four orders of magnitude larger, at 4 tesla. It is believed that magnetic field dependent processes, such as Feshbach resonances explain the discrepancy [2, 78]. Since our magnetic field values in the cell are below 1 tesla we use the former value in subsequent estimates.

Spin-exchange interactions between the different hyperfine states of deuterium have been studied by Koelman, Stoof, Verhaar and Walraven [59]. They predict that a gas of different hyperfine states will decay to a stable doubly-spin polarized gas of $|\zeta\rangle$ states only, which is analogous to what happens for hydrogen. Koelman, Stoof, Verhaar and Walraven [60] have discussed the lifetime of magnetically trapped deuterium through dipolar decay. They find a strong temperature and magnetic field dependence on the decay rate. This is markedly different from hydrogen, where the decay rates are fairly insensitive to the sample magnetic field and temperature, $g_{dd} \simeq 1.2 \times 10^{-15}$ cm^3·sec^{-1}. The deuterium decay rate $G_{\zeta\zeta} \simeq 10^{-14}$ cm^3·sec^{-1}K^{-1} at 1 tesla, and $G_{\zeta\zeta} \simeq 2.2 \times 10^{-13}$ cm^3·sec^{-1}K^{-1} at 10 G. Thus at low magnetic fields, the decay rate is comparable to or lower than that of hydrogen only below 5 mK. At 100 mK, the low-field decay rate is almost 20 times larger than that of hydrogen, resulting in a shortened sample lifetime. However, the larger collisional cross section of deuterium should allow faster thermalization of the sample, and hence faster evaporative cooling, which should limit the losses due to the large dipolar decay rate at high temperatures.

The electronic excitation spectrum of deuterium is similar to that of hydrogen and can be studied with the same laser systems as hydrogen. There are small differences due to the nucleus, which are interesting to study through precision spectroscopy [48, 15].

4.1.3 Deuterium and hydrogen recombination on helium surfaces

As described in Sections 2.3.3 and 2.4.2, two regimes characterize the interaction between hydrogen or deuterium and the cell walls. The high temperature regime is good for magnetic trap loading, due to the short surface residence time τ_{res} (Eq. 2.4), which hinders surface recombination losses. The low temperature regime is good for wall-free magnetic confinement as well as bolometric detection, due to the longer residence time which allows efficient surface recombination.

The residence time τ_{res} is strongly dependent on the atomic species (hydrogen or deuterium) through the helium surface binding energy E_b. The binding energy is also dependent on the helium surface composition (^{3}He or ^{4}He), see Table 4.2.

The binding energy of deuterium on ^{3}He has not been measured. However, given the discrepancies in the measured ^{4}He surface value (see Table 4.2), it is most likely not an easy measurement to perform. As in the case of hydrogen, a ^{3}He surface could reduce the binding energy by more than a factor of 2 compared to the ^{4}He energy. However, we can only assume a reduction in binding energy in the presence of ^{3}He, we don't know how large it is. The advantage of the smaller residence time due to the lower ^{3}He binding energy is also offset by ^{3}He's high vapor pressure, which can prevent atoms from accumulating in the trap. The vapor pressure can be expressed as a density. Rob deCarvalho [17] extrapolated the vapor pressure data from Pobell [85] to low temperatures, expressed as density. Fig. 4-2 uses this extrapolation.

The surface recombination and dwell times (Eqs. 2.3 and 2.4) for hydrogen and deuterium on ^{3}He and ^{4}He surfaces are shown in Fig. 4-3.

The important quantities that determine the surface residence and recombination times are described in Section 2.3.3. They are the equilibrium gas-surface densities, the recombination rate and the surface residence time. The equilibrium gas and surface densities n and σ are described by Eq. 2.2. The recombination rate is the inverse of the recombination time τ_{rec} in Eq. 2.3. The surface residence time τ_{res} is defined in Eq. 2.4.

The two timescales depend on several quantities that are species dependent. The thermal wavelength λ_{dB} and the average speed $\bar{v}$ of hydrogen and deuterium differ by a factor of $\sqrt{2}$ because of the mass difference. The helium surface binding energy E_b and surface recombination cross-length l_c are quite different for deuterium and hydrogen (see Table 4.2). Moreover, since there is no clear agreement on the measured E_b and l_c values for deuterium on ^{4}He (and no measured value for E_b of deuterium on ^{3}He at all), it is difficult to be certain of the predictive power any calculations based on

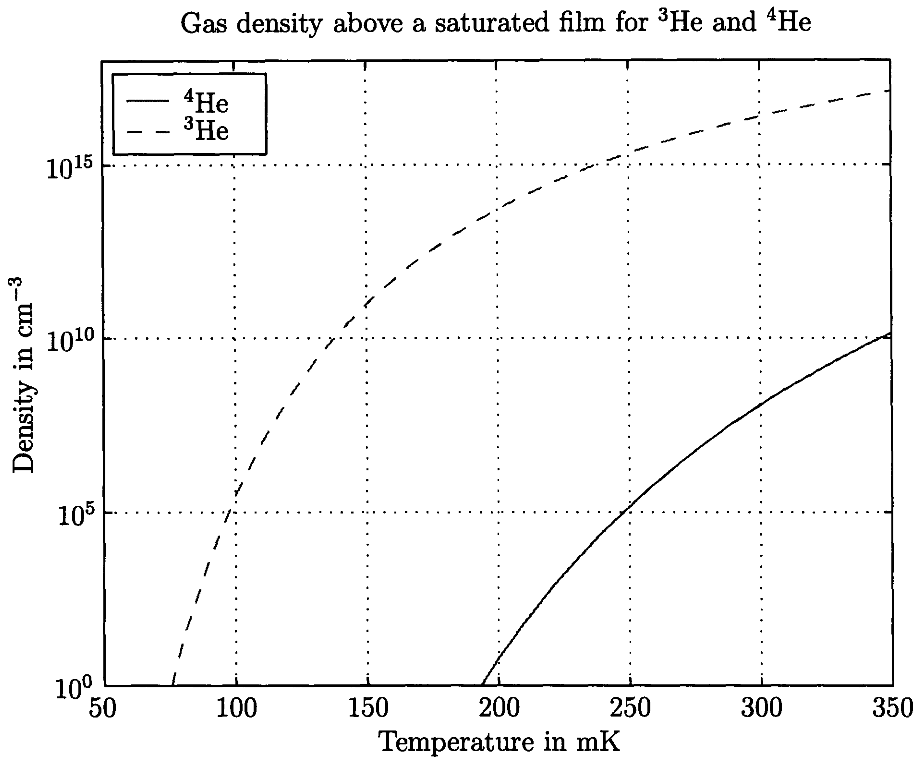

Figure 4-2: Density of ^{3}He and ^{4}He above a saturated film. The density of ^{3}He is substantially larger than that of ^{4}He, down to very low temperatures. It should be noted that these curves are low temperature extrapolations [17] of data taken above 600 mK [85], and that our films are usually subsaturated (which would decrease the gas density above the film significantly).

these values. The sticking probability s may also be dependent on the atom species. The following discussion is thus mostly qualitative.

At the same temperature T and bulk gas density n, the ratio of equilibrium surface densities of hydrogen and deuterium is

$$\frac{\sigma(H)}{\sigma(D)} = \frac{\exp((E_b(H) - E_b(D))/k_BT)}{\sqrt{2}}. \tag{4.1}$$

The ratio of recombination and residence times is

$$\frac{\tau_{\mathrm{rec}}(D)}{\tau_{\mathrm{res}}(D)} = \frac{\tau_{\mathrm{rec}}(H)}{\tau_{\mathrm{res}}(H)}\frac{\sigma(H)}{\sigma(D)}\frac{l_c(H)}{l_c(D)}\frac{s(D)}{s(H)}\frac{\exp((E_b(H) - E_b(D))/k_BT)}{\sqrt{2}} \tag{4.2}$$

If we combine these expressions (making the assumption of equal bulk gas densities), and also assume that the sticking probabilities are close to equal, this expression simplifies to

$$\frac{\tau_{\mathrm{rec}}(D)}{\tau_{\mathrm{res}}(D)} = \frac{\tau_{\mathrm{rec}}(H)}{\tau_{\mathrm{res}}(H)}\frac{l_c(H)}{l_c(D)}\frac{\exp(2(E_b(H) - E_b(D))/k_BT)}{2}. \tag{4.3}$$

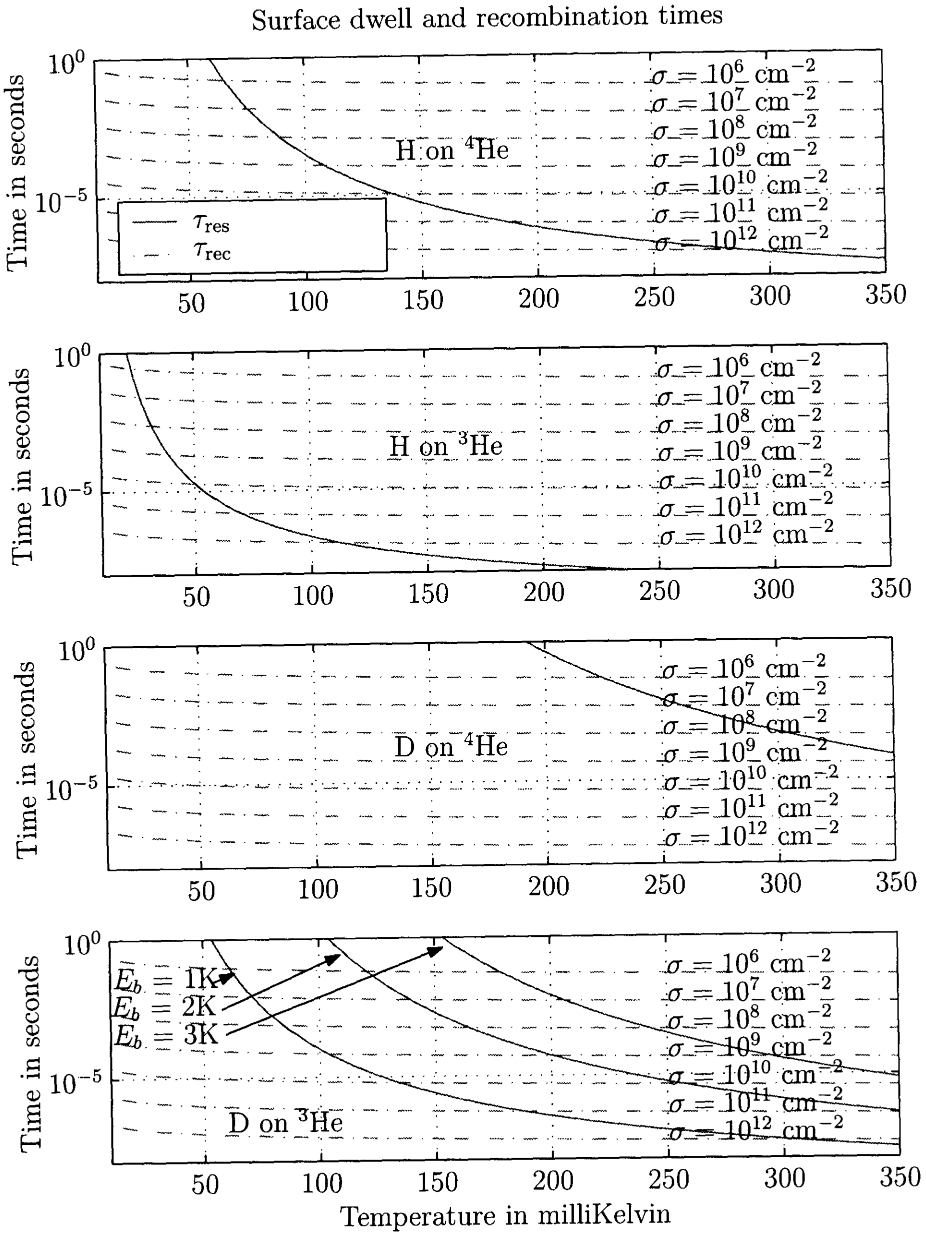

Figure 4-3: Surface residence and recombination times of hydrogen and deuterium on ^{4}He and ^{3}He. The values of the binding energy and recombination cross length used to calculate $\tau_{\rm res}$ 2.4 and $\tau_{\rm rec}$ 2.3 are those of Table 4.2. For deuterium, the ^{4}He binding energy E_b is taken to be 3.8 K, and the surface recombination cross length l_c is taken to be 0.55 Å. The sticking probability is taken to be 10%. Since the binding energy of deuterium on ^{3}He has not been measured, curves are shown for binding energies of 1, 2, and 3 K.

The ratio $\tau_{\text{rec}}/\tau_{\text{res}}$ indicates the surface regime of the hydrogen or deuterium. If $\tau_{\text{rec}}/\tau_{\text{res}} > 1$, the atoms will be more likely to bounce off the helium surface than to recombine, a good regime for trap loading, but bad for wall-free magnetic confinement or bolometric recombination detection. If $\tau_{\text{rec}}/\tau_{\text{res}} < 1$, the atoms will be more likely to recombine on the helium surface than to bounce back into the bulk, a good regime for wall-free magnetic confinement and bolometric detection, but a bad one for trap loading. If $\tau_{\text{rec}}/\tau_{\text{res}}$ is extremely small, the atoms emitted at the discharge may recombine entirely in the first few wall bounces during the expansion into the cell, a distance of a few centimeters. If τ_{res} and τ_{rec} become large, on the order of a tenth of a second, another process becomes dominant for the surface atoms: they skitter along the helium surface to the lowest or highest magnetic field regions, depending on whether they are high- or low-field seekers.

If the measured value for l_c of 5.5×10^{-9} cm [2] is correct, the expression 4.3 is entirely dominated by the exponential factor $\exp(2(E_b(H) - E_b(D))/k_B T)$. This factor can be extremely small: at 300 mK, for the ^{4}He binding energies of $E_b(H) = 1.1$ and $E_b(D) = 3.8$ K, it is 1.5×10^{-8}. This means that it is possible to detect deuterium on the bolometer but not load a significant amount of deuterium into our magnetic trap at that temperature. If l_c of deuterium is larger at 1 tesla than the value reported by Arai et al. [2], the deuterium surface recombination would be even more efficient at all temperatures. As we know from the experimental results summarized in Section 4.1.1, it is possible that l_c is quite large at 1 tesla.

The deuterium ratio $\tau_{\text{rec}}(D)/\tau_{\text{res}}(D)$ attains the favorable values of the 300 mK hydrogen ratio at a temperature of 900 mK, larger than our initial trap height and impossible to reach and cool from in our cell. Moreover, at 900 mK the large ^{4}He vapor pressure would be enough to destroy any trapped sample.

The conclusion from these timescale comparisons of hydrogen and deuterium is that probably the only hope for trapping deuterium through helium-surface cooling is introducing ^{3}He into the cell.

4.1.4 Difficulties in trapping deuterium and experimental goals

The larger helium surface binding energy and recombination cross length of deuterium compared to hydrogen are both impediments to trapping deuterium using helium-surface cooling. Since the binding energy determines the atom surface density, and hence recombination rate on the cell wall during the critical trap loading process, it is feared that many atoms would be lost during the first cooling stage, and no significant quantity of trapped deuterium would be seen.

The detection systems described in Chapter 2 are designed to detect a trapped sample. For instance, we have no method for detecting the quantity of deuterium on the helium surface, or even the deuterium flux from the discharge. Having a bolometer located at the cell top (close to the discharge) as well as at the cell bottom could help to understand the fate of deuterium in our cell.

Since we know how to trap hydrogen in our apparatus (even though the details of the trap loading process are not understood), we developed diagnostics for studying early stages of hydrogen trapping. The goal is to detect hydrogen in the cell as soon as possible after the discharge is run. This is done in two ways: $1S-2S$ optical excitation and detection several seconds after the discharge is run, and time-resolved bolometric detection during a series of discharge pulses. The $1S-2S$ detection of warm hydrogen samples is described in Section 4.2. The technique of bolometric time-resolved detection of discharge pulses is described in detail in Section 4.3. The bolometric study of individual hydrogen discharge pulses is described in Section 4.4. Both these detection methods provide insights into the hydrogen trap loading process, but both also suffer limitations in detection capability and possibilities for quantitative analysis. Nevertheless, they were the best available, and so we applied them to deuterium.

Discharge pulses from a deuterium discharge were studied using the bolometer, with pure ^{4}He and ^{3}He-^{4}He mixtures coating the cell walls. The purpose of the experiment described in Section 4.5 was to understand the behavior of deuterium in our discharge and cell, and possibly to trap it using ^{3}He-^{4}He mixtures for the film.

Although we were able to characterize the deuterium discharge and observe changes in the presence of ^{3}He, we were not able to detect a trapped deuterium sample. Magnetically trapping deuterium remains to be achieved. Section 4.7 of this chapter indicates how this may be done.

4.2 $1S-2S$ Detection of Warm Hydrogen

This section describes the results of the $1S-2S$ detection of warm hydrogen. Using this technique, we investigated the effects of varying experimental parameters relevant to trap loading on the total number of detected atoms. The experimental parameters were the discharge power (Section 4.2.3), the discharge duration (Section 4.2.4), the initial (trap-loading) cell temperature (Section 4.2.5), and the radial (quadrupole) trapping magnetic field (Section 4.2.6). These parameters were varied from their optimal values, which are 3 dBm, corresponding to a peak power of 10-30 watts after amplification, for the discharge power, 8 seconds of 1 ms pulses at 50 Hz for the discharge duration, 270 mK for the initial cell temperature, and 9600 G for the radial trapping field at the cell walls.

4.2.1 Description of the $1S-2S$ detection of warm hydrogen

The procedure for the $1S-2S$ detection of warm hydrogen is as follows. The discharge is pulsed while all magnets are ramped up. The loading magnet (at the bottom of the cell) must be lowered before the MicroChannel Plate (MCP) detector can be used. This is because the Lyman-α MCP detector is in the fringe field of the loading magnet, and this field deviates the MCP electrons, prohibiting efficient electron pulse amplification. The $1S-2S$ detection happens a few seconds after the discharge has stopped, which is enough time for evaporative cooling to start over the lower pinch barrier. The temperature of the sample is expected to be either at or a bit below the temperature of the cell, which can be varied from 100 to 300 mK. The temperature of the gas is quite warm compared to our normal $1S-2S$ detection regime (below 10 mK).

We were not able to measure the temperature of the warm sample using $1S-2S$ detection: the $1S-2S$ double-exponential signal was weak and very broad compared to the signal of a colder sample. This is because the density of the hydrogen in the laser beam was almost one hundred times smaller. Even though the initial number of hydrogen atoms in the cell during trap loading is larger than the number after evaporative cooling, the $1S-2S$ signal is smaller, because it depends on the atom density at the laser beam focus. The statistical noise on the warm hydrogen signal is such that the double-exponential linewidth could not be measured to better than a factor of 2, and no meaningful temperature measurement could be made.

4.2.2 Comparison of warm and cold sample data, I_{warm} and N_{cold}

The $1S-2S$ signal amplitude is proportional to the number of atoms in the laser beam. We compared the warm sample $1S-2S$ signal amplitude (henceforth denoted I_{warm}) with bolometer data. The bolometer data is the integrated bolometer signal when the atoms are dumped out of the trap after a stage of magnetic forced evaporation. The bolometer detects the amount of cold, trapped hydrogen, and the integrated bolometer signal is thus proportional to the number of atoms in the trap (henceforth denote N_{cold}).

We compared I_{warm} and N_{cold} as a function of trap loading parameters: the discharge power, duration, cell temperature and magnet configuration. We would normally expect these two sets of data to give similar results, eg the number of atoms in the cell during the trap loading phase should be proportional to the number remaining after evaporative cooling.

If this technique allowed us to predict the optimal parameters for hydrogen trapping, it might also be possible to employ it with warm deuterium samples right after the discharge is run.

4.2.3 Discharge power

The data in Fig. 4-4 show the dependence of both N_{cold} and I_{warm} on the discharge power. The normal trap loading value 3 dBm. The other trap loading parameter values are listed above.

These results show that I_{warm} is much less sensitive to the discharge power than N_{cold}. This may have to do with the cell temperature evolution after the discharge is run, while the trap is loaded. A smaller discharge power causes less heating of the cell, and hence a lower cell temperature and a faster cooling time.

The prevailing trap loading theory, described by David Landhuis [65], is that the shortest possible cell cooling time is preferred. This short cooling time would minimize the time spent at certain 'sticky' temperatures between 100 and 200 mK, where the hydrogen is much more likely to be lost on the cell walls. The I_{warm} data

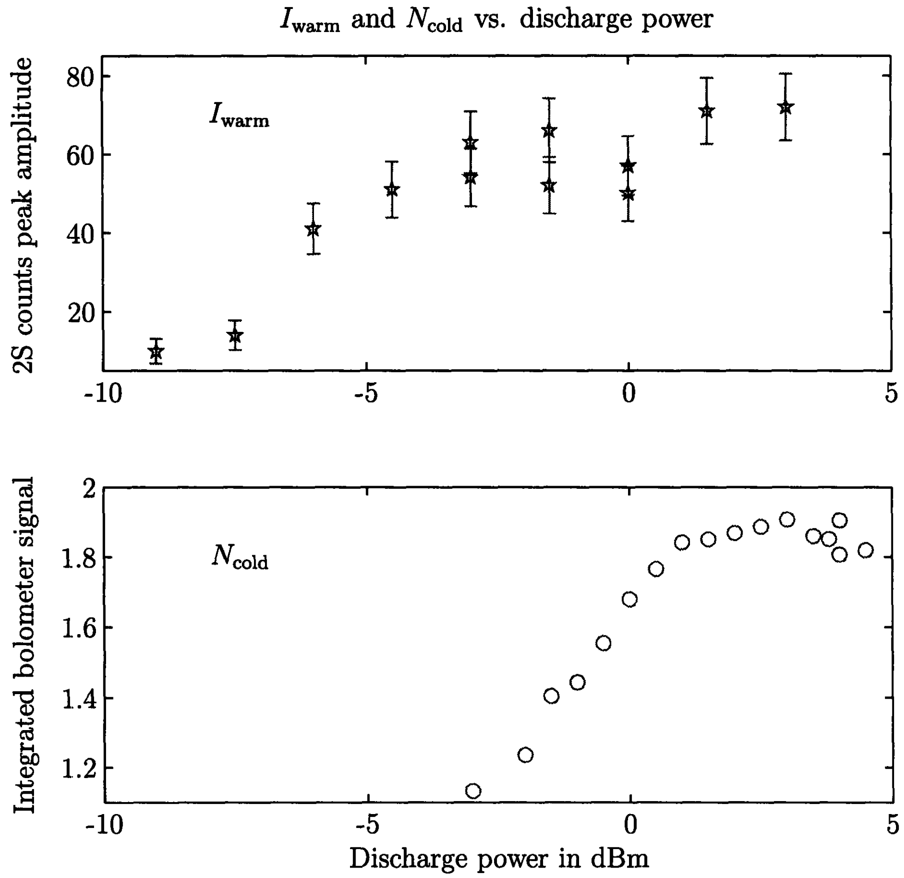

Figure 4-4: I_{warm} and N_{cold} as a function of the discharge power. I_{warm} is fairly insensitive to the discharge power down to very low powers, however N_{cold} shows a much greater sensitivity.

shows that in fact a *longer* cooling time is preferred, and that losses due to the cell cooling trajectory happen during the early stages of evaporative cooling, since they are visible in the N_{cold} data, but not in the I_{warm} data.

The hydrogen surface density is described by Eq. 2.2, and is proportional to the gas density near the cell walls. The gas density of atoms in the magnetic potential is

$$n(\mathbf{r}) = n_0 \exp(-U(\mathbf{r})/k_B T) \tag{4.4}$$

where n_0 is the density at the trap bottom (peak density). If the temperature of the trapped gas decreases, so does the gas density near the walls, and hence the surface density will also be lower.

Since the surface density is proportional to the recombination rate, it is possible that starting evaporative cooling at a higher cell temperature allows the sample to cool and decreases the hydrogen wall density at lower (sticky) cell temperatures. This would explain the discrepancy between the I_{warm} and N_{cold} data.

4.2.4 Discharge duration

The data in Fig. 4-5 show how N_{cold} and I_{warm} depend on the discharge duration. (The discharge is normally on for 8 seconds, pulsed for 1ms at 50 Hz.)

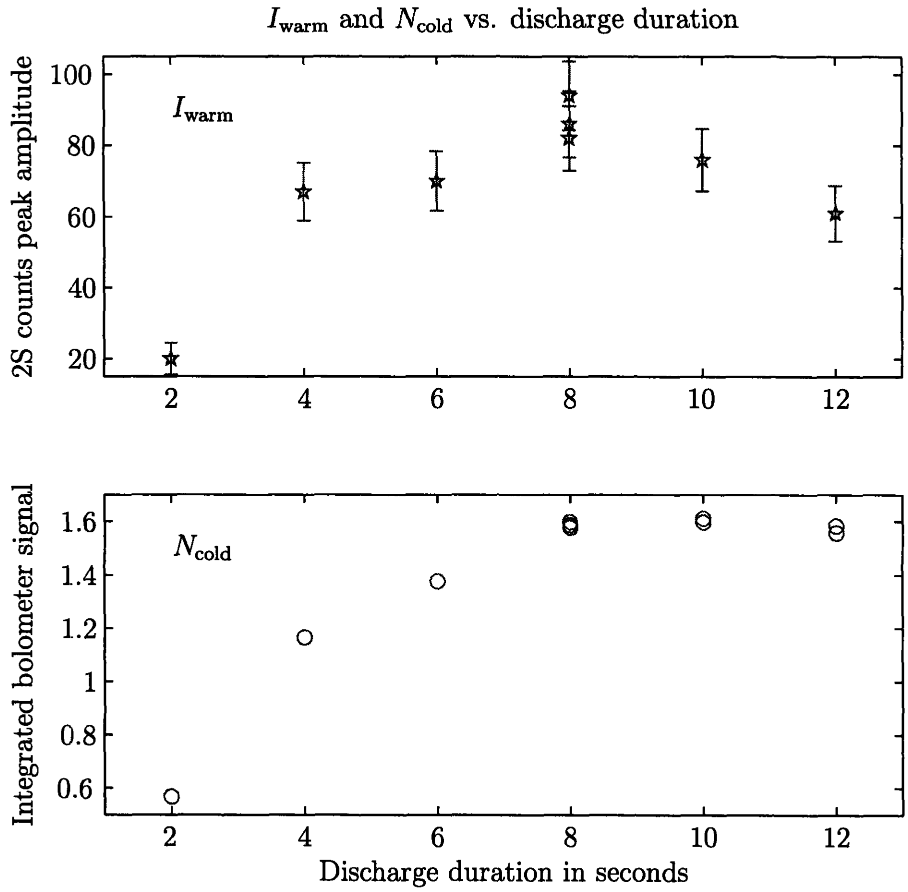

Figure 4-5: I_{warm} and N_{cold} as a function of the discharge duration. I_{warm} and N_{cold} are very well correlated.

I_{warm} and N_{cold} exhibit the same overall dependence on the discharge duration, which suggests that the number of atoms emitted into the cell, and ultimately trapped is proportional to the duration of the discharge.

The upper limit on the number of trapped atoms for long discharge durations is part of the trap loading process that is not understood, but clearly occurs quite early after the discharge is run, since it is visible in I_{warm} as well as N_{cold}.

4.2.5 Initial cell temperature

The data in Fig. 4-6 show how N_{cold} and I_{warm} depend on the initial cell temperature. (The usual trap loading cell temperature is at or above 270 mK.)

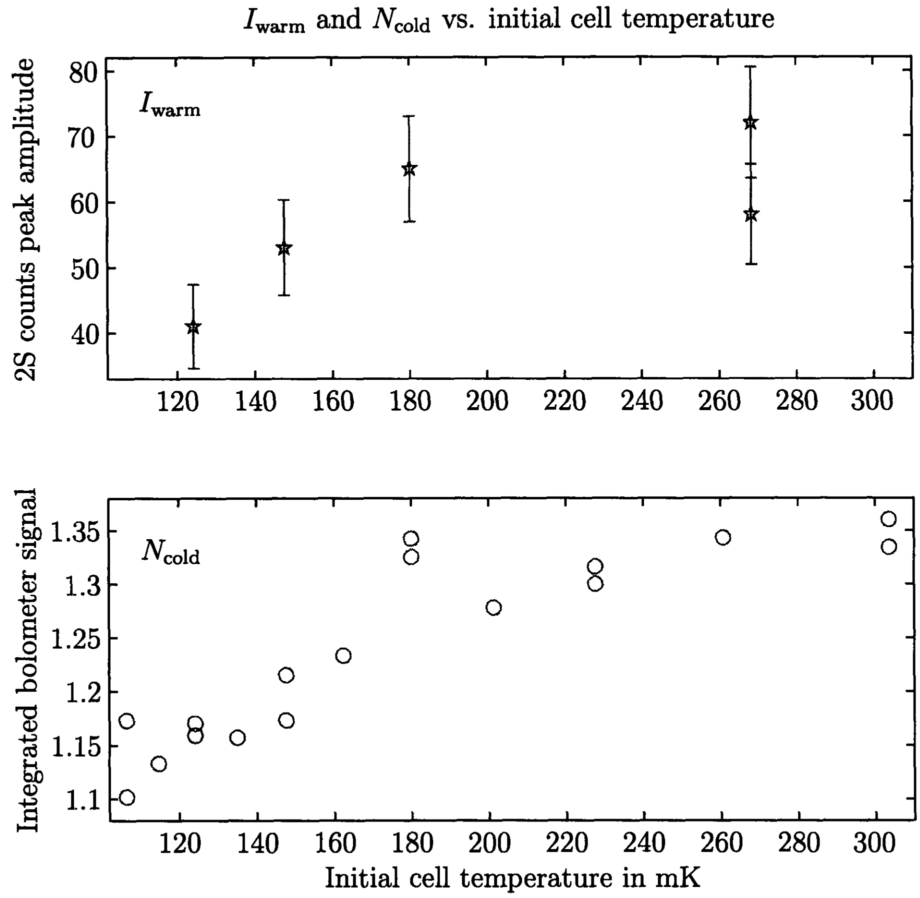

Figure 4-6: I_{warm} and N_{cold} as a function of the initial cell temperature. I_{warm} and N_{cold} are well correlated.

I_{warm} and N_{cold} exhibit the same behavior. This indicates that a colder cell temperature immediately depletes atoms from the trapping region by the increased probability of sticking and recombining on the helium-coated cell walls.

The initial (trap-loading) cell temperature is different from the cell temperature referred to above, in the discharge power Section 4.2.3. The initial cell temperature is controlled by the cell heaters at the top and bottom of the liquid helium jacket. If the cell is heated by these heaters, it cools much faster than if it is heated indirectly by the discharge. This is because the discharge is a mass of copper, with a high heat capacity. The cell can be heated without heating the discharge, but the reverse is not true. Cooling the discharge takes longer than cooling the cell.

4.2.6 Radial (quadrupole) magnetic field

The data in Fig. 4-7 show the dependence of I_{warm} on the linear radial trapping field of the quadrupole magnet. From this data we can see that the warm sample $1S-2S$ signal is mainly due to magnetically trapped atoms. If there is no quadrupole field, I_{warm} is almost too small to detect.

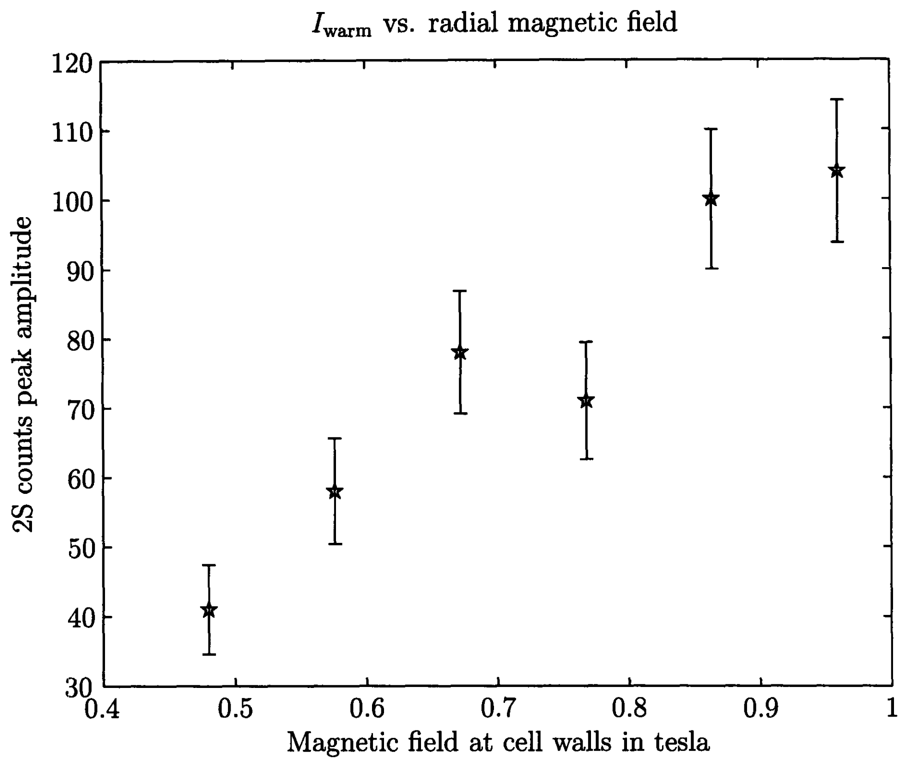

Figure 4-7: $I_{\rm warm}$ as a function of radial magnetic field

The radial density of low-field-seeking atoms in the cell can be written

$$n(\rho) = n_0 \exp(-U(\rho)/k_B T) \tag{4.5}$$

where n_0 is the peak density at the center of the trap and $U(\rho) = \alpha\rho$ is the linear radial potential created by the quadrupole magnet. If we assume the total number of atoms $N = 2\pi L \int_0^{\rm wall} n(\rho)\rho\, \mathrm{d}\rho$ (L is the length of the sample) and the temperature remain constant, we find the following expression for the peak density:

$$n_0 = \frac{N}{2\pi L \rho_{\rm wall}^2} \frac{\eta^2}{1 - \exp(-\eta)(\eta + 1)} \tag{4.6}$$

where η is the ratio of the potential at the cell walls to the sample temperature $\alpha\rho_{\rm wall}/k_B T$. The sample temperature is that of the cell, 300 mK. The radial potential is 620 mK at maximum cell radius and quadrupole current. Going from $\eta = 2$ (maximum quadrupole field) to $\eta = 1$ would decrease n_0 by a factor of almost 2, which is what we see in Fig. 4-7. If the quadrupoles were ramped down to zero, the peak density would decrease by a factor of more than 3, and the $1S-2S$ signal with it. With such low signal amplitude, it is very difficult to detect variations. This means that the warm sample $1S - 2S$ detection is mainly useful when studying trapped low-field-seekers.

4.2.7 What can be learned from warm sample $1S-2S$ detection?

$1S-2S$ detection of warm hydrogen helps reveal the optimal trap loading parameters in terms of discharge power, duration, cell loading temperature and initial magnetic fields.

Although the $1S-2S$ detection of warm hydrogen provides insights into the reasons certain parameter values are optimal for trap loading (in particular the discharge power), we cannot use it to observe a purely untrapped hydrogen sample, or to discover how to go from an untrapped sample to a trapped one.

It is not trivial to find the $1S-2S$ line. The natural linewidth is far smaller than the laser linewidth of 1 kHz. The laser is offset locked to a Fabri-Perot reference cavity line. Even with large samples of hydrogen, it is often a lengthy process to find the correct offset frequency, because it is necessary to search up to 10 MHz for a line a few kHz wide.

For deuterium, the search process would be even more difficult. We use tellurium spectroscopy at 486 nm as an absolute frequency reference. The closest saturated absorption tellurium feature is the $g1$ line, but only the frequency of the $b1$ has been measured precisely by Gillaspy and Sansonetti [32], and it is a daunting 4.245 GHz away from the deuterium $1S-2S$ transition frequency at 486 nm. The tellurium spectrum shifts from oven to oven due to pressure differences, and we cannot be certain of the comparison of our oven to that used by Gillaspy and Sansonetti. $1S-2S$ spectroscopy of deuterium would require scanning 50-100 MHz, a very lengthy process. $1S-2S$ spectroscopy could only produce results if there were a large enough density of deuterium in the trap. Without the guarantee that we have a significant trapped deuterium population, there is no reason to believe that we could detect a $1S-2S$ signal, if even the laser were at the correct frequency.

4.3 Time-Resolved Studies of Discharge Pulses

4.3.1 Interest in time-resolved study of individual discharge pulses

We can use the bolometer (see Section 2.6) to understand the behavior of the atoms immediately after they are emitted by a single discharge pulse into the cell. After each discharge pulse, the atoms expand into the cell and interact with the helium-coated walls and the magnetic field. Whether or not a significant number of atoms becomes trapped depends entirely on this interaction. Some of the atoms from the discharge pulse reach the cell bottom, and their recombination energy can be detected on the bolometer as a time-resolved recombination intensity profile.

We attempt to infer the effect of the different magnetic fields on the atoms emitted from the discharge from the arrival time profiles of the atoms onto the bolometer. Unfortunately, due to the temperature sensitivity of the bolometer (see Section 2.6.3), we cannot vary the temperature of the cell over a wide range, and thus cannot study the temperature dependence of the signal. However, the very failure to detect recombination on the bolometer is an indication of a change in temperature regime (going to a shorter surface residence and longer recombination time, which are usually better for trap loading).

This method of detection is more relevant to deuterium than the warm sample $1S-2S$ detection previously described, because it allows us to investigate the atoms during the crucial stage between discharge emission and trapping.

Since we know that we can load hydrogen into our trap, we first investigate hydrogen discharge pulses.

4.3.2 Method and geometry of bolometer discharge pulse detection

The experimental technique for detecting atom arrival time profiles from individual discharge pulses on the bolometer is described below.

Time-resolved bolometric detection

The bolometer signal is a voltage proportional to the energy deposited on the bolometer's quartz substrate surface, recorded on a digitizer. We record the bolometer signal while the discharge is pulsed on and off. The discharge pulse itself can be seen on the bolometer as a square pulse (due to rf pickup of the bolometer's electronics). The subsequent signal shows the arrival time profile and recombination of atoms from the discharge pulse at the location of the bolometer.

It should be noted that the bolometer does not distinguish between different kinds of energy deposited on the crystal. When detecting the gas mixture from individual discharge pulses, one should keep in mind that the bolometer is sensitive to the overall cell heating from the discharge pulse, impact energy (for instance from helium atoms) and quenching of excited helium, hydrogen or deuterium on its surface as well as hydrogen or deuterium recombination.

Temperature considerations, differences between hydrogen and deuterium

The regime for effective use of the bolometer is dramatically different from the trap loading regime: the bolometer requires cell temperatures below 100 mK to function (as shown in Fig. 2-6), and the trap loading process requires cell temperatures above 100 mK to trap atoms (see Sections 2.3.3 and 4.2.5 and Fig. 4-6).

John Doyle [22] explained that the reason for the temperature sensitivity of the bolometer to hydrogen recombination has to do with the surface recombination rate as a function of temperature, as explained in Chapter 2. Efficient surface recombination happens when the hydrogen's surface residence time is on the same order of magnitude as, or longer than, its recombination time. The residence time of deuterium on helium surfaces is much longer, due to its larger helium surface binding energy, as can be seen in Fig. 4-3. We thus expect the temperature sensitivity of the bolometer to be different for hydrogen and deuterium.

Detection geometry

The discharge is at the top of the cell, and the bolometer is at the bottom. The atoms travel 66 cm from the discharge to the bolometer down a cell 4 cm wide in diameter (see Fig. 2-1 for a schematic, and Fig. 2-5 for a dimensionally correct drawing).

As described in Section 2.6.4, the bolometer is fairly sensitive to the location of the recombination. We can thus assume that any signal we detect comes mostly from recombination close at the bottom of the cell, below the lower pinch magnet. This allows us to analyze the bolometer arrival time profiles as coming mainly from atoms arriving and recombining at the bottom of the cell.

4.3.3 Discharge pulse profiles dependence on magnetic fields

By varying the magnetic fields in the cell, we modify the potentials seen by the four different hyperfine states of hydrogen ($|d\rangle, |c\rangle, |b\rangle$ and $|a\rangle$) shown in Fig. 2-4, or the six different hyperfine states of deuterium ($|\alpha\rangle, |\beta\rangle, |\gamma\rangle, |\delta\rangle, |\epsilon\rangle$ and $|\zeta\rangle$) shown in Fig. 4-1.

At magnetic fields above 500 G, the different hyperfine states separate into two categories: low-field-seeking (trapped in our magnetic field minimum trap), and high-field-seeking (anti-trapped). The trapped states are the highest energy stretched states $|d\rangle$ and $|\zeta\rangle$: although initially all low-field seekers are trapped, the other eigenstates are soon lost from the trap through spin-exchange collisions with other trapped atoms as described for hydrogen by Stoof, Koelman and Verhaar [104] and for deuterium by Koelman, Stoof, Verhaar and Walraven [59].

If a bolometer signal is seen to change with magnetic field, it could be due not only to spin-polarized hydrogen or deuterium, but also to doubly electron spin-polarized metastable helium produced by the discharge.

The effects of the three large magnet systems on the low- and high- field seekers are described briefly below. We do not include the source magnet in this description, although it is our largest magnet. The 4 tesla magnetic field from the source magnet is located at the discharge, above the cell, and is very well compensated below the discharge (eg does not have a long fringe field).

Effect of the quadrupole magnet (radial field)

The quadrupole magnet provides a linear radial field, zero at the center of the cell, and up to 9600 G at the cell walls. Low-field seekers will be protected from the walls by the quadrupole magnet potential whereas high-field seekers will be pushed towards the walls. Once the atoms are on the helium walls, the low-field seekers will sometimes bounce off and come back into the trap volume, whereas high-field seekers will be quickly stuck back onto the walls.

Effect of the upper and lower pinch Magnets (axial field)

The upper and lower pinch magnet coils provide two high magnetic field regions along the cell axis (z axis), one above the trap, one below, of roughly 8300 G each. These fields can be seen in Fig. 2-5. These fields cause the low-field-seeking atoms to be vertically confined in the trap region, and the high-field-seeking atoms to be pulled either up or down out of the trapping region.

Effect of the loading magnet (cell bottom field)

The loading Magnet coil creates a strong magnetic field in the cell bottom region of roughly 8300 G. This is to prevent low-field-seeking atoms from arriving and accumulating in the region below the lower pinch field, where they would be lost to the cell bottom surface. The loading magnet field attracts high-field-seekers and repels low-field-seekers at the cell bottom, where the bolometer is located.

When both the pinches and the loading magnet are raised, their fields add to almost 9800 G at the cell bottom.

4.4 Hydrogen Discharge Pulse Profile Time-Resolved Studies

The following section describes bolometer data taken with a hydrogen discharge.

In these data, the discharge pulse itself can be seen as a vertical rectangular feature (due to rf pickup by the bolometer electronics). The discharge pulses are 15 ms long, spaced 1 second apart, and the cell temperature is kept at 90 mK. The discharge power is 3 dBm, amplified through a 50 dB 50 W amplifier. From the data shown in Section 4.2.5, it clear that the 90 mK cell temperature is far too cold for efficient trap loading, although it is possible to create a small trapped population. Normally, we run the discharge at 3 dBm for 8 seconds, at 50 Hz, with pulses 1 ms long. The total on-time of the discharge tends to be the important quantity for trapping hydrogen, eg the frequency can be lowered if the duty-cycle is lengthened.

4.4.1 Loading magnet low: detecting (mostly) low-field-seekers

Hydrogen discharge pulses and subsequent arrival time profiles are shown in Fig. 4-8. In this figure, the loading magnet is low and other magnetic fields in the cell volume are changed.

Plot (a): increasing the quadrupole field

The effect of increasing the quadrupole field alone in the cell is clear: the pulse of atoms arriving on the bolometer is increased dramatically. This is because the low-field seekers are protected from the cell walls, and are in effect funnelled towards the bolometer. Since at 90 mK the cell walls are already very sticky, protecting one half of atoms while attracting the other half to the walls yields an overall gain in signal.

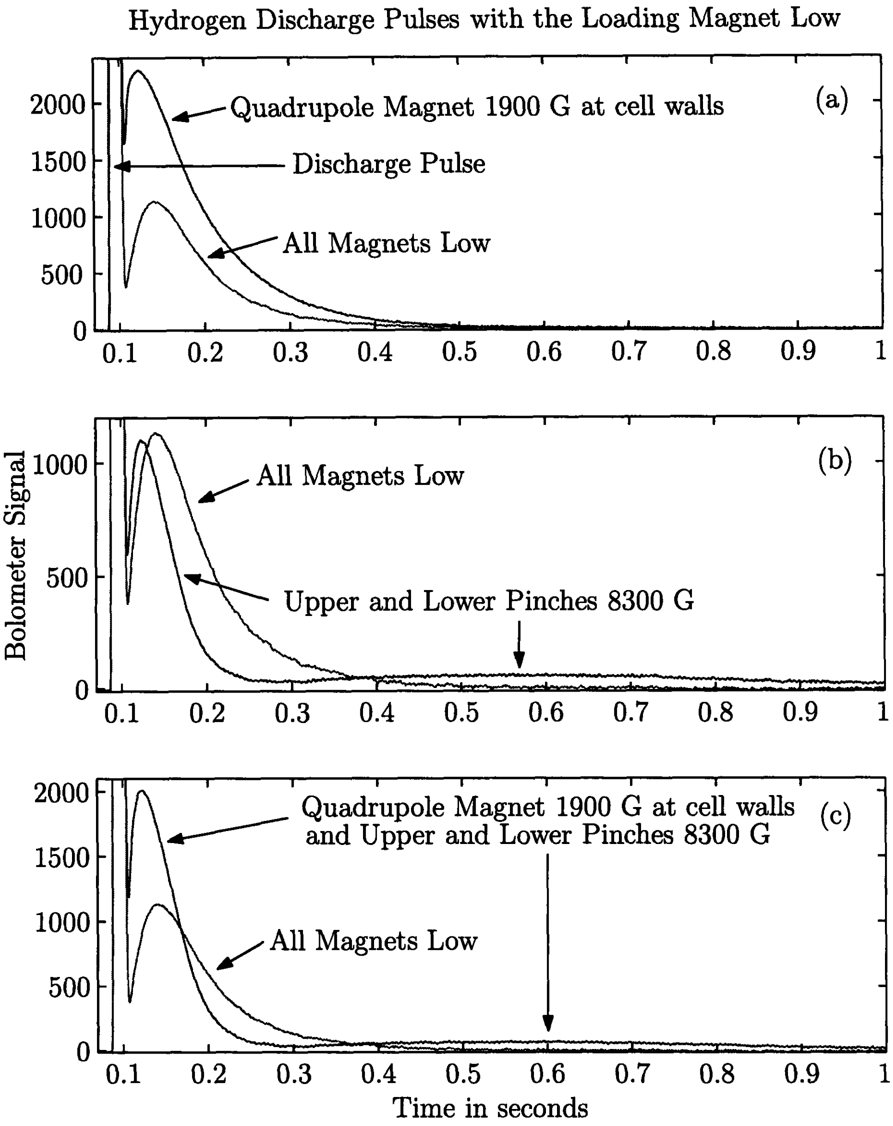

Figure 4-8: Hydrogen discharge pulses and subsequent recombination profiles as a function of cell magnetic field, with a low field at the bolometer. In this case, the bolometer detects mostly low field seekers. The most prominent features are the large increase in fast arrival time signal when the quadrupole is raised (plot (a)) and the smaller, slower signal in the presence of the pinch fields (plots (b) and (c)).

Plot (b): increasing the pinch fields

Increasing the upper and lower pinches alone speeds up and decreases the first arrival peak, and also creates a second, slower feature. The high energy high-field-seeking atoms will tend to be accelerated by the two potential wells of the pinch magnets, whereas the low-field seeking-atoms will be slowed down, and some trapped between the two high field regions. However, since they are radially exposed to the cell walls, they eventually all stick on the walls and recombine to molecular hydrogen. A small part of this hydrogen recombination energy will be deposited on bolometer (not very efficiently, since the recombination itself is happening in the middle of the cell rather than at the bottom). This is the likely source of the second smaller, slower feature.

Plot (c): increasing both the quadrupole and the pinch fields

Increasing both the pinch fields and the quadrupole field speeds up and increases the first arrival peak. The second feature apparent with the pinch magnets alone is also seen. In this case, we are most likely detecting primarily low-field-seeking atoms, protected from the cell walls by the quadrupole. However, some of these (the slower ones) are confined between the pinch magnets. Since the quadrupole magnet field at the cell walls is only 1800 G, or 120 mK for spin-polarized hydrogen, most of the hydrogen again ends up on stuck on the walls, and the slow second feature can be attributed to its recombination energy.

4.4.2 Loading magnet high: detecting (mostly) high-field-seekers

We can perform the same experiments with a high field at the location of the bolometer (bottom of the cell). These data are shown in Fig. 4-9.

When only the loading magnet is high (no trapping fields in the cell), the discharge pulse signal has two features, one fast and one much slower. The fast feature is accelerated compared to the one with no magnetic fields at all seen in Fig. 4-8 (all plots), and a bit smaller in amplitude, and much shorter in duration.

When the loading magnet is raised, we detect mostly high-field-seekers at the bolometer, and these are accelerated by the potential of the loading magnet. The low-field seekers are confined vertically between the 4 Tesla source magnet at the discharge and the 8300 G loading magnet at the cell bottom. These untrapped low-field-seekers stick and recombine on the cell walls, and the bolometer picks up this recombination energy, more efficiently than when the pinches were high, and the loading magnet low (see plot(b) of Fig. 4-8) since the recombination is closer to the bolometer itself.

Plot (a): increasing the quadrupole field.

When we raise only the quadrupole magnet, we create a defective trap, since the quadrupole field does not extend to the loading magnet. The fast feature becomes larger, and the slow feature smaller. The quadrupole field ensures that the majority

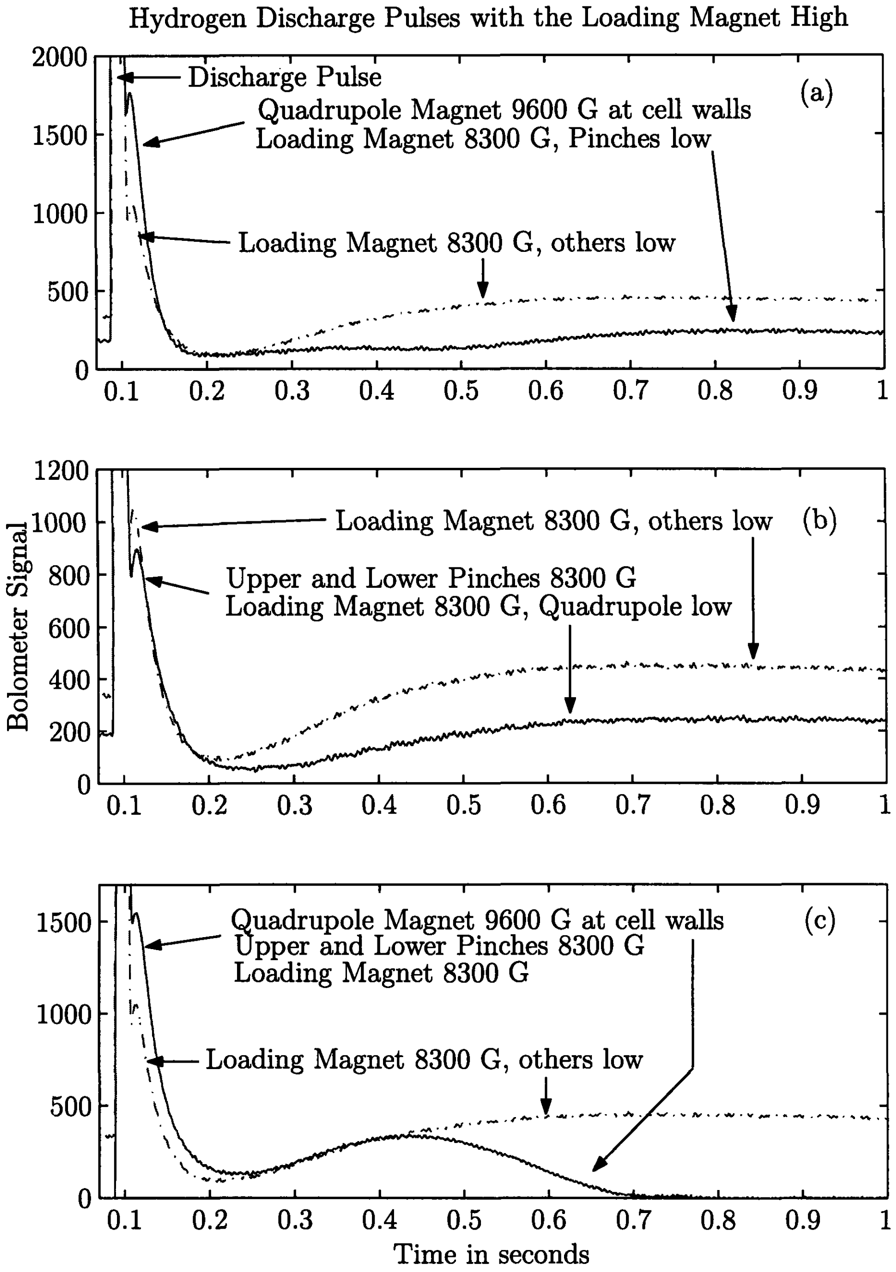

Figure 4-9: Hydrogen discharge pulses and subsequent recombination profiles as a function of cell magnetic field, with a high field at the bolometer. The most prominent features are the increase in the fast signal when the quadrupole is raised (plot (a)) and the shortening of the slow feature when both the pinches and the quadrupole fields are raised (plot (c)).

of the high-field-seekers are attracted to the sticky helium walls, and the low-field-seekers are the only ones that can reach the cell bottom. The most energetic of these pass into the loading magnet region, and are detected on the bolometer. The less energetic are partially trapped, and slowly decay as they find the trap defect (where the quadrupole field ceases).

It is useful to note that if the quadrupole magnet is raised to its maximum, but the loading magnet is low, the fast signal from the funneled low-field-seekers is so large it exceeds the range of the bolometer. However, when the loading magnet is raised, the fast signal is much smaller. Thus the loading magnet field is clearly repelling most low-field-seeking atoms.

Plot (b): increasing the pinch fields

When we raise only the pinch magnets, the fast feature becomes slightly smaller and the slow feature becomes much smaller. The recombination of the low-field-seekers on the cell walls is further removed from the bolometer, and not detected as well. As can be expected, the signals are overall very similar.

Plot (c): increasing both the quadrupole and the pinch fields

When we raise both the quadrupole and the pinch magnets, the fast feature becomes larger, and the slow feature is roughly the same height, but stops earlier. As before, the quadrupole protects the low-field-seekers from the cell walls, but the larger potential barrier caused by both the lower pinch and loading magnets prevents more of them from reaching the cell bottom. The trap is complete, with no zero field regions. The low energy low-field-seekers are trapped.

4.4.3 Possible sources of the slow discharge pulse arrival time signal

There are three loss processes that could explain the slower feature: evaporation, $|c\rangle$ state atom decay and $|d\rangle$ state atom decay.

The loss of $|c\rangle$ and $|d\rangle$ states is mainly through $c-c$ and $d-d$ dipolar decay. The rate constants g_c and g_d calculated by Stoof et al. [104] differ by two orders of magnitude at low magnetic fields (below 0.1 Tesla). Since this data is taken at suboptimal conditions for trap loading (cell too cold, single 7.5 ms discharge pulse), we expect the peak density of trapped atoms to be quite low, below 10^{12} cm^{-3}. At such low densities, the decay timescale for $|d\rangle$ state atoms is almost 1/2 hour, and the decay timescale for $|c\rangle$ state atoms is on the order of 10 seconds.

Thus the slower feature is probably due to initial evaporation from the trapped sample. The evaporation is from the sample to the cell walls. Since the walls are cold and sticky, the higher energy atoms of the trapped sample are removed by wall contact. As they are removed, the sample cools to a temperature below that of cell walls. This type of evaporation slows as fewer atoms are energetic enough to reach the walls, and no more signal is detected on the bolometer. For a 90 mK sample and cell temperature, in a 620 mK deep trap, the residence time and recombination time are roughly equal for a sample peak density of 10^{12} cm^{-3}, on the order of a fraction of a millisecond. Thus during that time, an atom on the liquid helium surface is almost equally likely to recombine or bounce off. This timescale is comparable to that of thermalization in the bulk gas. This timescale controls the sample thermalization. These timescales make it likely that in the first 0.3 seconds, a significant fraction of the high energy atoms in a trapped 90 mK sample at a peak density of 10^{12} cm^{-3} will recombine on the wall while the rest of the trapped sample cools.

We can thus differentiate a trapped from an untrapped sample by examining the properties of the slower discharge pulse feature. An untrapped sample has a long slow feature, as all atoms eventually recombine on the cell walls. A trapped sample has a slow feature that ends more rapidly, which is most likely due to initial evaporation to the cell walls.

4.4.4 Time-of-flight analysis of discharge pulse profiles

The arrival time profile of hydrogen atoms emitted by the discharge at the bolometer is due to the combination of several processes. A detailed model of the interaction of these processes would be computationally intense. However we can look at each process individually and gain some understanding of the ingredients of the arrival time profiles.

Maxwell-Boltzmann time-of-flight

If the cell were not a closed tube with semi-sticky walls, but an open space with a detector (the bolometer) placed a distance L away from the aperture of the emitter (the discharge), the arrival time profile should be that of a Maxwell-Boltzmann gas at a temperature T.

A gas at temperature T emitted through an aperture has speed probability distribution $P(v)\mathrm{d}v \propto v^3 \exp(-mv^2/2k_BT)\mathrm{d}v$ [57]. This can easily be transformed into an arrival time probability distribution function $P(t)\mathrm{d}t \propto t^{-5} \exp(-mL^2/2t^2k_BT)\mathrm{d}t$ where L is the distance of the detector from the aperture.

We can compare the discharge pulse profiles to such an arrival time profile by making several assumptions: first that the temperature of the gas is that of the cell, second that the discharge emits a constant flux of atoms. We know that both of these assumptions are weak: the atoms emitted from the discharge are most likely initially at a much higher temperature than the cell, but thermalize through bulk gas and surface collisions within the first few centimeters of expansion into the cell. Moreover the discharge operation is not uniform, it has a finite turn-on time and exhibits variations on the fraction of a millisecond timescale.

The only atoms to arrive at the bolometer by direct time of flight are those emitted from the discharge region into a very small solid angle: approximately 4×10^{-4} of the total. All the other atoms will have at least one and most likely many more wall collisions. At each such collision, they risk sticking on the wall with a sticking probability on the order of 10%. If they stick, they may recombine with

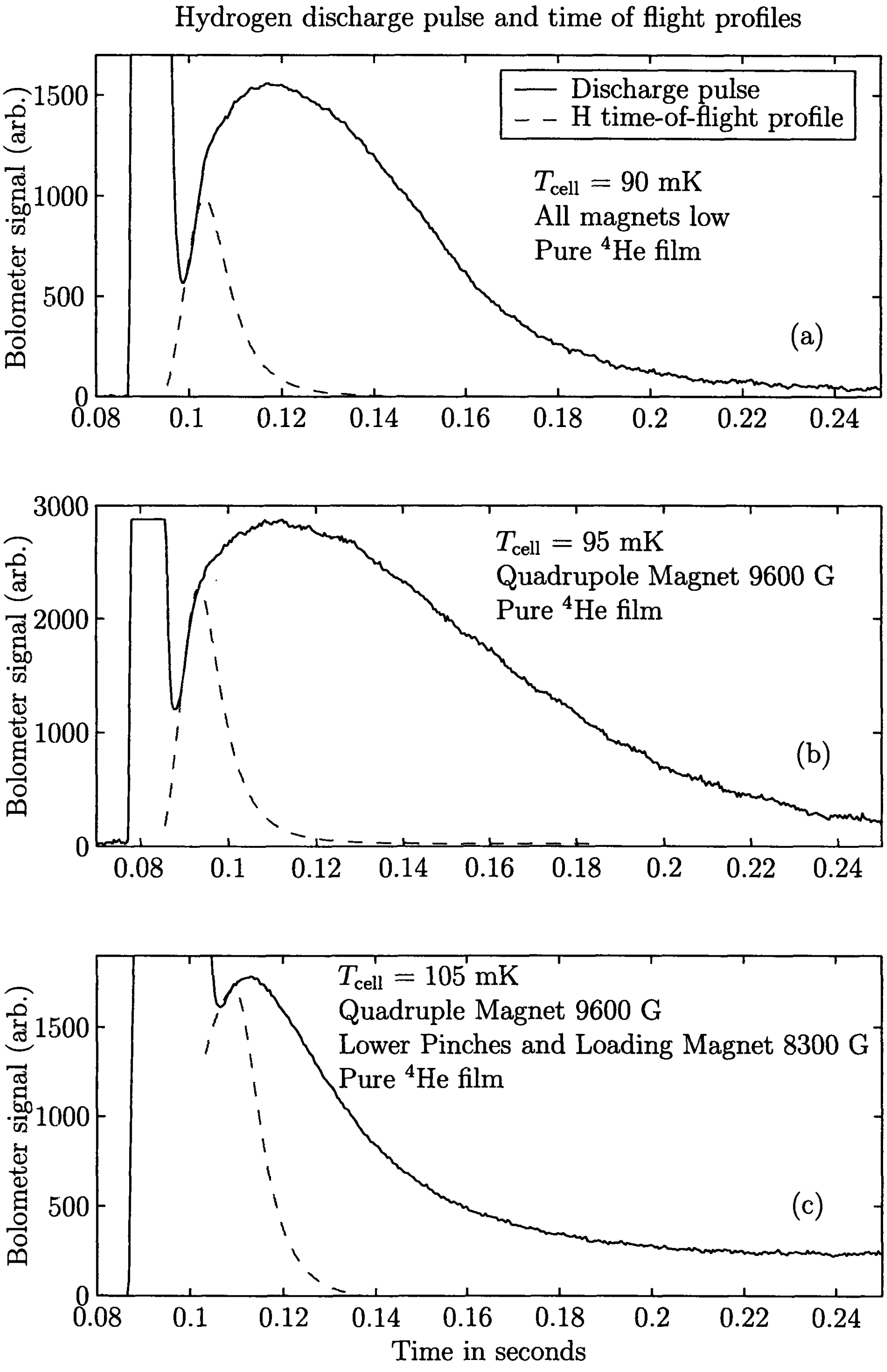

Figure 4-10: Hydrogen discharge pulses and time-of flight profiles. Since only 4×10^{-4} of the atoms are expected to reach the bolometer without wall collisions, it is not surprising that the time-of-flight curves at most fit the early part of the discharge pulse profiles. All the other atoms have wall collisions, with a the possibility of sticking on the surface and being later re-emitted into the cell at the temperature of the cell surface, which would explain the long delay.

other hydrogen atoms, or be re-emitted into the cell volume after a delay of τ_{res} (Eq. 2.4) in random direction, and with an average energy of the cell wall temperature. Such processes will tend to deplete and delay the atoms.

The only free parameter in the time-of-flight distribution is the amplitude. Fig. 4-10 shows discharge pulse profiles with hydrogen time-of-flight curves at the cell temperature, matched in amplitude to the early part of the discharge curve. Since only 4×10^{-4} of the atoms are expected to reach the bolometer without wall collisions, it is not surprising that the time-of-flight curves at most fit the early part of the discharge pulse profiles.

Gas puff expanding into closed cell

As the cell is in fact a closed tube, another way to picture the discharge pulse is the expansion of a puff of hydrogen gas into the cell volume. In this picture, the detector should see an initial buildup, and then a steady flux of hydrogen. However, this picture ignores the recombination losses on the cell walls.

Recombination loss onset

After the initial expansion into the cell, the density of hydrogen builds up in the bulk and on the cell walls. When the surface density is large enough, the recombination time τ_{rec} becomes shorter than the surface dwell time τ_{res}, and recombination depletes the hydrogen in the cell. We can interpret the timescale of the decay of the discharge pulses as being due to surface recombination losses, at least for the first two plots of Fig. 4-10 (all magnets low, and only quadrupole high respectively). The quadrupole magnet field decreases the density of low-field-seekers at the cell walls, consistent with a longer discharge pulse decay time.

In plot (c) of Fig. 4-10, where all trapping magnets and the loading magnet are high, the rapid decay time is not due to higher surface density and faster recombination, but to the trapping magnets preventing the lower energy low-field-seeking atoms from reaching the bolometer.

4.4.5 Interpretations of the time-resolved discharge pulse profile data

Although we are not able to conclusively verify what causes the changes in the discharge pulse profiles, we can nevertheless form a consistent picture from the changes caused by varying the magnetic field in the cell. In this way, we can qualitatively understand what is happening to the atoms in the cell by detecting those that arrive at the bottom of the cell. We also have a signature of a trapped sample as opposed to an untrapped sample.

4.4.6 Effect of introducing ^{3}He in the cell

In order to trap deuterium, we have to overcome the challenge of the high binding energy of deuterium on ^{4}He cell walls. Hydrogen has a lower binding energy on ^{3}He than on ^{4}He, and it is expected that the deuterium binding energy is also lowered on ^{3}He. We investigated the effect of adding ^{3}He on the hydrogen discharge pulse profiles and trapped samples. Issues involving the presence of ^{3}He in the cell are discussed in Section 2.6.6.

The binding energy of hydrogen on a ^{4}He surface is 1.11(1) K (see table 4.2). The addition of ^{3}He decreases the binding energy to 0.38 K for a ^{3}He surface density of 6×10^{14} cm^{-2}, as determined by Safonov et al. [95].

We added approximately 1.2×10^{20} ^{3}He atoms to the cell, roughly 15% of the ^{4}He, corresponding to a surface density of 1.8×10^{17} cm^{-2} (assuming all the ^{3}He is on the cell walls) well into the low binding energy regime. The cell volume density of gaseous ^{3}He is determined by the cell temperature. Below 100 mK, the volume density above a saturated film is smaller than 3×10^5 cm^{-3}, dropping precipitously with temperature (see Fig. 4-2). At 300 mK, the volume density above a saturated film is closer to 7×10^{15}, larger than our largest trapped hydrogen densities. In such a regime, it would be impossible to trap hydrogen. Thus loading a hydrogen trap with ^{3}He in the cell require a lower cell temperatures, where the ^{3}He density is not prohibitively large.

It is possible to trap hydrogen with this quantity of ^{3}He in the cell, although the trap loads and reproducibility are not as good as with pure ^{4}He. It is moreover possible to trap hydrogen with no external cell heating, which would normally result in significant losses (see Section 4.2.5 and Fig. 4-6). The ability to trap hydrogen without cell heating is an indication that the lower binding energy of the helium film allows a lower trap loading temperature.

By keeping the cell close to 70 mK, we can even do bolometer hydrogen discharge pulse studies similar to those described above, with a few complications. The signal changes with magnetic field are similar, but the bolometer is much more challenging to work with.

The ^{3}He in the cell slows the bolometer response, and decreases the hydrogen signal. This is because of the reduced hydrogen binding energy on the helium surface: the surface recombination rate and the surface residence time decrease. Any increase in temperature drastically reduces the bolometer's hydrogen recombination sensitivity (as described in Section 2.6.3 and shown in Fig. 4-3).

Larger discharge pulses not only raise the cell temperature beyond what the bolometer can tolerate, but also have a chance of destroying the helium film on the cell walls. The presence of ^{3}He weakens the superfluidity of the ^{4}He film, and a discharge pulse that is too long or too powerful can disrupt it. This can be seen in Fig. 2-2, Section 2.3.2.

4.5 Deuterium Discharge Pulse Profile Time-Resolved Studies

Having developed diagnostic tools for a hydrogen discharge and the arrival time profiles of the expanding gas puffs from individual discharge pulses, we attempted to do similar analysis with a deuterium discharge.

We first seek to understand the behavior of deuterium discharge pulse profiles in a ^{4}He-coated cell.

4.5.1 Starting the deuterium discharge

The cryogenic deuterium discharge is more difficult to start than the hydrogen one. Normally we can start the hydrogen discharge at temperatures below 1 K, but with deuterium it is necessary to heat the discharge to 1.75 K. The effect of this is to increase the (helium) vapor pressure in the discharge. The power required to start the discharge is very high: 14 dBm on the frequency synthesizer compared to 3 dBm usually (the normal hydrogen discharge rf peak power after amplification is 10-30 watts).

4.5.2 Magnetic field and cell temperature dependence of discharge pulse signals

We first saw deuterium from discharge pulses arriving at the bolometer when running the discharge at high powers and for long intervals (amplified 10 dBm and 75 ms long pulses, compared to amplified 3dBm and 1 ms long pulses for hydrogen). We could distinguish deuterium from other signals, such as cell heating by the discharge, by its magnetic field dependence, similar to that of hydrogen. Large discharge pulses heat the cell, but in fact it is only when the cell is quite warm (above 250 mK) that the atom pulses are detected at the cell bottom, on the bolometer.

The magnetic field and temperature dependence of the discharge arrival signal are shown in Fig. 4-11. The first plot shows bolometer data when there is no magnetic field in the cell, and when the quadrupole magnet is raised to 9600 G at the cell walls. With hydrogen, the increase in signal from raising the quadrupole is very large, because the quadrupole funnels the low-field seekers to the bolometer. With deuterium, we would expect to see the same behavior. However, the first few discharge pulses, at cell temperatures below 250 mK as measured on the second plot, show almost identical signals. It is only above 250 mK, in the later discharge pulses, that an amplification of signal due to the quadrupole field can be seen. This data is taken with only ^{4}He coating the cell walls. The two bolometer signal traces are offset for visual clarity.

At lower temperatures, deuterium is not visible on the bolometer, although the discharge is working (we can either visually detect the discharge pulses, or record them on the MCP). It may be that at lower temperatures the wall recombination is so efficient that the deuterium pulse recombines almost immediately on the cell

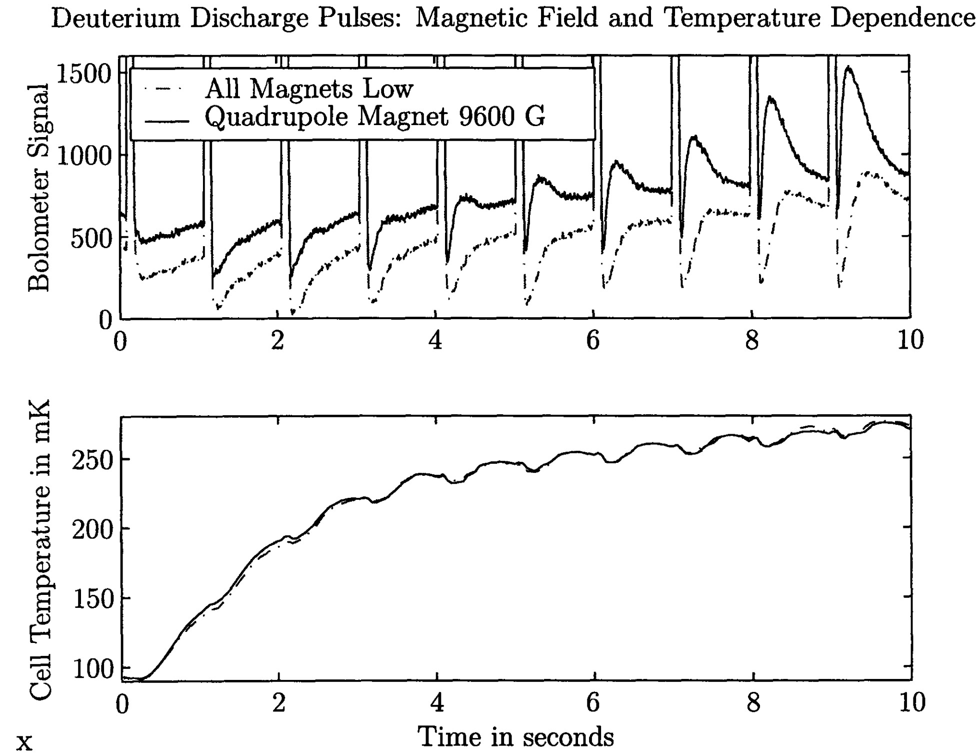

Figure 4-11: Deuterium discharge pulses with ^{4}He in the cell: Magnetic field and temperature dependence. The first plot shows the bolometer data for deuterium discharge pulses with the quadrupole field up and down (no other magnetic fields are present in the cell). The second plot shows the cell temperature progressively warming. As the discharge pulses heat the cell, deuterium recombination becomes visible on the bolometer, when the quadrupole magnet is ramped up and funnels the low-field seekers to the bolometer region. Deuterium recombination on the bolometer is only clearly visible at cell temperatures above 250 mK, when the quadrupole magnet is raised.

walls, far above the bolometer, and it is only at higher temperatures that some of the low-field-seekers protected by the quadrupole magnetic field can reach the bolometer region at the bottom of the cell.

4.5.3 Time-of-flight analysis of deuterium discharge pulses

It is possible to detect deuterium discharge pulse arrival time profiles in a ^{4}He-coated cell at temperatures below 200 mK, and for short (1 or 2 ms) pulses at 6 dBm power (amplified). However, these arrival time profiles are intermittent, only roughly 1/5 of the discharge pulses are followed by a deuterium recombination profile. The deuterium profiles, when present, are quite reproducible. The reason for this all-or-nothing behavior of the deuterium discharge in the ^{4}He-coated cell is not know. The discharge pulses with no deuterium profiles are simply followed by flat signals, not dropouts that could indicate a tear in the helium film (such as shown in Fig. 2-2).

The deuterium discharge pulses shown in Fig. 4-12 are much better approximated by time-of-flight profiles at the corresponding cell temperatures than the hydrogen discharge pulses of Fig. 4-10. The discharge pulse overall changes as expected with cell temperature (slower with lower temperature). However, it seems that with deuterium, we may be seeing mostly the 4×10^-4 of the atoms emitted directly to the cell bottom, and the vast majority of the others are adsorbed on the walls above the bolometer (as opposed to the hydrogen pulses of Fig. 4-10 , where the large majority of the slower signal is unaccounted for by the time-of-flight distribution). Since these data are taken at low temperatures in a ^{4}He coated cell, it is not surprising that most deuterium atoms with one or more wall collisions stay stuck and recombine on surfaces far above the bolometer.

4.5.4 Effect of introducing ^{3}He in the cell

After adding ^{3}He to the cell, the behavior of the deuterium discharge and discharge pulse arrivals at the bolometer changes dramatically, and we see magnetic field dependence behavior similar to that of hydrogen in a ^{4}He cell.

Unfortunately, because it is not possible to thoroughly pump out all the ^{3}He from the cell without heating the cell above 4 K (see Section 2.6.6), in this case we do not know exactly how much ^{3}He was in the cell, although it is probably between 5 % and 20 % of the amount of ^{4}He, well into the regime of high ^{3}He surface density necessary for lowering the surface binding energy [95].

The presence of ^{3}He makes it possible to detect deuterium recombination on the bolometer at lower temperatures than with ^{4}He alone. This is consistent with ^{3}He lowering the binding energy, and hence increasing the ratio of the recombination to residence times on the helium film.

Deuterium discharge pulses in a ^{3}He coated cell are shown in Fig. 4-13 with hydrogen discharge pulses in a ^{4}He coated cell as comparison. The hydrogen data is taken with the discharge frequency generator at 3 dBm, pulsed on for 15 ms and at a cell temperature of 90 mK. The deuterium data is taken with the discharge also running at 3 dBm, for 30 ms, and at a cell temperature between 70 and 115 mK. The

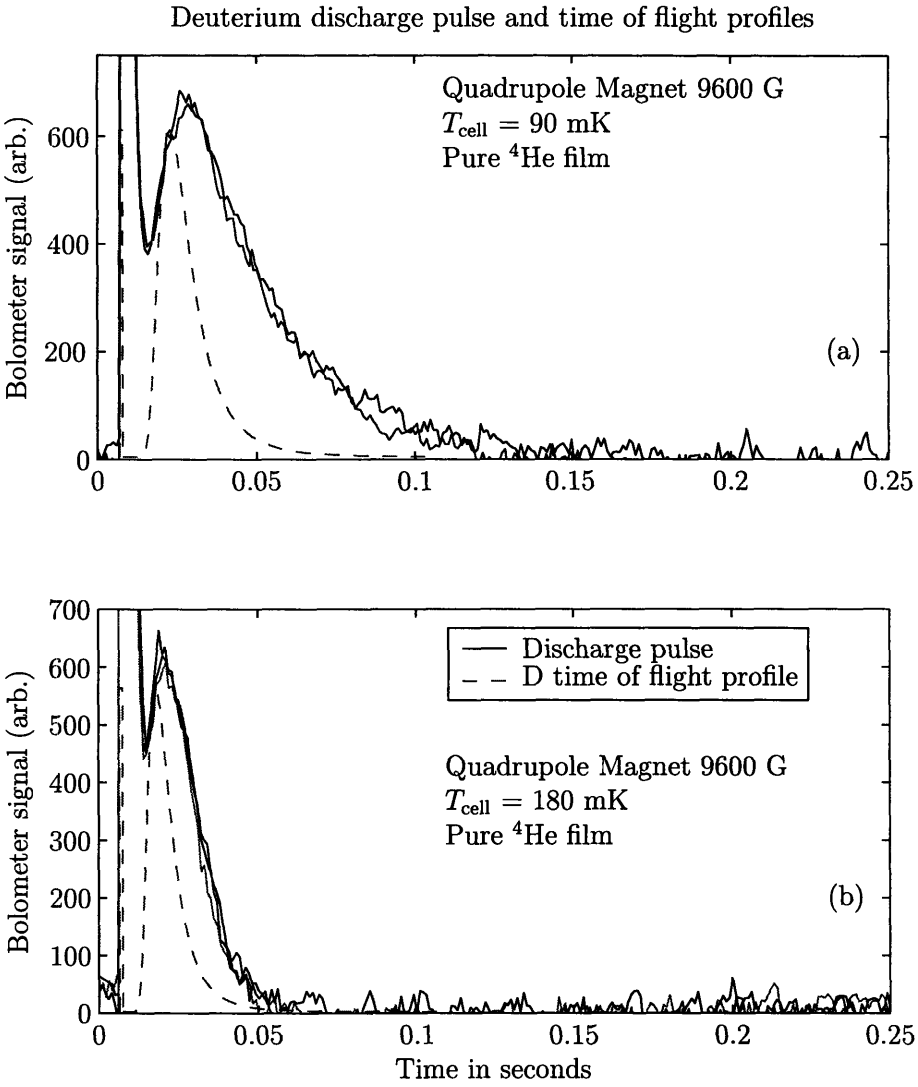

Figure 4-12: Deuterium discharge pulses and time-of-flight profiles at 90 and 180 mK in a ^{4}He-coated cell. The time-of-flight curves are better correlated to the deuterium discharge pulses than to the hydrogen (shown in Fig. 4-10), indicating more losses on the cell walls. The discharge pulses shown here are intermittent: within the same discharge pulse sequence, approximately 80 % will show no arrival time profile. However, when the arrival times are present, they are quite reproducible in overall shape.

discharge power is as usual amplified through a 50 dB 50 W amplifier. The deuterium data also is less reproducible than the hydrogen, due to helium film fragility (shown in Fig. 2-2). The data are scaled such that the discharge pulses with magnets low are of the same height. However, the deuterium data is taken with the bolometer at a higher set resistance, so the bolometer is sensitive to smaller signals. This makes the bolometer signal more noisy and vulnerable to overshoots and drifts (hence the negative drift after the fast signal component in each plot).

Plot(a): deuterium on ^{3}He and hydrogen on ^{4}He with all magnets low

When no magnetic trapping fields are present, the hydrogen signal is longer. Because the deuterium discharge pulse is twice as long, and because of the mass difference, the deuterium signal should be delayed and last longer compared to the hydrogen signal. This is not the case: the long tail of the hydrogen signal contains atoms that had ^{4}He wall collisions and were re-emitted into the cell. Fewer deuterium atoms unstick from even ^{3}He walls, and the arrival time pulse is short.

Plot(b): deuterium on ^{3}He and hydrogen on ^{4}He with a quadrupole field

A striking difference between the hydrogen and deuterium data can be seen in plot (b) of Fig. 4-13: the impact of the quadrupole magnet. Although increasing the radial quadrupole magnet field increases the arrival time signal for both hydrogen and deuterium, the relative increase for deuterium is much smaller. By comparison, the data for the quadrupole magnet at 9600 G is not shown for hydrogen, because the signal is so large, it is beyond the bolometer's range. Thus although a strong radial field protects some high-field seeking deuterium atoms from the cell walls, it is not as effective as for hydrogen. The difference is not with the magnetic field potential (which is similar for both species at 9600 G), but with the binding energy or recombination cross length on the helium film. Even with a ^{3}He surface, the deuterium binding energy could be twice as large at the hydrogen binding energy on ^{4}He.

For this data, the ratio of hydrogen cell wall binding energy to the wall temperature is 10. For deuterium, assuming $E_b = 2$ K for deuterium on ^{3}He, it is closer to 20. Under normal trap loading conditions, the ratio of surface binding energy to wall temperature for hydrogen is 3.5. For deuterium in a ^{4}He coated cell, this would correspond to a cell wall temperature of 1 K. For deuterium in a ^{3}He coated cell, assuming the binding energy is close to 2 K, a cell wall temperature of 550 mK. The vapor pressure of ^{3}He at 550 mK is extremely large, and would not allow a trapped sample to form. Moreover, heating the cell to this temperature would require a corresponding slow time to cool down into the thermal disconnect region, and hence further atom losses.

Plot(c): deuterium on ^{3}He and hydrogen on ^{4}He with all magnets raised

In plot(c) of Fig. 4-13, we see the characteristic arrival time profile that we identify with a trapped sample for hydrogen (see Section 4.3.3 and Fig. 4-9), for hydrogen

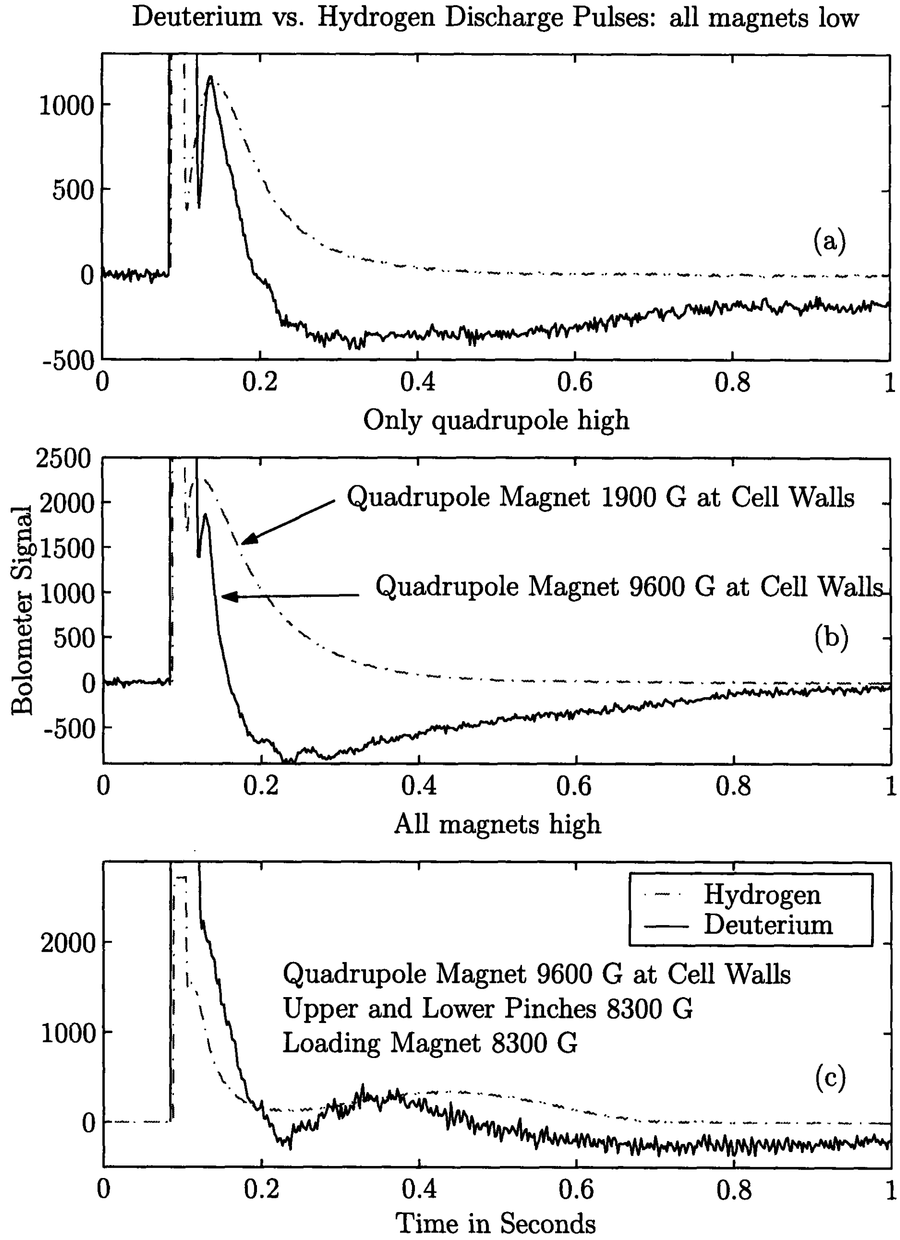

Figure 4-13: Comparison between deuterium and hydrogen discharge pulses as a function of magnetic field. The hydrogen is in a ^{4}He-coated cell, the deuterium is in a ^{3}He-coated cell. The overall behavior with magnetic field is similar: increase in fast signal height with quadrupole field in plot (b) compared to plot (a), finite duration slow feature with all magnets high in plot (c). Although the deuterium data has been scaled to match the hydrogen in plot(a), it is in fact overall smaller than the hydrogen data. Deuterium also experiences less amplification with the quadrupole field than hydrogen (note the different quadrupole values in plot (b)).

and deuterium. Both the fast and the slow feature are proportionally larger than for hydrogen (compared to plots (a) and (b)), and the slow feature peaks sooner and disappears faster than for hydrogen, but happens overall on the same timescale.

Seeing this feature as evaporation from a trapped sample to the helium wall encouraged us to attempt to detect a trapped deuterium sample after forced magnetic evaporative cooling. However, we were never able to detect a trapped sample even when varying discharge and trap loading temperature parameters.

This may be because the arrival time profile in the third plots of Figs. 4-9 and 4-13 are not in fact characteristic of trapped samples. It is also possible that because the recombination we detect from deuterium in Fig. 4-13 are overall smaller, requiring a higher set resistance as described above, the trapped sample is similarly small and cannot be ultimately detected on the bolometer. Or it may be because the large helium surface binding energy causes the deuterium surface to bulk density ratio to be very large. In this latter case, even though we can see signals due to surface recombination on the bolometer, there are not enough deuterium atoms in the trap volume to have collisions and thermalize to temperatures below the trap height, and eventually all are lost to the walls.

Whichever the case, trapping deuterium was not possible for us, even in a ^{3}He-coated cell with magnetic fields of almost 1 tesla at the cell walls.

4.6 Buffer Gas Trap Loading

John Doyle and his group at Harvard University have pioneered buffer gas cooling as an alternative to laser cooling [19, 16]. Buffer gas cooling is done by placing the atom or molecule to be trapped in a gas of dense cold ^{3}He or ^{4}He in a cell with a magnetic field minimum trap.

The atom or molecule is cooled by collisions with the cold helium gas, to a temperature below that of the trap threshold. The density of the helium gas must be such that the timescale of diffusion to the walls is much longer than the timescale of thermalization. Most atoms and molecules do not have bound surface states on liquid helium, but instead dissolve in the liquid.

Then the non-magnetic helium gas is *suddenly* removed. The timescale of the helium gas removal is crucial to successful buffer gas loading. If the helium gas is not removed quickly enough, the trapped sample decays through background gas collisions rather than evaporatively cooling from the magnetic trap.

In our experiment, although the hydrogen may experience some helium gas collisions, the atoms thermalize with the cell walls by sticking and being re-emitted into the cell and magnetic trap region. Our experiment is not designed for buffer gas loading. If we heat the cell enough to achieve high helium gas densities, we have no mechanism other than cooling the cell for removing the helium gas. Since cooling the cell takes several tens of seconds, enough time for a trapped sample to decay through background collisions, we are unable to do efficient buffer gas trap loading.

4.7 Conclusions of Deuterium Study

The set of experiments described in this chapter demonstrated the difficulty in understanding the trap loading stage of our experiment, even in the case of hydrogen which we have trapped successfully for years. Deuterium brings a new set of challenges on top of these.

Our conclusion is that it is not possible to trap deuterium with our current trap loading techniques. The large binding energy of deuterium on ^{4}He (and ^{3}He) prevent us from loading significant amounts of deuterium in the trap. It is also possible that there is another phenomenon, due to magnetic- field-dependent resonances, that increases the recombination rate on the helium surface [100, 2, 78].

Successfully trapping deuterium in a magnetic trap will most likely be done by buffer gas trap loading [39]. In this trapping loading method, deuterium would be protected from the cell walls by a gas of helium atoms, and thermalized by this gas to a temperature below that of the magnetic trap height. Then the (non-magnetic) helium gas is removed fast enough to minimize background gas losses, and a significant fraction of the deuterium gas remains in the magnetic trap. A new cryostat designed by the MIT Ultracold Hydrogen group to trap hydrogen-lithium mixtures through buffer gas loading may be the ideal instrument to finally trap deuterium.

Appendix A

BBO Doubling Crystal Surface Contamination

A.1 The BBO Doubling Crystal and its Maintenance

The (Beta-Barium Borate) BBO crystal [81] is used in the $1S - 2S$ spectroscopy laser system to double 486 nm light to 243 nm [96]. We get our BBO crystals from two companies: Cleveland Crystals (www.clevelandcrystals.com) and CASIX (www.casix.com). Cleveland Crystals has good technical support. The BBO crystal is brewster cut, to minimize internal reflection at 486 nm.

BBO is hygroscopic. We flush the crystal with nitrogen when the laser is off, and with oxygen when the 486 nm laser light is on the crystal. Without oxygen, the crystal damages and the transmission of 486 nm light decreases. The cause of this damage is not completely known. It is believed that the oxygen gas flow replenishes oxygen burned off the crystal surface. According to Kjeld Eikema from Vrije University in the Netherlands, light above 300 nm can remove oxygen atoms from the crystal surface [26]. Clearly, 243 nm is well into this regime. However, Jon Sandberg [96] reported no change in the damage process even after changing the phase matching angle (and hence the doubling efficiency).

A.2 Crystal Surface Damage and Color Centers

If oxygen gas is not flowed over the crystal during laser operation, the surface of the crystal becomes permanently damaged. A "color center" forms on the spot where the laser beam exits the crystal. A color center is a location with excess atoms with free electrons (metal atoms) which absorb optical laser light. Color centers are usually defined as occurring in alkali halogenide (eg Na-Cl) crystals [49]. The most likely scenario in the creation of a color center is that when enough oxygen is removed from the surface without being replaced, a defect in the crystal structure is created: a spot with too many barium and boron atoms. Barium and boron are both metals, and without the presence of the electronegative oxygen, their free electrons may absorb optical laser light[3].

The color center reduces the transmission of 486 nm light (and hence the efficiency of 243 nm production) dramatically, by a factor of 2 or more. This damage occurs gradually, on the timescale of hours.

In our experience, such crystal damage is both permanent and localized. It is permanent because oxygen flushing will not undo the damage (although it can prevent it from getting worse). (It should be noted that other groups have seen oxygen flushing repair BBO damage spots [26].) It is localized: translating the crystal such that the beam exits on a different spot of the crystal surface is usually sufficient to resume normal laser operation.

A.3 A New Type of Crystal Surface Damage

After years of successful operation of BBO crystals using nitrogen/oxygen flushing, our BBO crystals started suffering from a new type of surface damage. This problem appeared as a drastic decrease in the time a color center took to form (minutes instead of hours) and no visible slowing of damage with oxygen flow.

As soon as the doubling cavity was locked, with approximately 40 W of 486 nm light propagating in the cavity, the surface would start damaging and the power would rapidly decrease with or without oxygen flow. Moreover, translating the crystal did not allow us to resume normal operation. Although initially the cavity 486 nm transmission power would go up to normal levels, it would again decrease rapidly as a new damage spot formed.

Once a crystal started exhibiting this behavior, it would not stop. Even worse, changing the crystal in our system to a new one resulted in the same surface damage behavior after a few days.

This new type of crystal damage thus had three important characteristics: it prohibited the oxygen gas from preventing crystal surface damage, it affected the whole surface, and it was permanent.

A.4 Crystal Contamination Diagnosis

Colleagues in the Center for Material Science and Engineering [102] recommended that we use the CMSE Shared Experimental Facility for surface spectroscopy. After consulting with research specialist Elisabeth Shaw (elshaw@mit.edu) we used the Kratos Axis Ultra Imaging X-ray Photospectrometer to do X-ray photoelectron spectroscopy of the BBO crystal surface. The spectrometer data are atomic peaks (measured through the energies of the innermost electrons excited by the X-rays). There is no information about molecular structure.

We examined damaged and new crystal surfaces, as well as a mirror from the doubling cavity. Two contaminants were found on the damaged crystal surface: fluorine and chlorine. Fluorine was also seen on the doubling cavity mirror. A contaminant common to all the surfaces we studied is carbon, which contaminates everything [99].

A.5 Finding the Contamination Source

We examined our gas handling system and gas supply for fluorine and chlorine. The fluorine was not hard to trace: not only did our gas handling system contain teflon tubing and teflon tape, but the crystal itself was held in its holder with teflon spacers.

Chlorine is present in many plastic compounds commonly used in "clean" gas systems (PVC, Tygon, Nalgene tubing). To complicate matters, the chemical formula of many commonly used tubing systems are proprietary, and our requests for information were denied by the manufacturing companies. We got around some of these problems by doing surface spectroscopy of the plastic tubing itself.

Kjeld Eikema told us that his group used teflon tubing for their BBO gas handling [26], which seemed to be the likely source of the fluorine contamination of our crystal surface, but they did not have surface damage problems.

We substituted metal and glass for plastic components where possible. Since the gas cylinders are located on the lab floor, and the crystal is on a floating optical table, flexible plastic tubing is necessary to keep the optics table vibrationally isolated from the rest of the room. We substituted all tygon and telflon plastic tubing for silicone tubing from Nalgene. Silicone tubes are made the same elemental components as glass (silicon and oxygen) and are remarkably free of contaminants.

We also investigated the BOC gas cylinder cleaning and filling process in detail. Although it seemed very unlikely that any fluorine or chlorine contamination could happen through this channel, we started using high purity gases.

None of this helped. BBO crystals in our system were still getting damaged in the same way. In fact, the inability to use teflon tape to seal the gas system joints (for instance the important gas cylinder-to-regulator joint) caused the gas cylinders to empty faster, and did little to protect the crystal from outside damage.

By correlating the damage with the presence of chlorine (but not fluorine), using further surface spectroscopy, we concluded that the real culprit of the damage was in fact chlorine alone. We were able to use teflon tape and tubing again. We determined that the chlorine could not be coming from the clean gas delivery system, but must be coming from the lab air.

A.6 Building Air Flow and Lab Overpressure

We concluded that the chlorine contaminating our crystal came from the janitorial staff's floor cleaning of the hallway outside the lab every few nights. The building had recently undergone air flow renovations, and since we had blocked off air flow to the optics lab for fear of dust in the new system, the optics lab was at *underpressure* and sucked in air from the hallway through the cracks around the door.

We also found that other groups using BBO crystals heat the crystal mount, in an effort to prevent water from being absorbed in the crystal [26]. We decided the same rationale might apply to chlorine contamination, and Kendra Vant designed a new crystal mount with a small programmable heater Hytek chip [73] on it.

After unblocking the lab air flow, resuming lab air overpressure compared to the hallway, and heating the crystal, the problem of crystal contamination was solved and has not been seen again in our lab.

A.7 Damage Mechanism: Fluorine vs. Chlorine

An interesting question is why chlorine causes permanent crystal surface damage and fluorine does not, since they are chemically similar (both halogens).

One consideration is the chemical source of the chlorine and fluorine. The data from the X-ray photospectrometer does not indicate the molecular structure, only the relative atomic concentration. However, we know that the fluorine in our lab comes from teflon tape and teflon tubing. Teflon contains fluorine and carbon (as determined by X-ray surface photospectroscopy). Fluorine in this form is quite inert. The chlorine contamination comes from bleach, which is very reactive.

This helps explain why the presence of fluorine does not permanently damage our crystals, whereas chlorine does [3].

A.8 Crystal Surface Repair Techniques

Once a crystal surface is damaged or contaminated, we usually have to send it back to the manufacturer for repolishing. However, there is another cheaper and faster method with the potential for achieving similar results. In discussions with the technical support staff of Cleveland Crystals [14], we learned that they clean their crystals in an a Oxygen Plasma Asher at 10-15 mTorr for 4 minutes before doing coatings.

After using the Oxygen Plasma Asher of the Ashoori group for 4 minutes at 10-15 mTorr, we found that the contamination had decreased by a factor of 3/4.

It should be noted that our BBO crystal is uncoated. Since it is Brewster cut, there is no need for an anti-reflective coating. Moreover, according to Kjeld Eikema [26], any BBO crystal used with light at higher frequency than 300 nm should not be coated, since oxygen bubbles form under the coating. Also, no coated crystal should be put in a plasma asher, for obvious reasons ...

Thanks to Sam Arey for helpful discussions of the chemistry of the contamination and color center formation processes.

Appendix B

Superfluid Helium Jacket Fill Line Design

B.1 Filling and Emptying the Jacket

The superfluid helium jacket that surrounds the cell, providing thermal conductivity from top to bottom, is described in Section 2.3. Filling and emptying the jacket are very time consuming procedures (taking a day each).

Emptying the jacket is also quite risky. It involves heating the cell top to cause the helium vapor pressure to push the helium out the jacket fill line. The jacket fill line is a capillary to avoid a large heat load on the dilution refrigerator. The emptying process goes faster if the helium is liquid in the line, but pushed upwards by gas pressure from the jacket. However, if the pressure in the jacket is too large, it can cause the cell to crack or leak. To avoid this, a jacket fill line relief valve is installed just above the cell.

The jacket fill line relief valve consists of a bellows segment caped by a piece of brass shim, connected by solder. When the bellows expands too far, the shim first makes an electrical connection with a blunt piece of metal connected to a resistor. When a resistance can be read on this connection, the cell top heater is (manually) turned off and the pressure goes down. If the bellows expand further, the shim cap is punctured by a needle and the pressure in the jacket can expand into the IVC. Of course, a repair of the jacket fill line relief valve requires a full warm up and opening the IVC, with the risks of new damage and leaks that these entail, but at least the cell is protected.

The timescale of the filling of the jacket is set by the time it takes the cryostat to liquefy and cool a large amount of helium gas at room temperature. However, the timescale of emptying the jacket is set by the geometry of the fill line. The jacket fill line was initially 3 meters of .3 mm ID capillary line, from the 1 K pot to the jacket itself, thermally anchored at the still, baseplate, and mixing chamber. After a particularly disastrous warm-up due to a jacket relief puncture (see Appendix D below), we decided to change the fill line to be more efficient.

B.2 Contributions to the Heat Load on the Mixing Chamber

We can measure a significant change (20-30 mK) in the temperature of the mixing chamber before and after the jacket is filled. We tried to estimate the different contributions to the heat load on the mixing chamber.

B.2.1 Liquid-helium filled jacket line (no flow)

The fill line itself is made of low thermal conductivity stainless steel. However, when it is filled with liquid helium, the thermal conductivity becomes considerable.

The effective thermal conductivity of a column of helium below 0.4 K is approximated on page 25 of Pobell [85]

$$\kappa \approx 20dT^3 \mathrm{W/cm} \cdot \mathrm{K} \tag{B.1}$$

where d is the column diameter in cm. The heat load is correspondingly

$$\dot{Q} = \frac{A}{l} \int_{T_1}^{T_2} \kappa \mathrm{d}T \approx \frac{4d^3}{l}(T_2^4 - T_1^4) \tag{B.2}$$

where A is the area of the column, l is the length, and T_1 and T_2 are the temperatures on either end. When the dilution refrigerator is running, we expect the mixing chamber temperature to be $T_{\mathrm{MC}} \simeq 50$ mK, the baseplate temperature $T_{\mathrm{BP}} \simeq 250$ mK, the still temperature $T_{\mathrm{S}} \simeq 700 - 800$ mK, and of course the 1K pot temperature $T_{1\mathrm{K}} = 1.7$ K.

If we assume 30 cm length steps between each stage, with 0.017" = 0.43 mm ID capillary lines, the heat load to the mixing chamber from the baseplate is 0.04 μW, the heat load from the still to the baseplate is 3 W and the heat load from the 1K pot to the still is 83 mW. These are all acceptable numbers.

B.2.2 Blackbody heating from 4K IVC tailpiece

Unlike the rest of the IVC apparatus below the 1K pot, the cell does not have a radiation baffle between it and the outer surface of the IVC tailpiece. The IVC tailpiece is at 4K (see cell diagram Figure 2-1) and thus heats the cell through blackbody heating. Any heating to the cell will be transmitted to the mixing chamber since the two are thermally connected through the discharge, which anchored on the mixing chamber.

This heat load to the cell is

$$\dot{Q} = \sigma((4K)^4 - T_{cell}^4)A_{\mathrm{cell}} \approx 1.3\mu\mathrm{W}, \tag{B.3}$$

if $T_{cell} = T_{MC} = 50$ mK.

This heat load is only apparent when the jacket is filled, because when the jacket is empty the cell is effectively thermally disconnected from the mixing chamber. This is the largest heat load to the cell/mixing chamber in these calculations.

B.2.3 Thermal contact from kevlar threads to tailpiece

The cell is centered in the IVC by 3 kevlar threads connected to the 4K tailpiece. We don't know the thermal conductivity of kevlar, but use that of nylon instead: $\kappa_{\text{nylon}} \simeq 7 \times 10^{-5}$ W·cm^{-1}·K^{-1}.

Assuming the diameter d of the threads is 0.3 mm and their length l is 5 cm, we find a total

$$\dot{Q} = \frac{\pi d^2}{4l}\kappa(4\text{K} - T_{\text{cell}}) \simeq .05\mu\text{W}. \tag{B.4}$$

B.3 Superfluid Flow Heating

Superfluid helium flows from cold to warmer spots. We estimate the heat flow from a film of superfluid helium coating the inside of the jacket fill line, flowing to a warm spot, evaporating and recondensing in the line. We use a 30 nm thick film (page 26 of Pobell [85]) and a film flow velocity of 30 cm·sec^{-1} (page 28 of Pobell [85]). Then

$$\dot{Q} = \pi d\, f_{\text{fudge}} 30\text{nm}\, 30\,\text{cm} \cdot \text{sec}^{-1}\, Q_L \tag{B.5}$$

where $d = 0.4$ mm is the inner diameter of the fill line, f_{fudge} is fudge factor taking into account the roughness seen by the superfluid film (taken to be 5), and $Q_L = 2.56$ Joule·cm^{-3} is the latent heat of vaporization of ^{4}He. In this case, the estimate for the heat load from the 1K pot to the still is .1 mW.

Another way of looking at the superfluid flow is to assume the entire capillary is filled with helium. Then

$$\dot{Q} = \frac{\pi d^2}{4}\, 30\text{cm} \cdot \text{sec}^{-1}\, Q_L \simeq 0.1\text{W}. \tag{B.6}$$

This value for the heat load seems too large.

Whatever the case may be, the superfluid flow/evaporation/recondensation is most likely to happen between the still and the 1K pot, not at the mixing chamber. To minimize the heat flow due to this, we introduce a 35 cm section of 0.3 mm ID capillary between the 1K pot and the 30 cm 0.4 mm ID line going to the still.

B.4 Current Fill Line Design Summary

The current fill line is constituted of 3 30 cm long 0.4 mm ID capillary segments, between the mixing chamber, baseplate, and still. The line leaving from the still connects to a 35 cm long segment of 0.3 mm ID capillary line to the 1K pot.

Using this new line, we can empty the jacket in close to three hours, an improvement of more than a factor of 2 on the old fill line design. No extra heating of the cell or mixing chamber has been observed compared to the old design, which is consistent with our calculation showing that the main heat load on the mixing chamber comes the 4K black body radiation on the cell when the jacket is filled, not the jacket line itself.

Appendix C

Magnet Power Supply Control

C.1 Original Design, Floating Voltage Requirement

Most continuous current supplies were originally designed to be remotely operated through a variable resistance (trimpot) connected to external terminals on the supply [67]. Since effectively a varying voltage was measured across the resistance, this design was adapted to incorporate remote control by varying a voltage across two power supply terminals.

A variable voltage is obviously more convenient than a varying resistor for uses with modern computer control through analog outputs. However, it is not advisable to use an analog output directly from a computer DAC or a normal grounded voltage supply. The current supply expects a *floating* control voltage. If a grounded voltage is supplied, the current supply output will also be connected to ground, with sometimes surprising resulting behavior (especially if several supplies are connected through magnets, as in our system). Responses such as no current output, oscillations and spiking have been observed.

C.2 Control Voltage Circuit Design

To avoid this problem, we have designed a power supply control circuit that takes a grounded voltage, divides it into the 0-1V range, floats it through the voltage difference amplifier INA 117, amplifies it by a variable gain and offsets it by a variable voltage. The circuit diagram is shown in Fig. C-1.

The circuit shown in Fig. C-2 has a feedback stage, so that the current can be monitored across a shunt and corrected if necessary. In this case the negative pin of the monitored current is grounded, if not, modificaitions should be made. The diode clamp in the last stage prevents the output voltage from being negative, and is necessary in some cases where the supply responds to an initial small negative voltage with a time lag in turn on, resulting in overshooting. A negative voltage is not a normal output of the circuit, but could be induced by the current of another power supply across the same coil. The output from this supply must be floated through a circuit similar to the one shown in Fig. C-1.

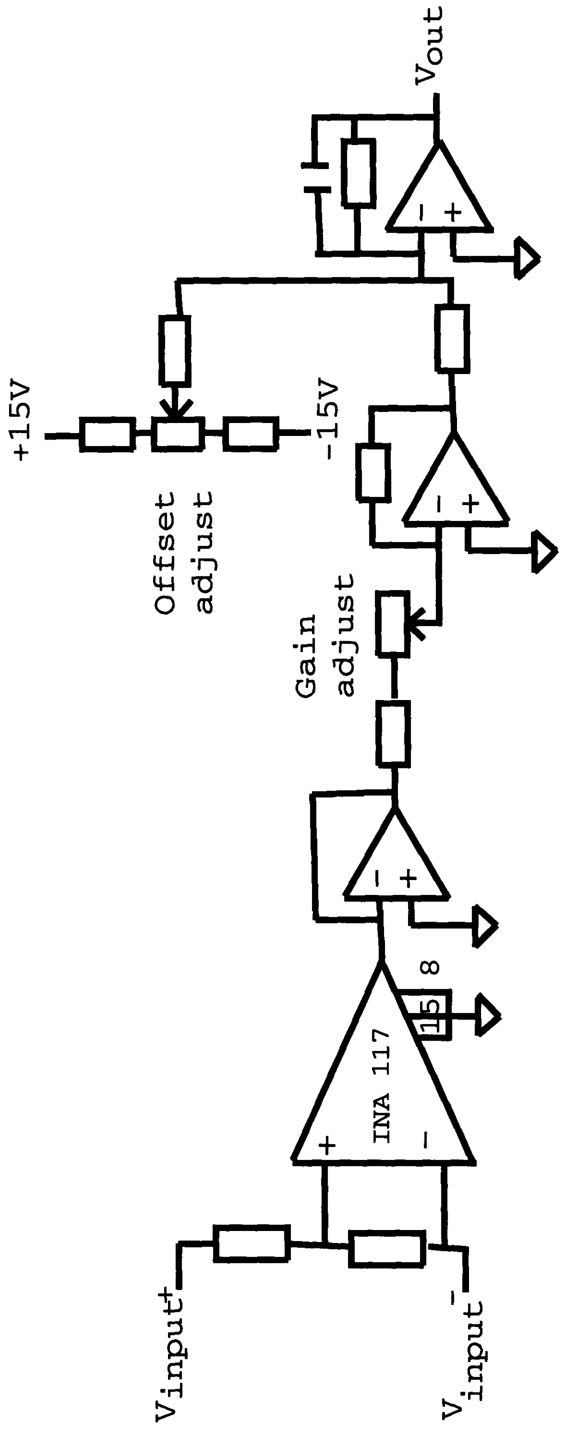

Figure C-1: Floating voltage circuit for current supply control.

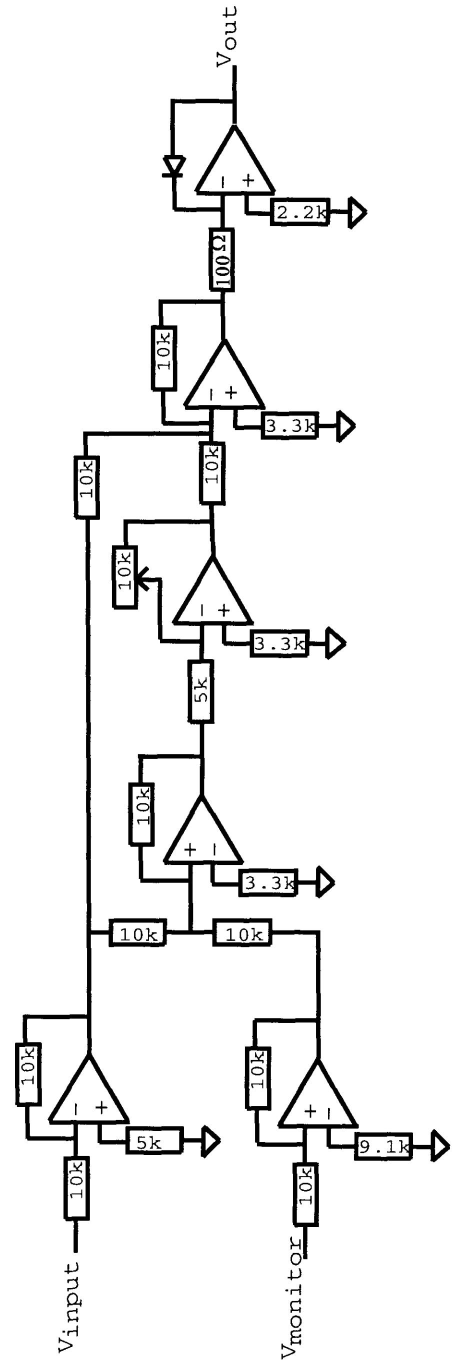

Figure C-2: Feedback circuit for current supply control.

The feedback portion was used in the high magnetic field 2S hyperfine splitting experiment, chapter 3. The power supplies needed to be steadily ramped up in seconds, and stay at constant current values during the spectroscopy (several minutes). However, most large current supplies, although they eventually stay at constant current values, have a slow exponential drift after ramp-up. In particular, the Hewlett Packard 6012A 60 A current supply for the bias magnet drifted by as much as 1% in the first minute after ramp-up. This corresponded to a 8 G drift during spectroscopy, an unacceptably large number. By measuring the current across a high current precision resistor, and using the control circuit feedback loop, the bias supply stayed steady to a part in 10^4 per minute, a tremendous improvement.

Care must be taken in setting the values for the feedback gain and timescale. Magnets usually have inductances, and it is quite easy to amplify oscillations of the circuit.

Appendix D

Repairing Leaking Dilution Fridge Heat Exchangers

D.1 What Are Dilution Fridge Heat Exchangers?

The heat exchangers of the Oxford ^{3}He-^{4}He dilution refrigerator [83] are located between the still and the mixing chamber. The purpose and design of heat exchangers is described in detail by Pobell [85] in section 7.3.3. Heat exchangers cool the ^{3}He liquid incoming to the mixing chamber, by using thermal contact with outgoing ^{3}He in dilute solution.

The Oxford dilution refrigerator's heat exchangers are similar to the Frossati design in figure 7.14 of Pobell. They are made of 3 sheets of 70-30 Cu-Ni soldered together, forming two distinct volumes, packed with silver sinter.

D.2 Discovery of a 4K Fridge to IVC Leak

During a cooldown in spring 2003, we found a dilution refrigerator leak into the IVC. The leak was detected first as a warming of the dilution refrigerator system. While at liquid helium temperatures, we probed the IVC gas accumulation, after first filling the bath space, then the 1 K pot, then the fridge. The IVC background was higher after the mixture was condensed in the fridge.

The leak had not been visible during the cooldown, and may have opened up going to 4 K. At room temperature, the leak was apparent as a ^{4}He leak while leak checking the IVC, as a slow small rise on the leak detector on the order of 1 minute. with 10 mbar pressure at the still. The leak was closer to the still than the condenser (faster rise time).

D.3 Locating a Leak on the Cryostat

To localize the leak, the cryostat itself must be leak checked. This is done using hydrogen gas, as the helium background in the cryostat is so high. The leak check procedure was very lengthy, since it took 30 seconds for the leak detector level to rise slightly, and then 30 seconds to drift back down. We bagged off different portions of the fridge to blow hydrogen gas on them.

When the leak was found to be on the heat exchangers, we faced the challenge of locating it more precisely. To do so, we bagged off each heat exchanger stage, and located the stage of the leak. Then we made a plastic nozzle for the hydrogen gas delivery that would fit on the edge of the heat exchanger (without damaging it further), and found the exact location of the leak. To help with this lengthy and frustrating process, we used little strips of paper tape to mark the edges. The leak was finally pinpointed within a centimeter of the north-east inner edge of the 5th heat exchanger down from the top.

We used a fan to disperse the hydrogen gas while leak checking. During this leak check process, we used 1 hydrogen gas cylinder every 2-3 days.

D.4 Possible Leak Repair Mishaps

Repairing the leak is done by locally heating the heat exchanger seal edge, applying flux using an acid brush (available at the Central Machine Shop), reflowing the original solder, and adding some solder on the outside. The flux used was Super Flux 22, soft solder liquid flux, from "the Superior Flux & Mfg. Co." CAS 7646-85-7, which contains zinc chloride. The solder used was solid core, most likely 60-40 (shiny).

In repairing the leak, it is crucial to try to avoid creating more damage. Since the original vacuum seal is made using solder, and since Cu-Ni conducts heat very well, it is possible to open more leaks along the same edge when heating the heat exchanger. Even worse, it is possible to cause the solder along the entire edge seal to flow, in which case the heat exchanger would open up completely.

To avoid this contingency, we machined two aluminum clamps. These were designed to fit between the heat exchanger stages, and clamp down only on the edges of the heat exchanger on either side of the leak. Not only do the clamps mechanically prevent the heat exchanger from opening up, they also act as heat sinks. It is also possible to use wet paper towels as effective heat sinks.

It is also crucial to use a powerful but temperature regulated soldering iron heater. We used a Weller EC 1002 temperature controlled heater. This is to maintain a heat sufficient to cause solder to flow locally, but to prevent overheating that could flow solder throughout the heat exchanger. It also allows us to see when we have good thermal contact (the temperature drops).

Another risk is of fixing the external leak, but opening an internal leak from the incoming ^{3}He channel to the outgoing ^{3}He channel. There is little one can do avoid this, but one should at least be aware it can happen, and look for it in subsequent leak checks (for instance as a change in timescale of gas going from still side to condenser side or vice-versa). The only way of fixing an internal leak from the outside is to keep trying to reflow the internal solder.

A third risk is involved when using flux on Cu-Ni. All flux should be carefully removed (and adjacent heat exchanger stages shielded during soldering, and thoroughly cleaned afterwards). Even a small flux residue or splatter can eventually eat through the thin Cu-Ni, and cause more leaks in the future. For this reason it is also important to heat the piece long enough not only for the solder to flow, but also for any flux mixed in with the solder to burn away.

The interior of the heat exchanger is filled with silver sinter. It is important to use as little solder as possible, otherwise solder could get sucked inside the heat exchanger and plug up the spaces between the sinter, constricting the flow. It is also important not to use too much heat because the silver sinter could melt.

D.5 Solder Tip Designing and Testing

Difficulty of access of the interior heat exchanger edges is a problem at every stage of the leak testing and repair. Most commercially available soldering iron tips are both too short and too thick to access the inner edge of a heat exchanger. It is thus necessary to make one's own. We used a rod of oxygen-free copper, and machined a long thin solder iron tip on the lathe. Machining copper is very difficult, and a thin long rod requires a lot of patience on the lathe.

Once the tip was made, we bent it to the appropriate shape *before* fitting on the solder iron heater. This was a mistake, since it is not possible to fit the iron holder fitting over a bent tip. However we were able to tighten the tip to the heater using a system of wire and screws.

We asked a metal supply company found through Thomas Register for a sample of the thinnest Cu-Ni sheet they carried. We rigged a test jig with the approximate geometry of the heat exchanger, using two pieces of the Cu-Ni sheet as the heat exchanger to repair. The MIT Central Machine Shop machined a hole in the center of the two Cu-Ni sheets, and made the edges thinner to approximate the actual heat exchanger edge.

Testing was done for geometry of the soldering iron, ways to maintain good thermal contact, applying the flux and solder, and the time and temperature setting required to heat the Cu-Ni. As a result of the testing, we knew the appropriate temperature setting for the soldering iron power supply and the timescale of the piece heating and repair. We also cut a small wedge in the soldering iron where it would be held against the edge of the heat exchanger, to make the thermal contact better and more steady.

We brushed the flux on the heat exchanger edge. Then we put solder on the iron tip, applied the iron to the heat exchanger, slid it around the edge close to the leak when things were warm, and the repair was done.

The elaborate preparation and testing was successful. The leak was repaired on the first attempt and the cryostat has worked without major problems since.

Bibliography

[1] J.M. Anthony and K.J. Sebastian. Relativistic corrections to the zeeman effect in hydrogenlike atoms and positronium. *Phys. Rev. A*, 49:192, 1994.

[2] T. Arai, M. Yamane, A. Fukuda, and T. Mizusaki. The second order recombination and spin-exchange relaxation of atomic deuterium at low temperatures in a low magnetic field. *Journal of Low Temperature Physics*, 112(5-6):373–398, 1998.

[3] Samuel Arey. Personal communication. Department of Civil and Environmental Engineering Massachusetts Institute of Technology.

[4] J. Bardeen, L.N. Cooper, and J.R. Schrieffer. Theory of superconductivity. *Phys. Rev.*, 1957.

[5] D. A. Bell, H. F. Hess, G. P. Kochanski, S. Buchman, L. Pollack, Y. M. Xiao, D. Kleppner, and T. J. Greytak. Relaxation and recombination in spin-polarized atomic hydrogen. *Phys. Rev. B*, 34(11):7670, December 1986.

[6] H.A. Bethe and E.E. Salpeter. *Quantum Mechanics of one- and two- electron atoms.* Springer Verlag, 1957.

[7] F. Biraben, M. Bassini, and B. Cagnac. Line-shapes in doppler-free two-photon spectroscopy. the effect of finite transit time. *J. Phys. (Paris)*, 40:445, 1979.

[8] G. Breit and I. Rabi. Measurement of nuclear spin. *Phys. Rev.*, 38:2082, 1931.

[9] C. L. Cesar. *Two-Photon Spectroscopy of Trapped Atomic Hydrogen.* PhD thesis, Massachusetts Institute of Technology, 1995.

[10] C.L. Cesar and D. Kleppner. Two-photon doppler-free spectroscopy of trapped atoms. *Phys. Rev. A*, 59:4564, 1999.

[11] Claudio L. Cesar, Dale G. Fried, Thomas C. Killian, Adam D. Polcyn, Jon C. Sandberg, Ite A. Yu, Thomas J. Greytak, Daniel Kleppner, and John M. Doyle. Two-photon spectroscopy of trapped atomic hydrogen. *Phys. Rev. Lett.*, 77(2):255, July 1996.

[12] R.W. Cline, David A. Smith, T.J. Greytak, and D. Kleppner. Magnetic confinement of spin-polarized atomic hydrogen. *Phys. Rev. Lett.*, 45:2117, 1980.

[13] E.R. Cohen and B.N. Taylor. The 1986 adjustment of the fundamental physical constants. *Rev. Mod. Phys.*, 59:1121, 1987.

[14] Cleveland Crystals. www.clevelandcrystals.com. (216)486-6100.

[15] B. de Beauvoir, C. Schwob, O. Acef, L. Jozefowski, L. Hilico, F. Nez, L. Julien, A. Clairon, and F. Biraben. Metrology of the hydrogen and deuterium atoms: Determination of the rydberg constant and lamb shifts. *Eur. Phys. Jour. D*, 12:61, 2000.

[16] R. deCarvalho, J.M. Doyle, B. Friedrich, T. Guillet, J. Kim, D. Patterson, and J.D. Weinstein. Buffer-gas loaded magnetic traps for atoms and molecules: a primer. *European Physical Journal D*, 7:289, 1999.

[17] Robert deCarvalho. *Inelastic Scattering of Magnetically Trapped Atomic Chromium.* PhD thesis, Harvard University, 2003.

[18] B. DeMarco and D. S. Jin. Onset of Fermi degeneracy in a trapped atomic gas. *Science*, 285(5434):1703, September 1999.

[19] J.M. Doyle, B. Friedrich, Jinha Kim, and David Patterson. Buffer-gas loading of atoms and molecules into a magnetic trap. *Phys. Rev. A*, 52:R2515, 1995.

[20] J.M. Doyle, J.C. Sandberg, I.A. Yu, C.L. Cesar, D. Kleppner, and T.J. Greytak. Hydrogen in the submillikelvin regime: Sticking probability on superfluid ^{4}he. *Phys. Rev. Lett*, 67:603, 1991.

[21] John Doyle. Personal communication. Physics Department, Harvard University.

[22] John M. Doyle. *Energy Distribution Measurements of Magnetically Trapped Spin Polarized Atomic Hydrogen: Evaporative Cooling and Surface Sticking.* PhD thesis, Massachusetts Institute of Technology, 1991.

[23] John M. Doyle, Jon C. Sandberg, Ite A. Yu, Claudio L. Cesar, Daniel Kleppner, and Thomas J. Greytak. Hydrogen in the submillikelvin regime: Sticking probability on superfluid ^{4}He. *Phys. Rev. Lett.*, 67(5):603, July 1991.

[24] R.W.P. Drever, J.L. Hall, F.V. Kowalski, J. Hough, G.M. Ford, A.J. Munley, and H. Ward. Laser phase and frequency stabilization using an optical resonator. *Applied Physics B*, page 31, 1983.

[25] M.I. Eides, H. Grotch, and V.A. Shelyuto. Theory of light hydrogenlike atoms. *Physics Reports*, 342:63–261, 2001.

[26] Kjeld Eikema. Personal communication. Vrige University Physics Department Laser Center in the Netherlands.

[27] Electronic Navigation Industries, Inc. *Instruction Manual Model 550L Broadband Power Amplifier.*

[28] Emerson & Cuming Speciality Polymers, a division of National Starch and Chemical Company. *Stycast 1266 A/B two component, low viscosity, epoxy encapsulant*, 1998.

[29] L. Essen, R.W. Donaldson, M.J. Bangham, and E.G. Hope. Frequency of the hydrogen maser. *Nature*, 229:110, 1971.

[30] Dale G. Fried. *Bose-Einstein Condensation of Atomic Hydrogen*. PhD thesis, Massachusetts Institute of Technology, 1999.

[31] Dale G. Fried, Thomas C. Killian, Lorenz Willmann, David Landhuis, Stephen C. Moss, Daniel Kleppner, and Thomas J. Greytak. Bose-Einstein condensation of atomic hydrogen. *Phys. Rev. Lett.*, 81(18):3811, November 1998.

[32] J.D. Gillaspy and C.J. Sansonetti. Absolute wavelength determinations in molecular tellurium: new reference lines for precision laser spectroscopy. *J. Opt. Soc. Am. B*, 8:2414, 1991.

[33] S. R. Granade, M. E. Gehm, K. M. O'Hara, and J. E. Thomas. All-optical production of a degenerate Fermi gas. *Phys. Rev. Lett.*, 88(12):120405, March 2002.

[34] T. Greytak. Personal communication. Department of Physics Massachusetts Institute of Technology.

[35] H. Grotch and R.A. Hegstrom. Hydrogenic atoms in a magnetic field. *Phys. Rev. A*, 4:59, 1971.

[36] H. Grotch and R. Kashuba. Magnetic interactions of one-electron atoms and positronium. *Phys. Rev. A*, 7:78, 1973.

[37] Z. Hadzibabic, C. A. Stan, K. Dieckmann, S. Gupta, M. W. Zwierlein, A. Görlitz, and W. Ketterle. Two-species mixture of quantum degenerate Bose and Fermi gases. *Phys. Rev. Lett.*, 88(16):160401, April 2002.

[38] G. Hagel, C. Schwob, L. Jozefowski, B de Beauvoir, L. Hilico, F. Nez, L. Julien, F. Biraben, O. Acef, and A. Clairon. Metrology of hydrogen atom: Determination of the rydberg constant and lamb shifts. *Laser Physics*, 11:1076, 2001.

[39] J.G.E. Harris, R.A. Michniak, S.V. Nguyen, W. Ketterle, and J.M Doyle. Buffer gas cooling and trapping of atoms with small magnetic moments. *cond-mat/0311349*, 2003.

[40] M. E. Hayden and W. N. Hardy. Atomic hydrogen-deuterium mixtures at 1k: recombination rates, spin-exchange cross sections, and solvation energies. *J. Low Temp. Phys.*, 99:787, 1995.

[41] M. E. Hayden, M. W. Reynolds, and W. N. Hardy. Atomic hydrogen and deuterium mixtures at 1k. *Physica B*, 169:541–542, 1991.

[42] J.W. Heberle, H.A. Reich, and P. Kusch. Hyperfine structure of the metastable hydrogen atom. *Phys. Rev.*, 101:612, 1956.

[43] Harald F. Hess. Evaporative cooling of magnetically trapped and compressed spin-polarized hydrogen. *Phys. Rev. B*, 34(5):3476, September 1986.

[44] Hewlett Packard. *Regulated DC Power Supply Models 6259B, 6260B, 6261B, 6268B, 6269B Operating and Service Manual*, 1976.

[45] Hewlett Packard. *6012A Autoranging DC Power Supply Operating and Service Manual*, 1980.

[46] Hewlett Packard. *8662A Synthesized Signal Generator 10 kHZ-1280MHz Operating and Service Manual*, 1982.

[47] M. Houbiers, R. Ferwerda, H. T. C. Stoof, W. I. McAlexander, C. A. Sackett, and R. G. Hulet. Superfluid state of atomic ^{6}Li in a magnetic trap. *Phys. Rev. A*, 56(6):4864, December 1997.

[48] A. Huber, Th. Udem, B. Gross, J. Reichert, M. Kourogi, K. Pachucki, M. Weitz, and T.W. Hänsch. Hydrogen-deuterium $1s - 2s$ isotope shift and the structure of the deuteron. *Phys. Rev. Lett.*, 80:468, 1998.

[49] Ulrich Jonas. Introduction to surface chemistry. Online lecture notes: http://www.mpip-mainz.mpg.de/ jonas/.

[50] S.G. Karshenboim. The g factor of the proton. *Phys. Lett. B*, 566:27, 2003.

[51] S.G. Karshenboim and V.G. Ivanov. Hyperfine structure in hydrogen and helium ion. *Phys. Lett. B*, 524:259, 2002.

[52] S.G. Karshenboim and V.G. Ivanov. Hyperfine structure of the ground and first excited states in light hydrogen-like atoms and high-precision tests of qed. *Eur. Phys. Jour. D*, 19:13, 2002.

[53] Wolfgang Ketterle and N. J. van Druten. Evaporative cooling of trapped atoms. *Adv. At. Mol. Opt. Phys.*, 37(0):181, 1996.

[54] T. Killian. *1S-2S Spectroscopy of Trapped Hydrogen: the Cold Collision Shift and Studies of BEC.* PhD thesis, Massachusetts Institute of Technology, 1999.

[55] T.C. Killian, D.G. Fried, L. Willmann, D. Landhuis, S.C. Moss, T.J Greytak, and D. Kleppner. Cold collision frequency shift of the $1s - 2s$ transition in hydrogen. *Phys. Rev. Lett*, 81:3807, 1998.

[56] Toichiro Kinoshita. Present status of $g - 2$ of electron and muon. In S.G. Karshenboim, editor, *The Hydrogen Atom, Precision Physics of Simple Atomic Systems*, page 157. Springer-Verlag, 2001.

[57] Charles Kittel and Herbert Kroemer. *Thermal Physics (second edition)*. Freeman, 1980.

[58] Gregory Kochanski. *Magnetic Trapping and Cooling of Atomic Hydrogen*. PhD thesis, Massachusetts Institute of Technology, 1982.

[59] J. M. V. A. Koelman, H. T. C. Stoof, B. J. Verhaar, and J. T. M. Walraven. Spin-polarized deuterium in magnetic traps. *Phys. Rev. Lett.*, 59:676, 1987.

[60] J. M. V. A. Koelman, H. T. C. Stoof, B. J. Verhaar, and J. T. M. Walraven. Lifetime of magnetically trapped ultracold atomic deuterium gas. *Phys. Rev. B*, 38:9319, 1988.

[61] Vianney Koelman. *New directions in the theory of spin-polarized atomic hydrogen and deuterium*. PhD thesis, Technische Universiteit Eindhoven, 1988.

[62] N. Kolachevsky, M. Fischer, S.G. Karshenboim, and T.W. Hänsch. High-precision optical measurement of the 2s hyperfine interval in atomic hydrogen. *Phys. Rev. Lett.*, 92:033003, 2004.

[63] L.D. Landau. *Phys. Z. Sowjetunion*, 1932.

[64] D. Landhuis, L. Matos, S.C. Moss, J.K. Steinberger, K. Vant, L. Willmann T.J. Greytak, and D. Kleppner. Inelastic collision rates of trapped metastable hydrogen. *Phys. Rev. A*, 67:022718, 2003.

[65] David Paul Landhuis. *Studies with Ultracold Metastable Hydrogen*. PhD thesis, Harvard University, 2002.

[66] O. J. Luiten, M. W. Reynolds, and J. T. M. Walraven. Kinetic theory of the evaporative cooling of a trapped gas. *Phys. Rev. A*, 53(1):381, January 1996.

[67] Jim MacArthur. Personal communication. Physics Department Electronics Shop, Harvard University.

[68] J. M. Marin, J. Boronat, and J. Casulleras. Atomic and molecular hydrogen impurities in liquid he-4. *Jounal of Low Temperature Physics*, 110(1/2):205–211, 1998.

[69] Naoto Masuhara, John M. Doyle, Jon C. Sandberg, Daniel Kleppner, Thomas J. Greytak, Harald Hess, and Gregory P. Kochanski. Evaporative cooling of spin-polarized atomic hydrogen. *Phys. Rev. Lett.*, 61(8):935, August 1988.

[70] R. Mayer and G. Seidel. Electron spin resonance of atomic hydrogen and deuterium at low temperatures. *Phys. Rev. B*, page 4199, 1985.

[71] David McIntyre. *High Resolution Laser Spectroscopy of Tellurium and Hydrogen: A Measurement of the Rydberg Constant.* PhD thesis, Stanford University, 1987.

[72] H.J. Metcalf and P. van der Straten. *Laser Trapping and Cooling.* Springer, 1999.

[73] Hytek Microsystems. www.hytek.com.

[74] S. Millman, I.I. Rabi, and J.R. Zacharias. On the nuclear moments of indium. *Phys. Rev.*, 53:384, 1938.

[75] P.J. Mohr and B.N. Taylor. Codata recommended vales of the fundamental physical constants: 1998. *Phys. Rev.*, 72(2):351, 2000.

[76] P.J. Mohr and B.N. Taylor. The 2002 recommended values of the fundamental physical constants, web version 4.0. *http://physics.nist.gov/constants/*, 2002.

[77] M. Morrow, R. Jochemsen, A. J. Berlinsky, and W. N. Hardy. Zero-field hyperfine resonance of atomic hydrogen for $0.18 \leq \mathrm{t} \leq 1$ k: The binding energy of h on liquid ^{4}he. *Phys. Rev. Lett.*, 46:195, 1981. Erratum Phys. Rev. Lett. 47 p. 455.

[78] A. P. Mosk, M. W. Reynolds, and T. W. Hijmans. Atomic deuterium adsorbed on the surface of liquid helium. *Phys. Rev. A*, 64:022901–1, 2001.

[79] Stephen C. Moss. *Formation of a Bose-Einstein Condensate in Atomic Hydrogen.* PhD thesis, Massachusetts Institute of Technology, 2002.

[80] M. Niering, R. Holzwarth, J. Reichert, P. Pokasov, T. Udem, M. Weitz, T.W. Hänsch, P. Lemonde, G. Santarelli, M. Abgrall, P. Laurent, C.Salomon, and A. Clairon. Measurement of the hydrogen $1s-2s$ transition frequency by phase coherent comparison with a microwave cesium fountain clock. *Phys. Rev. Lett.*, 84:5496, 2000.

[81] D.N. Nikogosyan. Beta barium borate (bbo). *Applied Physics A*, page 359, 1991.

[82] R. Onofrio and C. Presilla. Ultracold atomic fermi-bose mixtures in bichromatic optical dipole traps: a novel route to study fermion superfluidity. *Journal of Statistical Physics*, 115:57, 2004. cond-mat/0403612.

[83] Oxford Instruments Limited. *Model 2000 Dilution Refrigerator System Instruction Manual.* Project number 26418.

[84] R. K. Pathria. *Statistical Mechanics.* Butterworth Heinemann, 1972.

[85] Frank Pobell. *Matter and Methods at Low Temperatures Second Edition.* Springer, 1996.

[86] David E. Pritchard. Cooling neutral atoms in a magnetic trap for precision spectroscopy. *Phys. Rev. Lett.*, 51(15):1336, October 1983.

[87] D.E. Pritchard, K. Helmerson, and A.G. Martin. In S. Haroche, J.C. Gay, and G. Grynberg, editors, *Atomic Physics*, volume 11, page 179. World Scientific, Singapore, 1989.

[88] N. Ramsey. Atomic hydrogen hyperfine structure experiments. In T. Kinoshita, editor, *QUANTUM ELECTRODYNAMICS*, page 673. World Scientific, 1993.

[89] M. W. Reynolds, M. E. Hayden, and W. J. Hardy. Resonance recombination of spin-polarized deuterium. In S. Stringari, editor, *Spin Polarized Quantum Systems*, page 236. World Scientific Publishing, 1989.

[90] M. W. Reynolds, M. E. Hayden, and W. N. Hardy. Atomic deuterium at 1k. *Physica B*, 165&166:741–742, 1990.

[91] M. W. Reynolds, M. E. Hayden, and W. N. Hardy. Hyperfine resonance of atomic deuterium at 1k. *J. Low Temp. Phys.*, 84:87, 1991.

[92] G. Roati, F. Riboli, G. Modugno, and M. Inguscio. Fermi-Bose quantum degenerate ^{40}K-^{87} Rb mixture with attractive interaction. *Phys. Rev. Lett.*, 89(15):150403, October 2002.

[93] N.E. Rothery and E.A. Hessels. Measurement of the 2s atomic hydrogen hyperfine interval. *Phys. Rev. A*, 61:044501, 2000.

[94] M. Saarela and E. Krotscheck. Hydrogen isotope and he-3 impurities in liquid he-4. *Journal of Low Temperature Physics*, 90(5/6):415, 1993.

[95] A. I. Safonov, S. A. Vasilyev, A. A. Kharitonov, S. T. Boldarev, I. I. Lukashevich, and S. Jaakkola. Adsorption and two-body recombination of atomic hydrogen on he-3-he-4 mixture films. *Phys. Rev. Lett.*, 86(15):3356–3359, 2001.

[96] J.C. Sandberg. *Research Toward Laser Spectroscopy of Trapped Atomic Hydrogen.* PhD thesis, Massachusetts Institute of Technology, 1993.

[97] F. Schreck, L. Khaykovich, K. L. Corwin, G. Ferrari, T. Bourdel, J. Cubizolles, and C. Salomon. Quasipure Bose-Einstein condensate immersed in a Fermi sea. *Phys. Rev. Lett.*, 87(8):080403, August 2001.

[98] J. Schwinger. Quantum electrodynamics and the magnetic moment of the electron. *Phys. Rev.*, 73:416L, 1948.

[99] Elizabeth Shaw. Personal communication. Center for Material Science and Engineering Massachusetts Institute of Technology.

[100] I. Shinkoda, M. W. Reynolds, R. W. Cline, and W. N. Hardy. Observation of doubly spin-polarized deuterium by electron spin resonance. *Phys. Rev. Lett.*, 57:1243, 1986.

[101] I. F. Silvera and J. T. M. Walraven. Spin-polarized atomic deuterium: stabilization, limitations on density, and adsorption energy on helium. *Phys. Rev. Lett.*, 45:1268, 1980.

[102] Aimee Smith. Personal communication. Department of Material Science and Engineering Massachusetts Institute of Technology.

[103] Inc. Stanford Research Systems. *Model FS700 LORAN-C Frequency Standard*, 1990. Revision 2.0.

[104] H.T.C. Stoof, J.M.V.A. Koelman, and B.J. Verhaar. Spin-exchange and dipole relaxation rates in atomic hydrogen: rigorous and simplified calculations. *Phys. Rev. B*, 38:4688, 1988.

[105] D.R. Tilley and J. Tilley. *Superfluidity and Superconductivity.* Adam Hilger, 1990.

[106] Andrew G. Truscott, Kevin E. Strecker, William I. McAlexander, Guthrie B. Partridge, and Randall G. Hulet. Observation of Fermi pressure in a gas of trapped atoms. *Science*, 291(5513):2570, March 2001.

[107] Th. Udem, A. Huber, B. Gross, J. Reichert, M. Prevedelli, M. Weitz, and T. W. Hänsch. Phase-coherent measurement of the hydrogen 1s-2s transition frequency with an optical frequency interval divider chain. *Phys. Rev. Lett.*, 79:2646, 1997.

[108] K.M. Vant. Upcoming Ph.D. Thesis. Personal communication, 2005.

[109] N.V. Vitanov and K.A. Suominen. Time-dependent control of ultracold atoms in magnetic traps. *Phys. Rev. A*, 56:R4377, 1.

[110] L. Viverit, S. Giorgini, L. P. Pitaevskii, and S. Stringari. Adiabatic compression of a trapped Fermi gas. *Phys. Rev. A*, 63:033603, February 2001.

[111] J.T.M. Walraven, I.F.Silvera, and A.P.M. Matthey. Magnetic equation of state of a gas of spin-polarized atomic hydrogen. *Phys. Rev. Lett*, 45:449, 1980.

[112] S.F. Watanabe and H.G. Robinson. Motional narrowing of zeeman resonance lineshapes i. theoretical development. *J. Phys. B*, 10:931, 1977.

[113] R.C. Weast, editor. *CRC Handbook of Chemistry and Physics.* CRC Press, 1988.

[114] M. Weitz, A. Huber, F. Schmidt-Kaler, D. Leibfried, W. Vassen, C. Zimmermann, K. Pachucki, and T. W. Hänsch. Precision measurement of the 1s ground-state lamb shift in atomic hydrogen and deuterium by frequency comparison. *Phys. Rev. A*, 52:2664, 1995.

[115] L. Willmann and D. Kleppner. Ultracold hydrogen. In S.G. Karshenboim, editor, *The Hydrogen Atom, Precision Physics of Simple Atomic Systems*, page 42. Springer-Verlag, 2001.

[116] W.H. Wing. Gravitational effects in particle traps. *Prog. Quant. Electr.*, 8:181, 1984.

[117] P.F. Winkler, D. Kleppner, T. Myint, and F.G. Walther. Magnetic moment of the proton in bohr magnetons. *Phys. Rev. A*, 5:83, 1972.

[118] I.A. Yu, J.M. Doyle, J.C. Sandberg, C.L. Cesar, D. Kleppner, and T.J. Greytak. Evidence for universal quantum reflection of hydrogen from liquid ^{4}he. *Phys. Rev. Lett.*, 71:1589, 1993.

[119] Ite Albert Yu. *Ultracold Surface Collisions: Sticking Probability of Atomic Hydrogen on Superfluid* ^{4}*He.* PhD thesis, Massachusetts Institute of Technology, 1993.

[120] C. Zener. Non-adiabatic crossing of energy levels. *Proc. R. Soc. London A*, 137:696, 1932.